Advanced Accelerator Interaction Region Optics for LHC Operation and Future Hadron Colliders

Léon van Riesen-Haupt

Keble College

University of Oxford

A thesis submitted for the degree of

Doctor of Philosophy

Hilary 2019

Acknowledgements

First of all I would like to thank my supervisor Andrei Seryi. His insights and ideas have driven the research in this thesis from the very first day. Andrei's encouragement and guidance created an extremely positive working environment resulting in interesting group discussions and giving me motivation and confidence in my work.

I would also like to thank Emmanuel Tsesmelis for taking over as my supervisor when Andrei left, his feedback and support during the final stages of my thesis was critical. Moreover, the first year accelerator courses that he organises provided a strong foundation for the work during my PhD. At this point I would like to acknowledge everyone involved in teaching in these courses, especially Ted Wilson, who showed us how enjoyable accelerator design can be.

I would like to thank all my colleagues in Oxford and the other JAI institutions who helped create a positive and familiar atmosphere within the institute. Special thanks go, of course, to my group members and friends Emila Cruz-Alaniz and José Abelleira who helped me a lot throughout my studies and were great company along the way.

My thanks also go to the colleagues at CERN who have always been welcoming and helpful when I was visiting. I would like to thank Rogelio Tomás who is very approachable and always has great input on my work and ideas with whom I could co-operate. As well as Frank Zimmermann, for his keen interest and support in my work. My gratitude also goes to Daniel Schulte and Antoine Chance as well as Roman Martin and Andy Langner who were a great help on all FCC-hh related topics. Moreover, I want to thank my friends and colleagues Michael Hofer, Jacqueline Keintzel, Matthew Crouch and Demin Zhou — together we created a great HE-LHC team. Finally, I want to thank the entire OMC team for letting me join during various measurement session on the LHC as well as teaching me how to extract the data.

I am eternally grateful for my mother who supported and motivated me in everything I did, my father who was always there and I can count on and my stepfather who has motivated me to follow an analytical path from a young age. Without their love and support I would never be where I am today.

Special thanks go to my partner Muna who supported me and was with me on the PhD journey since the very first day. I want to thank my

brothers Aaron and David, who have been my best friends since I can remember. Of course I have to also acknowledge my baby siblings Anouk and Besarion who have been an inspiration to do well.

I also acknowledge all the friends I have made in Oxford and CERN during my PhD outside of work. I am obliged to everyone who has played for Keble College Darts Club during my time in Keble. I am grateful for all the friends who shaped the MCR and made it a great place.

Finally I want to thank all my teachers, tutors and professors on my path who have driven my interest to learn and research and guided my along the way.

Abstract

In order to further probe our understanding of the structure of matter and the universe, physicists constantly strive to create particle colliders that reach higher energies and luminosities. Improved technologies can partly help to fulfil these goals, however, novel experimental interaction region (EIR) optics and methods are also essential to this cause.

This thesis covers several optics issues and solutions applicable to the Large Hadron Collider (LHC), its High Energy (HE-LHC) upgrade as well as the Future Circular Collider (FCC-hh). A key tool presented in this thesis is an optimisation method to produce short final focus triplets that produce large integrated gradients whilst having an aperture sufficiently large to sustain the beams and radiation shielding.

The optimisation method uses a thin lens solution as a first approximation for the required quadrupole strength. This solution is outlined in the thesis, it has a large range of potential applications. This is demonstrated by using it to optimise the dynamic aperture of the Nuclotron-based Ion Collider fAcility (NICA), which is severely impacted by quadrupole fringe field effects.

An optimised triplet for the FCC-hh is integrated into the EIR and the

resulting optics as well as the general impact it has on the machine is presented in this thesis. It also presents how the LHC EIR can be modified for the HE-LHC, including the implementation of an optimised triplet. Dynamic aperture studies of the HE-LHC with triplet field errors were also performed in the scope of this work.

Finally, a ballistic alignment optics for the LHC will be presented as well as a method that uses singular value decomposition to measure the offset of modulated quadrupoles. It will also be illustrated how this method can be used to improve the accuracy to optics measurements. These efforts can be used to improve the stability and luminosity of the LHC.

Contents

List of Figures

Chapter 1

Theory of Beam Physics

1.1 Single Particle Motion

1.1.1 Charged Particles in Fields

The underlying principle in all particle accelerators is the interaction of charged particles with electromagnetic fields. These fields can be used to accelerate but also steer particles so that they can reach large kinetic energies, whilst being guided through the machine. The force $\mathbf{F}$ a particle with charge q experiences when travelling through an electric field $\mathbf{E}$ and magnetic field $\mathbf{B}$ at a velocity $\mathbf{v}$ is called the Lorentz force and can be expressed as [1, p. 3]

$$\mathbf{F} = q(\mathbf{v} \times \mathbf{B} + \mathbf{E}). \tag{1.1}$$

Since the magnetic component of the Lorentz force $q\mathbf{v} \times \mathbf{B}$ acts perpendicular to the direction of travel it does not change the energy of the particle. Therefore, only electric fields are used to accelerate particles to high energies. The energy, ΔE, a particle gains when travelling from one point $\mathbf{r_1}$ to another point $\mathbf{r_2}$ is equal to the integral of the force along the trajectory [1]

$$\Delta E = \int_{\mathbf{r_1}}^{\mathbf{r_2}} \mathbf{F}(\mathbf{r}) \cdot d\mathbf{r} = q \int_{\mathbf{r_1}}^{\mathbf{r_2}} \mathbf{E}(\mathbf{r}) \cdot d\mathbf{r} = qV, \tag{1.2}$$

where V is the potential difference across the trajectory. Hence, the energy gain, in electronvolt, for a particle with the elementary charge, e, is equal to the potential difference across the field it travels through.

Since it is impossible to achieve a perfect vacuum, the highest obtainable electric fields are limited by the dielectric strength of the vacuum. Even for the best vacuum the highest static fields before breakdown are typically around $10^5\ \mathrm{V\,m^{-1}}$ [2]. On the other hand, particles in accelerators tend to have large kinetic energies and velocities close to the speed of light, $c = 3.0\ \times 10^8\ \mathrm{m\,s^{-1}}$. Therefore, even for fields of around 1 T, the product $|\mathbf{v} \times \mathbf{B}| \approx 10^8 - 10^9\ \mathrm{V\,m^{-1}}$, making the magnetic component much larger than the electric component. Hence, even though magnetic fields cannot be used to increase the energy of particles they are highly effective for steering particles at high energies.

1.1.2 Natural Coordinates

In order to simplify the electrodynamics for accelerators, it is convention not to use classical Cartesian coordinates but to define a co-moving system [3, p. 44-47]. In this system the s axis is aligned with the trajectory an ideal particle would take through the accelerator. The x and y axes are perpendicular to the s axis at every point and lie in the horizontal and vertical planes respectively. A schematic of this system is shown in Figure 1.1.

By using this coordinate system one can apply the chain rule to convert time derivatives into spatial derivatives by realising that for any function f the time deriva-

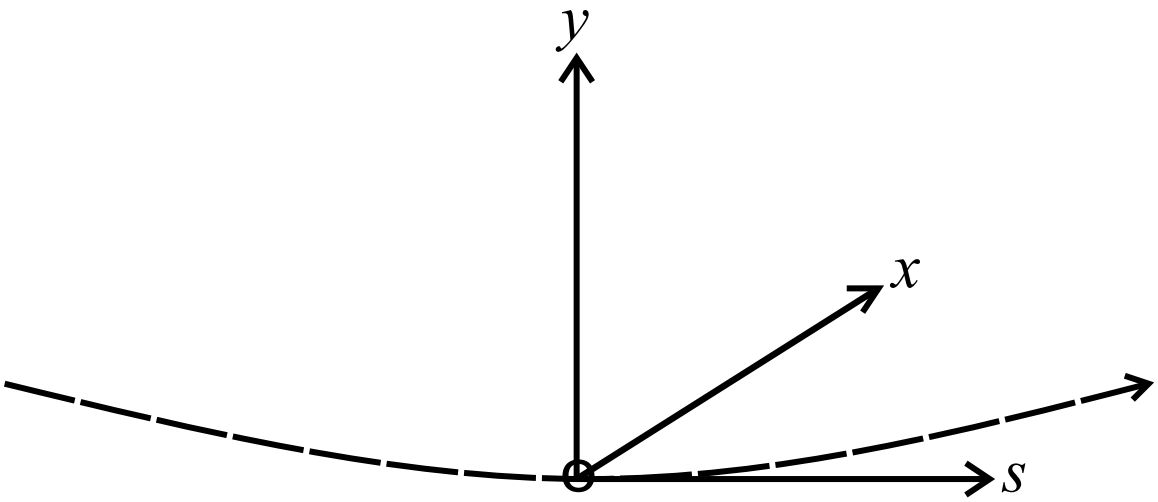

Figure 1.1: Diagram showing base vectors of co-moving coordinate system at a given point along the design trajectory represented by the dashed line.

tive $\dot{f}$ can be expressed as

$$\dot{f} = \frac{df}{dt} = \frac{df}{ds}\frac{ds}{dt} = f'v, \tag{1.3}$$

where f' is the spatial derivative and v is the speed along the s axis. This system is more natural as it describes the dynamics of the particles as a function of its position in the accelerator rather than with respect to time.

In this coordinate system, and using the approximation $\mathbf{v} \approx \big(v, 0, 0\big)$ the Lorentz force in a magnetic field can be expressed as

$$\mathbf{F} = m\ddot{\mathbf{r}} = mv^2 r'' = q\mathbf{v} \times \mathbf{B} = q \begin{pmatrix} v \\ 0 \\ 0 \end{pmatrix} \times \begin{pmatrix} B_s \\ B_x \\ B_y \end{pmatrix} = qv \begin{pmatrix} 0 \\ B_y \\ -B_x \end{pmatrix}, \tag{1.4}$$

where m is the mass of the particle.

From this one can extract equations of motion in the $\mathbf{x}$ and $\mathbf{y}$ planes to be

$$\begin{aligned} x'' &= \frac{q}{mv}B_y = \frac{q}{p}B_y = \frac{1}{B\rho}B_y, \\ y'' &= \frac{-q}{mv}B_x = \frac{-q}{p}B_x = \frac{-1}{B\rho}B_x, \end{aligned} \tag{1.5}$$

respectively. In Equations 1.5, p is the longitudinal momentum mv and the quantity $B\rho \equiv \frac{p}{q}$ is defined as the beam rigidity – a quantity describing the particle resistance

to the effect of a magnetic field [4, p. 24-26]. The rigidity depends on the particle's mass and charge but also the momentum it has been accelerated to.

In order to solve the dynamics analytically the equations are often linearised. The first step in doing this is performing a Taylor expansion of the right hand side of Equations 1.5. For the horizontal plane this would be

$$x'' = \frac{1}{B\rho}B_y = -\frac{1}{B\rho}\left(B_{y,0} + \left[\frac{dB_y}{dx}\right]_0 \frac{x}{1!} + \left[\frac{d^2B_y}{dx^2}\right]_0 \frac{x^2}{2!} + \left[\frac{d^3B_y}{dx^3}\right]_0 \frac{x^3}{3!} + ...\right) = \\ = \left(\frac{1}{R} + \frac{k}{1!}x + \frac{m}{2!}x^2 + \frac{o}{3!}x^3 + ...\right). \tag{1.6}$$

An ideal particle has $x = 0$ and will therefore experience an acceleration equal to $\frac{-B_{y,0}}{B\rho}$. Since for an ideal particle, the co-moving coordinates has to result in x remaining zero, it has to result in a centrifugal force countering this effect. The centrifugal force is given as $F = \frac{mv^2}{R}$, where R is the radius of curvature — this results in $x'' = \frac{1}{R}$. Therefore, in Equation 1.6, the convention $\frac{-B_{y,0}}{B\rho} \equiv \frac{1}{R}$ is used. The other component, k, m and o are the normalised quadrupole, sextupole and octupole components of the magnetic field [3, p. 44-46]. Often this equation is truncated at the linear quadrupole term to simplify the equations, however higher order terms are found in accelerators and have to be dealt with separately.

1.2 Elements in Synchrotrons

In this section the different electromagnetic components that can be found in an accelerator will be described. First, it will take a closer look at dipoles and quadrupoles and show how the dynamics can be linearised by only considering these components. It will then outline the boundary conditions found in a synchrotron and how these affect the dynamics. Next it will describe the effect of higher order static magnetic

elements before briefly describing radio frequency cavities.

1.2.1 Dipoles

A dipole magnet produces a field that is uniform and constant throughout its aperture. This field is formed using two magnetic poles and causes all particles to be deflected in the same direction. This property makes it convenient to use dipoles to steer the trajectory of the entire beam and to define the geometry of the co-moving coordinates around them. Whilst a particle that has the correct longitudinal momentum and lies on the ideal trajectory will remain on this trajectory as it passes through a dipole, the dynamics are more complex if the particle is not on the ideal trajectory.

In an ideal dipole, only the $\frac{1}{R}$ dipole component of Equation 1.6 governs the dynamics of the beam and is cancelled by the centrifugal force which is also equal to $\frac{1}{R}$. A small deviation from the ideal orbit by x causes a change in the bending radius causing this component to be $\frac{1}{R+x}$, this can be linearised by using a binomial expansion and then truncating the results as followed

$$x'' = \frac{1}{R+x} = \frac{1}{R}\left(\frac{1}{1+\frac{x}{R}}\right) \approx \frac{1}{R}\left(1-\frac{x}{R}\right) = \frac{1}{R} - \frac{x}{R^2}. \tag{1.7}$$

This effect is often referred to as weak focusing as it produces a force in the opposite direction of the offset, however, this effect is a lot weaker than the focusing effect from quadrupoles. Another effect one has to consider are chromatic effects when a particle has a small offset in longitudinal momentum, Δp. In this case the $\frac{q}{p}B_y$ has to be corrected to $\left(\frac{q}{p+\Delta p}\right)B_y$, a similar linearisation as in Equation 1.7 can be performed to come up with a full equation of motion for this system. The full equation of motion

also requires to subtract the centrifugal $\frac{1}{R}$ resulting in

$$x'' = -\frac{x}{R^2} + \frac{1}{R}\frac{\Delta p}{p}. \tag{1.8}$$

In principle this could be repeated in the vertical plane, however, dipoles are almost always used to steer beams in the horizontal plane for example in synchrotron arcs or to manipulate the inter-beam separation. One exception to this are dipole kickers that can be used to correct orbit distortions caused by imperfections or to induce offsets from reference orbit.

1.2.2 Quadrupoles

Quadrupoles are magnets that are constructed by using four equidistant alternating magnetic poles and produce a field in which the strength varies linearly with the distance from the centre. The exact nature of this field depends on the orientation of the quadrupole but the most common configuration produces a magnetic field described by

$$\begin{pmatrix} B_s \\ B_x \\ B_y \end{pmatrix} = \begin{pmatrix} 0 \\ -Gy \\ Gx \end{pmatrix}, \tag{1.9}$$

where G is the constant gradient of the field. A useful property of this field is that the resulting forces in the horizontal and vertical planes depend on the displacement in the respective planes — thereby resulting in a focusing force whilst keeping the equations of motion uncoupled.

The value of the gradient G depends on the strength of the field that can be achieved at the poles as well as the distance between the poles. The simplest approximation for this is that

$$G \approx \frac{B_{MAX}}{r}, \tag{1.10}$$

where B_{MAX} is the highest achievable field with the magnet technology available and r is the radius of the aperture of the magnet. The normalised quadrupole strength k relates to the gradient as $k = \frac{G}{B\rho}$. As one can see from Equation 1.9, the strengths in both planes are intrinsically linked such that $k_x = -k_y \equiv k$. Therefore, when adding this term to the equations of motion in both planes one gets

$$\begin{aligned} x'' + \left(\frac{1}{R^2} - k\right) x &= \frac{1}{R}\frac{\Delta p}{p}, \\ y'' + ky &= 0. \end{aligned} \tag{1.11}$$

If k is negative it has a focusing effect in the horizontal plane because it results in a force that is in the opposite direction of the offset, at the same time this has a defocusing effect in the vertical plane. This is reversed when k is positive. Therefore, quadrupoles of alternating gradient are commonly used to manipulate the beam in both planes.

1.2.3 Solution to Linear Equations

From Equations 1.11 one can see that in an ideal lattice made of perfect quadrupoles and dipoles would be sufficient for controlling the beams. It provides a means of guiding the beam using dipoles but also focusing it using a combination of quadrupole magnets. Moreover, these linear equations can be solved analytically, making it simpler to design a lattice using these magnets.

For an on momentum particle Equations 1.11 can be summarised as

$$z'' + Kz = 0, \tag{1.12}$$

where z can be x or y and $K = \left(\frac{1}{R^2} - k\right)$ in the horizontal and $K = k$ in the vertical plane. Oscillatory equations of motion in this form are commonly found in physics

and it is referred to as the Hill differential equation. The solution to the Hill equation is well studied and takes the form [5]

$$\begin{aligned} z(s) &= \sqrt{j_z \beta_z(s)} \cos\left[\mu_z(s) - \mu_{z,0}\right], \\ z'(s) &= -\sqrt{\frac{j_z}{\beta_z(s)}} \left(\sin\left[\mu_z(s) - \mu_{z,0}\right] + \alpha_z(s) \cos\left[\mu_z(s) - \mu_{z,0}\right]\right), \end{aligned} \tag{1.13}$$

with

$$\mu_z(s) = \int_{s_0}^{s} \frac{ds'}{\beta_z(s')} \tag{1.14}$$

and

$$\alpha_z \equiv \frac{-\beta_z'}{2}. \tag{1.15}$$

One can interpret this solution as a sinusoidal oscillation around $z = 0$ with an envelope $\sqrt{j_z \beta_z(s)}$. β_z, α_z and μ_z are known as the Twiss functions and depend solely on magnets in the machine whilst j_z and $\mu_{z,0}$ encapsulate the initial conditions of the particle. The envelope of the oscillations depends on machine properties and initial conditions, whilst the frequency of the oscillations varies as a property of the machine.

Substituting this solution into the original equation of motion yields a differential equation for β_z

$$\frac{1}{2}\beta_z \beta_z'' - \frac{1}{4}\beta_z'^2 + K\beta_z^2 = -\beta_z \alpha_z' - \alpha_z^2 + K\beta_z^2 = 1. \tag{1.16}$$

The solutions to this differential equation depends only on machine parameters and not on the initial conditions of the particle. If one knows the β_z function and its derivatives at a given point one can use these to compute the functions at a point downstream.

The initial conditions,z_0 and z_0', of the particle can be be used to solve for j_z and $\mu_{z,0}$, which leads to a system in which matrices of the position and momentum downstream are described through a transformation acting on a vector containing the initial conditions of the particle. The general expression is

$$\begin{pmatrix} z(s) \\ z'(s) \end{pmatrix} = \begin{pmatrix} C(s) & S(s) \\ C'(s) & S'(s) \end{pmatrix} \begin{pmatrix} z_0 \\ z_0' \end{pmatrix} = \mathbf{M} \begin{pmatrix} z_0 \\ z_0' \end{pmatrix}, \tag{1.17}$$

where the $S(s) = \sqrt{\frac{\beta_z(s)}{\beta_{z,0}}}(\cos\mu_z(s) + \alpha_{z,0}\sin\mu_z(s))$ and $C(s) = \sqrt{\beta_z(s)\beta_{z,0}}\sin\mu_z(s)$ [6, p. 28-30]. A common transfer matrix is that of a field free drift, in this case $C(s) = 1$ and $S(s) = s$. For a drift of length l this leads to a matrix

$$\mathbf{M_{Drift}} = \begin{pmatrix} 1 & l \\ 0 & 1 \end{pmatrix}. \tag{1.18}$$

Two other common matrices are those of a focusing ($K > 0$) and defocusing ($K < 0$) segments of length l, these matrices are

$$\begin{aligned} \mathbf{M_F} &= \begin{pmatrix} \cos(\sqrt{|K|}l) & \frac{1}{\sqrt{|K|}}\sin(\sqrt{|K|}l) \\ -\sqrt{|K|}\sin(\sqrt{|K|}l) & \cos(\sqrt{|K|}l) \end{pmatrix}, \\ \mathbf{M_D} &= \begin{pmatrix} \cosh(\sqrt{|K|}l) & \frac{1}{\sqrt{|K|}}\sinh(\sqrt{|K|}l) \\ \sqrt{|K|}\sinh(\sqrt{|K|}l) & \cosh(\sqrt{|K|}l) \end{pmatrix}, \end{aligned} \tag{1.19}$$

respectively [4, p. 38-40]. In the limit of $l \to 0$, these matrices converge to the thin lens approximation yielding

$$\mathbf{M_{thin,F}} = \begin{pmatrix} 1 & 0 \\ -Kl & 1 \end{pmatrix}, \mathbf{M_{thin,D}} = \begin{pmatrix} 1 & 0 \\ Kl & 1 \end{pmatrix}. \tag{1.20}$$

The properties of an accelerator can be computed by multiplying a series of matrices representing the individual components to obtain the overall transfer matrix of the machine. The particle dynamics can then be calculated from the initial conditions of the particles. In addition to using this to design an accelerator, one can also

use these transfer matrices to measure the properties of a machine. To do this the beam can be excited using a controlled dipole kick and the oscillations downstream can be measured to compute the transfer matrix and compare it to the design for corrections [7].

The solutions outlined above are for the homogeneous equation that sets $\Delta p = 0$. For the full solution, the particular solution yielding $\frac{1}{R}\frac{\Delta p}{p}$ has to be found. This is commonly done by finding the particular solution $D(s)$, which is often referred to as the dispersion function, for the case where $\frac{\Delta p}{p} = 1$ so that a general solution can be expressed as $D(s)\frac{\Delta p}{p}$. The differential form of this solution is [6, p. 37-38]

$$D'' - \left(k - \frac{1}{R^2}\right) D = \frac{1}{R} \tag{1.21}$$

and the solution to this is

$$D(s) = S(s) \int_{s_0}^{s} \frac{C(s')}{R(s')} ds' - C(s) \int_{s_0}^{s} \frac{S(s')}{R(s')} ds'. \tag{1.22}$$

This can be calculated along the accelerator and added to Equation 1.13 to obtain the full solution

$$\begin{aligned} z(s) = z_0(s) + D(s)\frac{\Delta p}{p} = \sqrt{j_z \beta_z(s)} \cos\left[\mu_z(s) - \mu_{z,0}\right] + D(s)\frac{\Delta p}{p}, \\ z'(s) = z_0'(s) + D'(s)\frac{\Delta p}{p} = \\ = -\sqrt{\frac{j_z}{\beta_z(s)}} \left(\sin\left[\mu_z(s) - \mu_{z,0}\right] + \alpha_z(s) \cos\left[\mu_z(s) - \mu_{z,0}\right]\right) + D'(s)\frac{\Delta p}{p}, \end{aligned} \tag{1.23}$$

where $z_0(s)$ and $z_0'(s)$ are the position and transverse momentum of an on momentum particle and $D'(s) \equiv \frac{dD(s)}{ds}$.

1.2.4 Closed Orbit

The linear equations in section 1.2.3 are dependant on the initial conditions and outline how the different elements affect the motion. The initial conditions depend on the source and are not easy to define or measure. A special case arises in a synchrotron, which is an accelerator that is designed to close on itself. In a synchrotron, the beam reaches an equilibrium state in which it follows an orbit that might not be the same as the design orbit but closes on itself. This orbit is referred to as the closed orbit [4, p. 2]. The closed orbit $\mathbf{z_{co}}$ at any point is defined as

$$\mathbf{M}\begin{pmatrix} z_{co} \\ z'_{co} \end{pmatrix} = \begin{pmatrix} z_{co} \\ z'_{co} \end{pmatrix}, \tag{1.24}$$

where $\mathbf{M}$ is the transfer matrix over one revolution.

In this case the periodicity $\beta_z(s + C) = \beta_z(s)$ and $\alpha_z(s + C) = \alpha_z(s)$, where C is the circumference of the synchrotron, becomes the initial condition required for the solution of the differential equations. This is often solved numerically by defining all the elements in an accelerator and solving the dynamics through iterative calculations [8, p. 127-137]. Once this is solved, one can evaluate the Twiss functions at any point of the lattice and one can also define the transfer matrix, $\mathbf{M}$, for one revolution at any point of the lattice as [9, p. 18]

$$\mathbf{M} = \begin{pmatrix} \cos(2\pi Q_z) + \alpha_z \sin(2\pi Q_z) & \beta_z \sin(2\pi Q_z) \\ -\sin(2\pi Q_z) & \cos(2\pi Q_z) - \alpha_z \sin(2\pi Q_z) \end{pmatrix}. \tag{1.25}$$

An important parameter used in this expression is the phase advance, μ_z, over one revolution in units of 2π – this phase advance is referred to as the tune, Q_z, of the

machine and is defined as [10, p. 318-319]

$$Q_z = \frac{\mu_z(C)}{2\pi} = \frac{1}{2\pi}\oint_{s_0}^{s_0+C} \frac{ds'}{\beta_z(s')}. \tag{1.26}$$

Whilst the tune describes how many betatron oscillation a particle undergoes when travelling around the ring once, we are often more interested in the non-integer part of the tune as this describes how the particle's location in phase space changes every time it travels through the accelerator.

The closed orbit is also important when considering the effect of small linear perturbations, such as dipole kicks or changed quadrupole fields, on the orbit and tune of the machine. These effects can be unwanted or purposely induced in order to obtain information about the lattice. One such effect is the so called k-modulation of a quadrupole — in this process the current through a quadrupole is modulated to result in a change of k by Δk.

The effect this has on the lattice can be approximated using the thin lens matrix from Equation 1.20 with $K = \Delta k$ and multiplying it by $\mathbf{M}$. The new transfer matrix, $\mathbf{M_{new}}$, will be of the same form of $\mathbf{M}$ but with $Q_z \to Q_z + \Delta Q_z$. Since $\mathbf{M_{new}}) = \mathbf{M}\mathbf{M_{thin}}$, one can equate the traces $\mathrm{Tr}(\mathbf{M_{new}}) = \mathrm{Tr}(\mathbf{M}\mathbf{M_{thin}})$ to yield [9, p. 19]

$$2\cos(2\pi(Q_z + \Delta Q_z)) = 2\cos(2\pi Q_z) - \beta_z(\pm\Delta k l)\sin(2\pi Q_z), \tag{1.27}$$

where l is the length of the quadrupole and $\pm$ is $+$ in the x plane and $-$ in the y plane. This can be rearranged to form an expression for β_z in terms of Δk and ΔQ, which can be easily measured,

$$\beta_z = \pm\frac{2}{\Delta k l}(\cot(2\pi Q_z)[1 - \cos(2\pi\Delta Q_z)] + \sin(2\pi\Delta Q_z)) \approx \pm 4\pi\frac{\Delta Q_z}{\Delta k l}. \tag{1.28}$$

This method is useful to get very precise measurements of the average β functions within a quadrupole. The modulation of the quadrupole also has an effect on the location of the closed orbit if the quadrupole is misaligned by an amount z_q or the beam does not pass through the centre due an orbit error or bump of z_q. To analyse this case one can define $\hat{\mathbf{M}}$ as the transfer matrix from the exit of the quadrupole to the entrance of the quadrupole

$$\hat{\mathbf{M}} = \mathbf{M}_{\mathbf{quad}}^{-\mathbf{1}}\mathbf{M}, \tag{1.29}$$

where the quadrupole again has been approximated as a thin lens with a transfer matrix $\mathbf{M}_{\mathbf{quad}}$. The misalignment of the quadrupole causes a kick equal to $\mp klz_q$ for $z = x$ and $z = y$ respectively. Therefore, Equation 1.24 can be expressed as [11]

$$\hat{\mathbf{M}} \begin{pmatrix} z_{co} \\ z'_{co} \mp klz_q \end{pmatrix} = \begin{pmatrix} z_{co} \\ z'_{co} \end{pmatrix}. \tag{1.30}$$

Next one can perturb the system by increasing $k \to k + \Delta k$ and labelling the change in closed orbit as Δz_{co} and $\Delta z'_{co}$. to get

$$\hat{\mathbf{M}} \begin{pmatrix} \Delta z_{co} \\ \Delta z'_{co} \mp \Delta klz_q \mp (k + \Delta)l\Delta z_{co} \end{pmatrix} = \begin{pmatrix} \Delta z_{co} \\ \Delta z'_{co} \end{pmatrix}. \tag{1.31}$$

By substituting in Equation 1.25 one can show that at the exit of the quadrupole

$$\begin{aligned} \Delta z_{co} &= \mp z_q \frac{\beta_z \cot(\pi Q_z)\Delta kl}{2 + \beta_z \cot(\pi Q_z)\Delta kl}, \\ \Delta z'_{co} &= \mp z_q \frac{\left[1 - \alpha_z \cot(\pi Q_z)\right]\Delta kl}{2 + \beta_z \cot(\pi Q_z)\Delta kl}. \end{aligned} \tag{1.32}$$

1.2.5 Higher Order Effects and Corrections

In reality, momentum offsets, field errors and misalignments can cause non-linear effects that have to be dealt with. The first such effect arises from quadrupole fields

that are not orientated in the same way as assumed in Equation 1.9 – this might arise from misalignments or errors in the magnetic fields. In this case an offset in the horizontal plane causes a kick in the vertical plane and vice versa. This causes complications because the equations of motion for both planes become coupled.

This coupling can be linearised which leads to coupling matrices that describe how the motion in one plane affects that in the other, in an analogous way to the single plane transfer matrices. In practice this coupling can be measured and then corrected for using special skew quadrupoles that have been rotated by 45° around the s axis and counter the unwanted coupling.

Another effect left out in the linearisation in Equation 1.11 is the effect quadrupole fields have on off-momentum particles. A similar binomial expansion as used in Section 1.2.1 can be performed to obtain a $\mp k\frac{\Delta p}{p}z$ term. This term essentially indicates that particles with a higher momentum experience a lower (de-)focusing effect than particles with a lower momentum.

The fact that particles at different energies experience different focusing effects means that the synchrotron tune of a single particle depends on its energy. The chromaticity of a machine, Q'_z, is the measure of how much the tune varies with energy. It is defined as $Q'_z \equiv \frac{\partial Q_z}{\partial(\Delta p/p)}$ and it can be shown to be [10, p. 323]

$$Q'_z \equiv \frac{\partial Q_z}{\partial(\Delta p/p)} = \mp\frac{1}{4\pi}\oint k(s)\beta_z(s)ds. \tag{1.33}$$

This chromatic effect is often cancelled using sextupole magnets that produce a Lorentz force kick of the form $\frac{m}{2}z^2$. One can substitute the orbit of an off-momentum

particle given in Equation 1.23 into this expression to get

$$z'' = \frac{m}{2}\left(z_0 + D\frac{\Delta p}{p}\right)^2 = \frac{m}{2}z_0^2 + m\left(D\frac{\Delta p}{p}\right)z_0 + \frac{m}{2}\left(D\frac{\Delta p}{p}\right)^2. \tag{1.34}$$

In this expression the second term results in a quadrupole like term with a strength $m\left(D\frac{\Delta p}{p}\right)$, this strength is proportional to the chromatic term and can be used to cancel this. This gives rise to second order terms in z and Δp, however, these can be cancelled by using combinations of differently powered sextupoles and optics that cancel these effects [3, p. 120-123].

Therefore sextupole families are used to reduce the chromaticity of the machine and make sure the particles have a low tune spread. It can be shown that with sextupoles the chromaticity is [10, p. 324]

$$Q'_z = \mp\frac{1}{4\pi}\oint (k(s) + m(s)D(s))\beta_z(s)ds, \tag{1.35}$$

this can be used to find the sextupole strengths required to bring the chromaticity to the desired value. For stability reasons this is often chosen to be a small positive value.

Another way to quantify the chromatic effects of a machine is with the chromatic amplitude function, W. This function is often referred to as Montague function and quantifies the local distortion of the Twiss functions due to momentum due to momentum offsets. The Montague function is defined as [12]

$$W_z = \frac{1}{2}\sqrt{\left(\frac{1}{\beta_z}\frac{\partial\beta_z}{\partial p}\right)^2 + \left(\frac{\partial\alpha_z}{\partial p} - \frac{\alpha_z}{\beta_z}\frac{\partial\beta_z}{\partial p}\right)^2}. \tag{1.36}$$

It is often not possible to produce magnets that have pure multipole fields, instead it is common to have a spectrum of unwanted multipole errors in a realistic magnet.

These field errors arise from systematic limitations from the design and the finite length of the magnets but can also be a result in uncertainties and errors in the manufacturing. If not compensated, these errors can distort the orbit and severely affect the stability of the beam.

When including these non-linear terms in the equation of motion, it can be shown that they result in orbit distorting terms, $c(b_n; p, q, l, m)$, on top of the linear solutions outlined in section 1.2.3. It can be shown that these terms are [13]

$$c(b_n; p, q, l, m) \equiv \int ds K_{n-1}(s) \beta_x^{p/2} \beta_y^{q/2} e^{\pm i[(p-2l)\mu_x \pm (q-m)\mu_y]}, \tag{1.37}$$

where K_{n-1} is the normalised multipole strengths as defined in Equation 1.6 corresponding to a 2-n polar field. q, p, l and m are non-negative integers where $q \in 2\mathbb{N}$, $p + q = n$, $0 \leq 2l \leq p$ and $0 \leq 2m \leq q$. A similar expression exists for resonances due to skew fields – in this case b_n is replaced with a_n, K_{n-1} is replaced with the corresponding normalised skew fields $K_{n-1}^{(s)}$ and $q \in 2\mathbb{N} - 1$. If the unwanted multipole fields in a machine are measured their effects can be cancelled out by using multipole correctors at a specific phase and strength to minimise these orbit distorting terms.

It should also be noted that when considering the effect of an error in a single location over multiple turns μ_z is replaced by $2\pi Q_z$. Since the $2\pi Q_z$ is multiplied by integers in the exponent we can see by inspection that the term grows if the non-integer part of the tune is a simple fraction. Therefore, it is common to run a synchrotron at a non-integer that is far away from simple fractions.

1.2.6 Radio Frequency Cavities

All of the components explored so far produce static magnetic fields in order to guide particles along a fixed path. However, sometimes one requires fields that vary with time. On the one hand this may allow one to achieve higher peak fields without breakdown but on the other hand it also creates fields that have a different effect on particles at different locations in the bunch, thereby controlling the longitudinal shape of the bunches and not just the transverse shape. These fields that vary in time are often achieved in the form of standing waves produced by exciting different harmonics in radio frequency (RF) cavities.

The most common type of RF cavity used in accelerators is an accelerating cavity. It produces large electric fields in the longitudinal direction that accelerates the particles in the beam as described in Equation 1.2. The standing wave produces a voltage across the cavity that varies in time as $V(t) = V_{max} \sin(2\pi f t)$, where V_{max} is the peak voltage and f is the frequency at which the electric field varies.

One would achieve the largest acceleration if all the particles pass through the cavity when $V(t) = V_{max}$, however, for stability reasons it is desirable to design the machine so that the individual bunches pass through an accelerating cavity slightly earlier or later than this [4, p. 57-62]. At lower momenta the ideal time the particles should pass through the cavity is slightly earlier and is illustrated by point A in Figure 1.2.

The benefit of this is that if a particle has slightly less than average energy it will be moving slightly slower. As a result of this the particle will reach the cavity

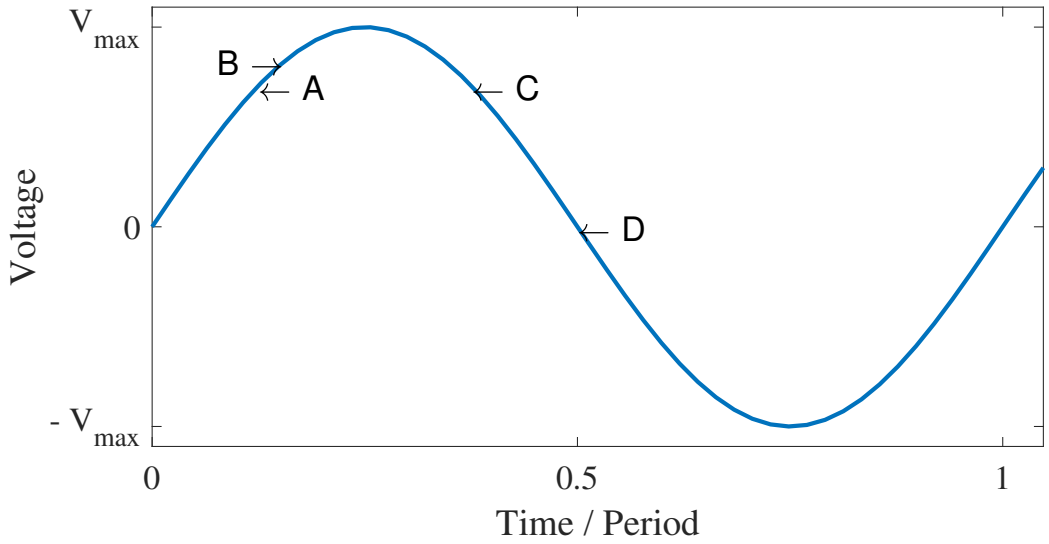

Figure 1.2: Voltage in an RF Cavity over one period. Points A, B and C indicate different phases in which bunches may pass through an accelerating cavity. Point D shows the ideal time to pass through a crab cavity.

slightly later, illustrated by point B in Figure 1.2. Therefore the particle with lower energy will experience a larger acceleration and catch up with the centre of the bunch, whilst particles with higher energies will experience a smaller acceleration. This effect provides buckets of stability, which cause particles to be in longitudinal bunches.

This effect breaks down when the velocity of the particles approaches the relativistic limit and the difference in speed is negligible. In this case the dispersion function causes particles with higher momenta to take a longer path resulting in them arriving later - the energy at which this starts happening is known as the transition energy. This is solved by changing the phase of the voltage in the cavities once this energy is reached so that the bunch passes through the cavity as the gradient of the voltage slopes down, this is represented in point C in Figure 1.2. This transition ensures that the bunches remain in longitudinally stable buckets.

Another, less common, type of cavity is the crab cavity – this cavity induces an electromagnetic kick in the transverse plane. It is phased in a way such that particles in the centre of the bunch do not experience a kick, this is represented by point D in Figure 1.2. Particles either end of the centre experience kicks in opposite directions proportional to their distance from the centre. This cavity causes the bunch to essentially experience a kick turning it around its longitudinal centre, the purpose of this will be explained in section 1.4.

1.3 Synchrotron Conventions

1.3.1 Common Optics Structures

As discussed above, synchrotrons are designed to guide the beam on a trajectory that closes on itself; this is done using a series of dipole magnets often arranged in several arcs. In order to keep the beam focused, alternating gradient quadrupoles are added in these arcs. The most common way of of doing this is through equally spaced quadrupoles with opposite and equal strengths. These periodically repeating structures are referred to as FODO cells [14].

The FODO cell gets its name from the fact that it consists of a focusing (F) and de-focusing (D) quadrupole with drifts (O) filled with dipoles in between. The β functions in a FODO cell are anti-symmetric in the two planes and are often matched to produce a fixed phase advance, μ. The fraction of a FODO cell occupied by dipoles is known as the fill factor. A larger fill factor means that a smaller dipole field is required to bend the beam by the required amount.

Apart from arcs, synchrotrons also have straight sections that can be used to house

insertion regions (IRs) that fulfil different purposes such as injection and extraction, collimation or acceleration. In colliders there are also IRs dedicated for the collisions, such an IR is known as an Experimental Interaction Region (EIR).

1.3.2 Beam Emittance and Size

Section 1.2.3 outlines the motion of a single particle where the exact position and momentum depend on the particle properties $\mu_{z,0}$ and j_z. In a real bunch the individual particles have different initial conditions resulting in a distribution of $\mu_{z,0}$ and j_z. One way of characterising this distribution is by measuring the root mean square (RMS) size of the beam $< z^2 >$. By calculating this for the expression of z in Equation 1.13 whilst assuming $\mu_{z,0}$ is distributed uniformly one can show that [15]

$$< z^2 >= \frac{< j_z >}{2}\beta_z = \epsilon_z\beta_z, \tag{1.38}$$

where we have defined $\frac{<j_z>}{2} \equiv \epsilon_z$. It can also be shown that $< z'^2 >= \epsilon_z\gamma_z$, where $\gamma_z \equiv (1+\alpha_z^2)/\beta_z$.

Since the average position and momentum of the particles in the beam are zero these averages correspond to the variance and it is therefore common to approximate the beam size and divergence as the standard deviations σ_z and $\sigma_{z'}$ respectively where

$$\sigma_z(s) = \sqrt{\epsilon_z\beta_z(s)}, \sigma_{z'}(s) = \sqrt{\epsilon_z\gamma_z(s)}. \tag{1.39}$$

The emittance can be measured using various methods [16] and the Twiss functions are well defined by the magnets in a lattice so that the beam in an accelerator can be well described using these equations.

The emittance decreases if the energy of the particles increases, therefore, the

normalised emittance, $\bar{\epsilon} = \gamma_{rel}\beta_{rel}\epsilon$, where $\beta_{rel} = v/c$ and $\gamma_{rel} = (1 - \beta_{rel}^2)^{-1}$ is often used, this is conserved during acceleration [4, p. 45-49].

1.3.3 Beam Stay Clear

Another important property of an accelerator is the beam stay clear (BSC), defined as the distance from the centre of the beam to the wall of the vacuum chamber. It is usually measured in units of beam size and in one dimension can be expressed as [17]

$$N_z = \frac{L_z - t_z - k_\beta D_z \frac{\Delta p}{p}}{k_\beta \sigma_z}, \tag{1.40}$$

where L_z is the half width of the vacuum chamber and t_z is the alignment tolerance that is subtracted to give a safety margin. Another safety margin is provided by the β-beating factor k_β which summarises the uncertainty in the β function. This uncertainty $\frac{\Delta\beta}{\beta}$ is called β-beating as it propagates throughout the whole machine; based on this $k_\beta \equiv \sqrt{1 + \Delta\beta/\beta}$ since σ_z is proportional to $\sqrt{\beta_z}$.

In practice the vacuum chambers can have complex shapes and the BSC is not just evaluated in the x and y planes but at several angles. This is usually done by software that evaluates the β functions at many points along a magnet and then computes the BSC at several angles. These programs often also take into account other factors like the beam halo or offsets of individual elements [8, p. 153-164]. The minimum required BSC throughout the accelerator is known as the acceptance and is usually limited by the collimator setting and how much beam intensity one is able to afford to lose by tightening the collimators.

1.3.4 Dynamic Aperture

Another factor that limits the beam size is the dynamic aperture (DA). This is a measure of the range of particles, again usual in units of beam size, that can circulate the synchrotron without getting lost due to dynamic effects and non-linear imperfections. In an ideal linear machine the dynamic aperture would be infinite because all particles follow well defined paths. Once you add errors, however, these orbits can become unstable – since these dynamic effects are proportional to z^n particles with larger amplitudes, j_z, are more likely to be on these unstable orbits.

The DA is evaluated by tracking particles at different amplitudes travelling around the synchrotron up to ten million times and observing which particles remain on a stable orbit [18]. The tracking is done with simulated non-linear errors and using numerical integrators that are often symplectic, meaning that they do not truncate the equations of motion, an example for such a tracker is Sixtrack [19, 20].

In order to speed up the computation by orders of magnitude, several other methods have been developed that aim to predict stability using many orders of magnitude less turns. One method of how this can be done is by evaluating the Lyapunov exponent, $L(z_0)$, for particles with different initial conditions z_0. This method tracks two particles close to the point in phase space that is being sampled and evaluates the distance between them $d(z_0, t)$ at every turn, t. The Lyapunov exponent is then defined as [21, p. 60-64]

$$L(z_0, t) = \frac{1}{t} \ln \left| \frac{d(z_0, t)}{d(z_0, 0)} \right|. \tag{1.41}$$

For a stable region in the limit of $t \to \infty$, $L(z_0, t)$ should go to zero, therefore, the

change in $L(z_0, t)$ over many turns can be monitored and if it approaches zero it can be considered a stable point.

In order to further increase the computational efficiency, Sixtrack uses two variants of this method, namely the distance and the slope method [22]. Both methods also use data from tracking two initially close test particles, the distance method considers a position in phase space to be stable if the distance between the test particles does not exceed a certain threshold. The slope method measures the rate of change of separation on a log-log scale and assumes chaotic motion if this exceeds a certain threshold. The distance method is considered to be optimistic, whilst the slope method can be pessimistic, therefore, the commonly used dedicated post processing programme SixDesk calculates a phase space average of the two methods [23].

1.4 Experimental Interaction Regions (EIR)

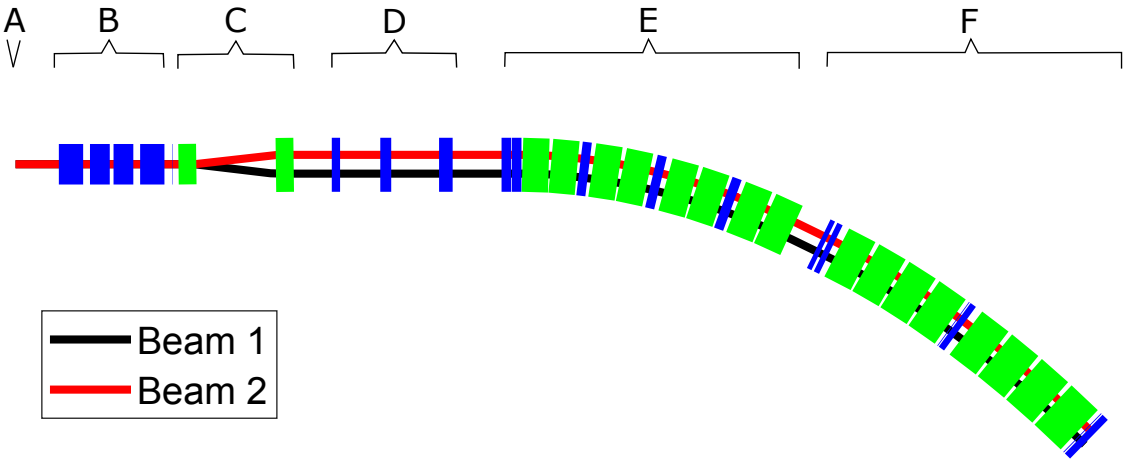

Figure 1.3: Diagram of a typical half of an Experimental Interaction Region – Quadrupoles represented in blue, dipoles in green. [Labels highlighting: A. Interaction Point, B. Triplet, C. Separation Dipoles, D. Matching Section, E. Dispersion Suppressor, F. First Arc FODO Cell.]

This thesis focuses on the design, optimisation and measurement of the EIRs in

various hadron synchrotrons. This section will outline the typical layout of such an EIR and give a brief overview of the different sections. A quick overview of a typical half of an EIR used in this thesis is shown in Figure 1.3.

1.4.1 Interaction Point

The interaction point (IP), shown as point A in Figure 1.3, is the location at which the two rotating beams collide and the interactions happen. The rate, N_r, at which these interactions happen depends on the cross section, σ, of the interactions and the collider luminosity, L, so that $N_r = L\sigma$. The cross-section is a quantity that represents the effective transverse area two particles must lie in in order to interact, it depends on all of the underlying physical interactions [24, p. 23-27]. The luminosity is a measure of the probability of particles interacting per unit time, for identical infinitely short beams it is expressed as [3, p. 25-27]

$$L_0 = \frac{fN^2}{4\pi\sigma_y\sigma_x}, \tag{1.42}$$

where f and N are the frequency of bunches colliding and number of particles per bunch respectively. It is common to measure the cross section, σ, in cm^2 and L in $\text{cm}^{-2}\text{s}^{-1}$. Often the average luminosity of a machine integrated over a time period is a useful quantity to know, this is known as the integrated luminosity, commonly measured in fb^{-1} (10^{39}cm^{-2}).

In order to prevent secondary collisions beyond the IP, the bunches are collided at an angle as shown in Figure 1.4. This angle is known as the crossing angle, θ, and is often measured in units of $\sigma_{z'}$ where z is the plane in which the crossing angle lies. As one can see in Figure 1.4 a) the crossing angle means that the bunches do not

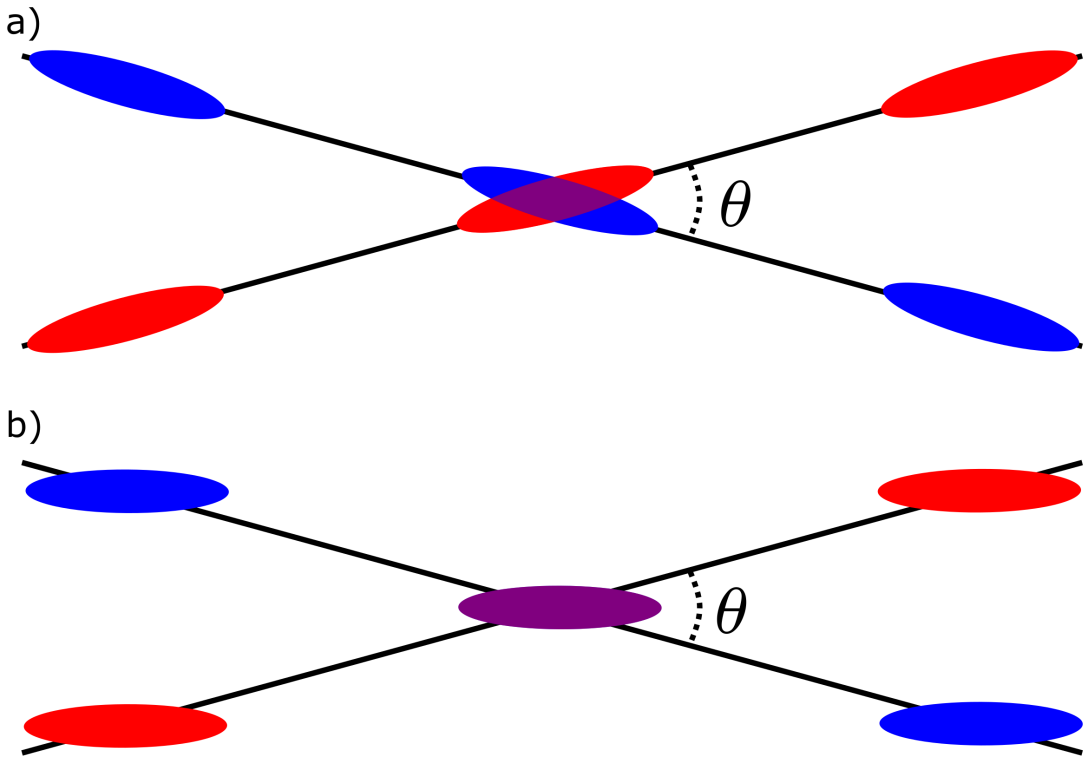

Figure 1.4: Diagramme showing bunches crossing at an angle and their overlap a) without and b) with crab cavities.

fully overlap at the IP, thus reducing the luminosity. The luminosity with crossing angle has to be corrected to $L = R_L L_0$ with [25]

$$R_L = \left[1 + \left(\frac{\sigma_s}{\sigma_z} \tan\frac{\theta}{2}\right)\right]^{\frac{-1}{2}}, \tag{1.43}$$

where σ_s is the longitudinal beam size.

In order to counter this geometric reduction the crab cavities outlined in Section 1.2.6 can be used to rotate the beams around an axis perpendicular to the crossing plane to regain the full overlap as shown in Figure 1.4 b). This twist can be achieved with a global crabbing scheme using a single cavity causing the bunches to rotate around themselves as they travel around the accelerator. However, it is more common to use a local scheme that kicks the beam just before it reaches the IP and

then kicks it just after in order to restore its original orientation. The equivalent crab cavity voltage, V_c, required either side of the IP to fully recover the luminosity is [26]

$$V_c = \frac{2cE_b \tan\frac{\theta}{2}}{2\pi f M_{12}(cc \to IP)} \frac{\sin(\pi Q_z)}{\sin(\mu_z[cc \to IP]\pi Q_z)}, \tag{1.44}$$

where c is the speed of light, E_b is the beam energy and $M_{12}(cc \to IP)$ and $\mu_z[cc \to IP]$ are the (1,2) transfer matrix element and phase advance in the crossing plane from the crab cavities to the IP.

1.4.2 Triplet

From Equation 1.42 one can see that the luminosity is inversely proportional to the beam sizes $\sigma_z = \sqrt{\epsilon_z \beta_z}$. Therefore, it is desirable to have the β functions at the IP to be as small as possible, this is usually achieved using strong focusing quadrupoles that are often arranged in a triplet, B in Figure 1.3. The β function at the IP is labelled β^* and it is common to design the accelerator so that the optics are symmetric around the IP so that $\alpha^* = 0$. The length of the drift between the IP and the start of the triplet is known as L^*, using this it can be shown that the β at the entrance of the triplet is [27]

$$\beta = \beta^* + \frac{L^{*2}}{\beta^*}. \tag{1.45}$$

From Equation 1.45 one can see that a small β^* results in very large β functions in the triplet. This puts strong constraints on the minimum aperture of the triplet magnets, this is worsened by the fact that the beams are on the same reference orbit at that point, meaning that they pass through the same magnet aperture. From Equation 1.10 we can see that the larger the aperture, the weaker the gradient meaning that long quadrupole magnets are needed in order to get a large focusing effect.

Since the β functions and strengths in the triplet are very large it is one of the biggest sources of chromaticity and non-linear resonance driving terms meaning it is favourable to have shorter triplets with smaller β functions.

In this thesis the common convention of numbering the quadrupoles starting from the closest to the IP will be adopted. The innermost quadrupole is labelled Q1, the next one Q2 and so on. Sometimes quadrupoles are split for practical reasons, in this case the sub-magnets are labelled alphabetically – i.e. Q1a, Q1b etc.

Final focus triplets are often used in hadron colliders with round beams, since they help to reduce the β functions equally in both planes. However, in electron-positron colliders, where the beams are usually flat due to radiation damping, it is more common to use a quadrupole doublet. The innermost quadrupole usually focuses in the vertical plane and the second quadrupole in the horizontal [28].

1.4.3 Separation Dipoles

In the arcs and most of the synchrotron, the two beams follow different reference orbits and often also move through separate magnet apertures. However, in order to collide they have to be put on the same reference orbit — this is usually done using a pair of separation dipoles, shown in section C in Figure 1.3. As seen from the IP the inner dipole, D1, separates both beams using a magnet with a single large aperture. The second dipole, D2, steers the particles back onto parallel orbits.

Unlike the arc dipoles, the separation dipoles steer the beams in opposite directions, therefore if the beams circulate in different apertures there will be a large magnetic flux through the separation between the two apertures in D2. This po-

tentially limits the aperture size of D2; the aperture in D1 is usually limited by the mechanical stress the dipole can tolerate. The integrated dipole field required to separate the beams depends on the beams separation in the arc as well as the distance between D1 and D2.

1.4.4 Matching Section

The triplet focuses the large β functions down again, however, these optics then have to be matched to be compatible with the arc. This is achieved with a set of individually powered quadrupoles in the matching section, D in Figure 1.3. The strengths of these quadrupoles can be matched using special algorithms that are often built into simulation software like MADX [8, p. 138-151]. These algorithms use numerical methods to vary the strengths of the quadrupoles systematically in order to get the desired Twiss functions at the exit. This process is called matching.

1.4.5 Dispersion Suppressor

The quadrupoles in the matching section would provide enough free parameters to match the α and β functions in both planes. In addition to that, it is also good to have no dispersion in the IP in order to keep the beam size as small as possible. The arc FODO cells have some intrinsic dispersion, hence, a group of quadrupoles and dipoles known as the dispersion suppressor (DS) are installed. One half of the DS is installed either side of the IP at the interface between the arc and EIR, labelled as E in Figure 1.3.

Traditionally, there are three different methods of designing and matching a DS and all of these have advantages and disadvantages [29, p. 198-206]. A straight

forward way of doing it is to construct a DS half out of three arc FODO cells but with individually powered quadrupoles. The quadrupole strengths can then be varied to match the dispersion, its derivative and the Twiss functions. The advantage of this method is that it is very flexible and does not alter the geometry. However, powering the quadrupoles individually can be costly and this method usually results in β functions and quadrupole strengths much larger than those in the FODO cells leading to aperture and magnet constraints.

The half-bend method does not require individually powered quadrupoles and has the same β functions as the arc. It suppresses the dispersion by installing special dipoles with half the normal strength in two or three FODO cells, depending on the phase advance in the cells. The downside of this is that the half strength dipoles have to be especially made for this and they have a big impact on the geometry, on top of that, it only works for 60° and 90° phase advance FODO cells. The missing-bend DS works in a similar way, by introducing FODO cells that have no bending magnets. In practice it is sometimes better to use a method that combines features of all three methods to have a small impact on the geometry but keep the β functions reasonable.

Chapter 2

Introduction

This chapter aims to provide an overview of the machines studied in the scope of this thesis. It will start off with looking at the Large Hadron Collider (LHC), outlining the motivations for building it and describing the overall design layout before taking a closer look at the EIR. It then gives a brief overview of possible future colliders before going into further detail on the future colliders studied in the scope of this thesis. An overview of the parameters of the colliders studied in this thesis is shown in Table 2.1.

Parameter	LHC	HL-LHC	HE-LHC	FCC-hh	NICA
Circumference [km]	27	27	27	100	0.5
Arc Dipole Field [T]	8.33	8.33	16	16	1.8
Beam Energy [TeV]	7	7	13.5	50	0.013
$\bar{\epsilon}_{x,y}$ [πµmrad]	3.5	2.5	2.5	2.2	5.7
Bunch Population N_b	1.5×10^{11}	2.2×10^{11}	2.2×10^{11}	1.0×10^{11}	6.1×10^{9}
$\beta^*_{x,y}$ [m]	0.55	0.15	0.45	0.3	0.6
Crossing angle [µrad]	285	590	330	176	0
Peak Luminosity [$\mathrm{cm}^{-2}\mathrm{s}^{-1}$]	1.18×10^{34}	19.5×10^{34}	28×10^{34}	30×10^{34}	1×10^{32}
Final Drift, L^* [m]	23	23	23	40	5.25

Table 2.1: Table showing design parameters of colliders studied in this thesis including LHC (design), HL-LHC (standard), HE-LHC, FCC-hh (ultimate) and NICA (Proton Collisions).

Sources: LHC [30], HL-LHC [31], HE-LHC, FCC-hh [32] and NICA [33].

2.1 The Large Hadron Collider

2.1.1 Motivation

In December 1994 the European Organization for Nuclear Research (CERN) Council approved the LHC project to succeed the Large Electron-Positron Collider (LEP) after its shutdown in 1999 [34]. The LHC is designed to collide protons at an ultimate Centre of Mass (CoM) energy of 14 TeV making it the most energetic collider ever built.

This energy reach was motivated by various theoretical particle physics predictions and experimental sources, the most prominent being the Higgs boson, which was expected at an energy of about 115 GeV [35]. The Higgs boson is responsible for the mechanism resulting in particles having masses and was one of the last unsolved problems of the Standard Model (SM). It was also predicted that the results might shed light onto questions such as the origin of particle flavours or mechanisms explaining gravity and unifying forces. More exotic predictions hoped to see evidence of Beyond SM (BSM) theories. Another aim of the LHC was to understand the matter-antimatter asymmetry and the quark-gluon plasma making up hadrons.

The LHC has two high luminosity experiments, A Toroidal LHC ApparatuS (ATLAS) and Compact Muon Solenoid (CMS), in late 2012 both of these experiments announced the discovery of a 125 GeV Higgs like particle decaying to $\gamma\gamma$ and ZZ [36, 37]. Whilst these discoveries were made from beams colliding at a 7 and 8 TeV CoM, the beam energy and luminosity of the machine have since been increased resulting in a much larger data set; this has led to further discoveries such as the decay of the Higgs

boson to $b\bar{b}$ [38]. The LHC and its scheduled upgrades plan to constantly improve and provide data for the next two decades [31]. On top of this, the LHC-beauty (LHCb) experiment has provided insights into the CP symmetry violations and made it possible to accurately measure the decay rates of rare charm and beauty hadrons [39]. Moreover, the A Large Ion Collider Experiment (ALICE) experiment has provided insights into the equation of state of nuclei by measuring the outcome of ion-ion and ion-proton collisions in the LHC [40].

2.1.2 Layout

The LHC is housed in the same 27 km tunnel that was previously built and used for LEP. A schematic layout of the tunnel is shown in Figure 2.1, it is divided into eight octants, at the centre of each of these octants lies an IR labelled 1 to 8 [30, p. 37]. Each IR is quasi asymmetric around the IP, meaning that the β functions in one plane are equal to the β functions in the other plane on the other side of the IP. The IRs are connected through arcs that are labelled as Arcnp where n and p are the left and right adjacent IRs. For example, the arc between IR1 and IR2 is referred to as Arc12.

Each arc is constructed of 23 FODO cells containing six dipoles [30, p. 43-47] that are designed to reach up to 8.33 T [41]. The phase advance in each FODO cell is about 90° which is matched using quadrupoles that are powered in series in each arc. Sextupole magnets are found next to each arc quadrupole, these are arranged in two individually powered families and are used to correct the chromaticity of the ring [42].

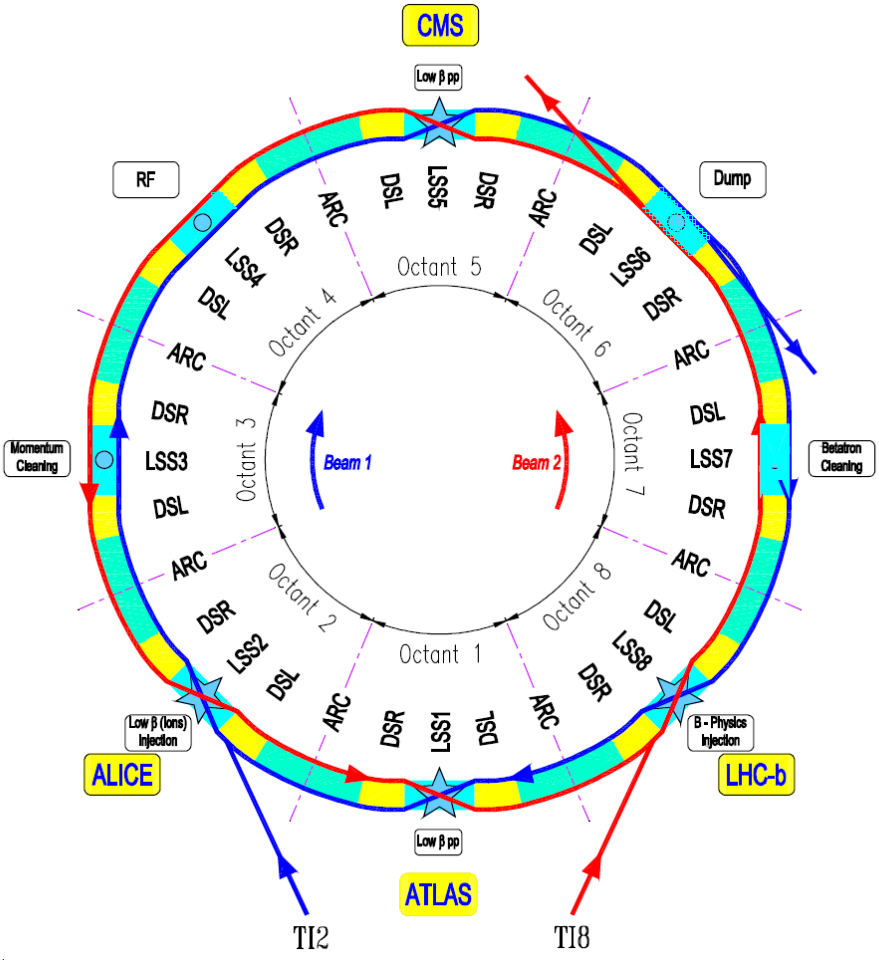

Figure 2.1: Conceptual layout of LHC Rings.

Source: [30, p. 37]

Beam 1 is injected in IR2 and circulates the LHC in a clockwise direction, whilst beam 2 is injected in the opposite direction in IR8. Both beams are injected at 450 GeV from CERN's Super Proton Synchrotron (SPS) with a design normalised emittance of 3.75 µm with bunches separated by 25 ns [43]. The beam is accelerated using the RF cavities in IR4, this IR also contains most of the beam instrumentation [30, p. 38]. IR4 was also designed in such a way that it contained one quadrupole more than needed to match the optics either side of the IP to give a handle to change

the tune of the LHC [44].

An extra quadrupole for tuning is also added in IR6, which contains the beam dump for both beams [45]. The beam is collimated in IR3 and IR7, the betatron cleaning takes place in IR7 whilst the momentum cleaning takes place in IR3. Both IRs use warm magnets to avoid the risk of superconducting magnet quenching [30, p. 36-38]. The beams cross each others' path in the four EIRs, two lower luminosity EIRs are in IR2 and IR8, whilst the higher luminosity EIRs, which are the most relevant in this thesis, are located in IR1 and IR5 [30, p. 32-36].

At injection the LHC is run at 59.28 and 64.31 horizontal and vertical tune respectively, once ramped up to full energy the optics are changed to collision optics and the tunes are set to 59.31 and 64.32 [46]. The LHC is designed to have a minimum BSC of 6.0 σ, however, it is run with a primary collimators set to 5.5 σ [47]. In its design the LHC aimed to have a long term DA of 6 σ, adding safety margins and uncertainties this translates to a computed DA of about 10 σ for 10^6 turns [48].

2.1.3 Experimental Interaction Region

As mentioned in Section 2.1.2, the LHC has four EIRs – this thesis focuses on the two high luminosity IRs, IR1 and IR5, hence a more detailed overview of these EIRs will be provided here.

The EIRs are designed to focus the beams down to a β^* of 55 cm in both planes and collide the beams at a crossing angle of 7σ, resulting in a minimum BSC of 6.98σ [30, p. 47-53]. This design β^* has since been surpassed by utilising improved collimation settings [47] and a special achromatic telescopic squeezing (ATS) optics [49].

The ATS optics works by decreasing the β^* by using the EIR magnets until the threshold at which the resulting chromaticity can still be compensated using the arc sextupoles. The β^* is then further decreased by increasing the β functions in the arcs adjacent to the EIR whilst leaving the EIR magnets unchanged. The increased arc β functions result in a higher efficiency of the sextupole correction as given by Equation 1.35 so that the chromaticity due to the lower β^* can still be compensated [42].

All these low β^* optics are achieved with a superconducting triplet located at an L^* of 23 m [50]. The triplet was optimised to be symmetric [51] with Q1 and Q3 being the same length and Q2 split into two sub-magnets Q2a and Q2b. Q1 and Q3 are 6.3 m long and the sub-magnets of Q2 are 5.5 m, the main quadrupoles are separated by 3.5 m leaving space for dipole kickers, collimators and beam position monitors (BPMs). The two Q2 magnets are 1 m apart and with a dipole kicker in between [52]. All three magnets have a field of 205 Tm^{-1} at collision and are powered in series but can be shunted individually using dedicated trim converters [53].

A skew quadrupole as well as two non-linear corrector magnets are located adjacent to Q3 in order to compensate for coupling and reduce the orbit distorting terms. The non-linear correctors can produce sextupole, octupole and dodecapole fields as well as skew sextupole and octupole fields. These can be used to compensate for errors in the triplet but also the dipole magnets [13].

The separation is achieved using a normal conducting D1 made of six 3.4 m long normal conducting magnets with a field of up to 1.38 T and a superconducting twin aperture D2 that is 9.45 m long and can produce a field of 3.5 T [52]. The LHC does not use any crab cavities since the crossing angle is relatively low [54].

The matching section of the LHC is made of three individually powered superconducting quadrupoles Q4, Q5 and Q6 – for historical reasons these three magnets are sometimes referred to as the outer triplet [55]. The DS is highly constrained by LEP tunnel geometry and made of two arc cells that have two instead of the regular three dipoles per half cell, the quadrupoles in these cells, Q7-Q10 are powered individually. In order to help the matching to the arc, the trim quadrupoles in the first arc cell, QT11-QT13, are also used to for the matching. These are adjacent to the FODO quadrupoles Q11-Q13 and are individually powered.

The injection optics of the LHC are designed to have a β^* of 10 m which results in much lower β functions in the triplet which is a requirement at injection since the emittance is larger. When the energy increases the β^* is squeezed to collision optics by gradually changing the quadrupole strengths. An overview of the injection and collision optics is shown in Figure 2.2 and Figure 2.3 respectively.

2.2 Future Colliders

The discovery of the Higgs boson was a great success for the SM and the accelerator community but the LHC experiments have not yet shed light on all questions it set out to answer. Currently, there are several options for possible colliders to explore fundamental particle physics in the post-LHC era. In general the options vary between various hadron synchrotrons that reach higher luminosities and energies, high-luminosity lepton synchrotrons and high energy lepton linear accelerators (linacs) for precision measurements as well as ion-lepton and hadron-lepton colliders for nuclear measurements.

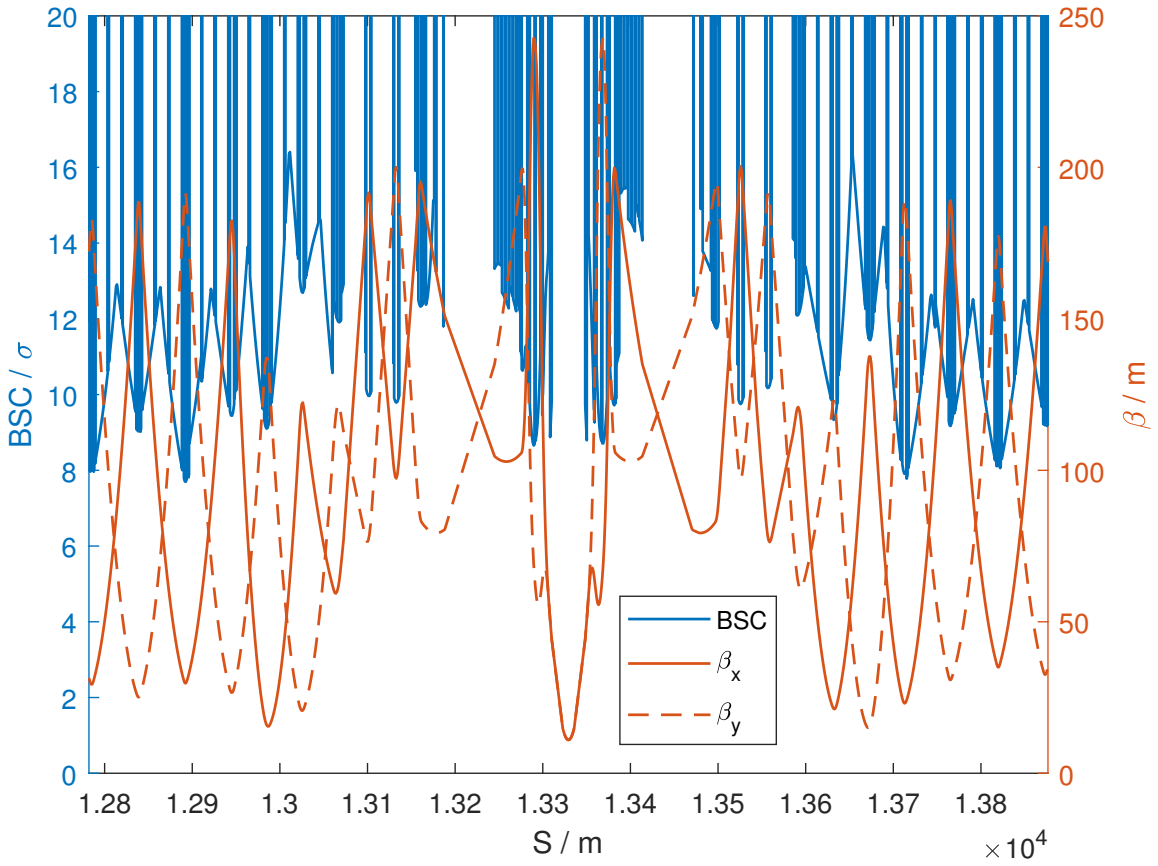

Figure 2.2: Plot showing β functions and BSC in LHC EIR for $\beta^* = 10$ m injection optics at 450 GeV beam energy.

This section will give an overview of some of these machines before going into greater detail on the three machines that will be explored in the scope of this thesis, namely the High Energy LHC, the Future Circular hadron-hadron Collider and the Nuclotron-based Ion Collider fAcility.

2.2.1 Future Collider Options

The High-Luminosity LHC (HL-LHC) is an approved upgrade of the LHC that aims to increase the LHC luminosity by upgrading the LHC injectors [56] to provide more intense beams during the LHC's long shut down at the end of 2018 [57] and installing an upgraded EIR in the long shut down at the end of 2024 [31]. These upgrades aim

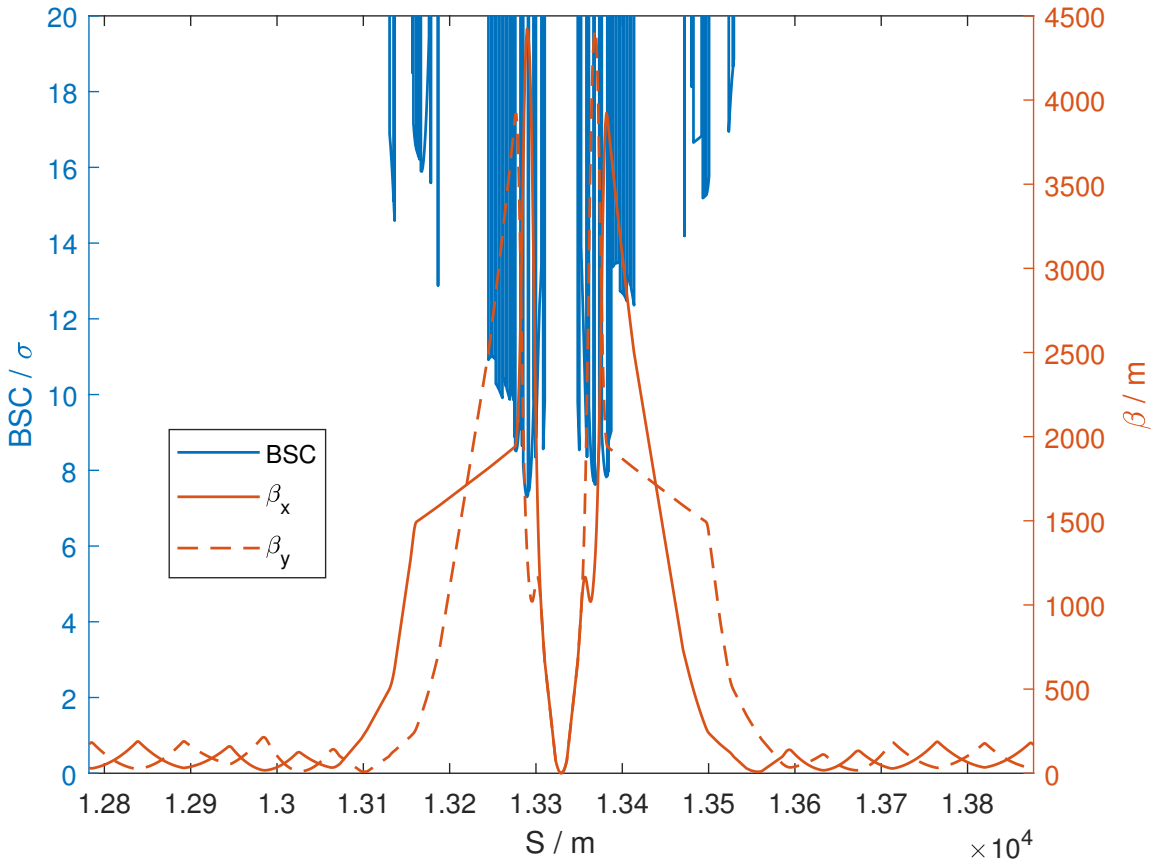

Figure 2.3: Plot showing β functions and BSC in LHC EIR for $\beta^* = 0.55$ m collision optics at 7 TeV beam energy.

to increase the luminosity by a factor of ten to fifteen, thus greatly increasing the amount of data that can be explored. The upgrade is made possible with magnets produced using a novel Nb_3Sn superconducting technology to manufacture a new triplet with higher gradients and aperture as well as new 11 T dipoles to be installed in various location to provide more space for collimators [58].

A more extensive upgrade of the LHC is considered in the High-Energy LHC (HE-LHC) upgrade, which explores the option of replacing all arc dipole magnets in the LHC with 16 T Nb_3Sn dipoles [59]. This increased strength would allow protons to be accelerated to CoM energies up to 27 TeV to explore new energy scales. With the

same technology it is possible to reach even higher energies by increasing the radius of the synchrotron. This is considered in the Future Circular Collider (FCC) study, that looks into a hadron collider, FCC-hh, that uses 16 T magnets in a 100 km ring in order to reach CoM energies of 100 TeV [60].

Whilst hadron synchrotrons are limited by the highest magnetic fields they can achieve, the energy reach and beam intensity of electron synchrotrons are limited by the synchrotron radiation produced by the beam and the power the RF-Cavities can provide the beam to counter this effect. This is because the energy a particle loses per turn due to synchrotron radiation is proportional to $\left(\frac{E}{m}\right)^4$, where E and m are the energy and rest mass of the particle [6, p. 45], which is about 2000 times lower for electrons than for protons. This results in electron synchrotrons being a lot less energetic than proton accelerators of the same size. However, since protons are composite particles, the actual CoM energy achieved in a collision depends on the parton distribution in the colliding protons and is typically significantly lower than the total CoM energy of the protons. Electrons are elementary particles so that the CoM energy in each collision is always equal to the CoM energy of the electrons, therefore electron colliders are sometimes favourable as they can be used for precision measurements at specific energies.

The FCC study also looks into a electron-positron collider that could precede the FCC-hh in the same 100 km as was the case with LEP and LHC. The FCC-ee plans to initially collide leptons at CoM energies of 91.2 GeV with peak luminosities of $200 \times 10^{34}\text{cm}^{-2}\text{s}^{-1}$ and eventually reach energies of up to 365 GeV at the cost of reducing the beam current and consequently the luminosity to $1.3 \times 10^{34}\text{cm}^{-2}\text{s}^{-1}$ [32].

A similar study is also performed in the Chinese Circular Electron-Positron Collider (CEPC) study that plans to house a lepton collider in a 70 km with plans to also install the Super Proton-Proton Collider (SPPC) in the same tunnel [61].

Lepton linacs have the advantage that they do not require to bend the particles, meaning there is no synchrotron radiation. As a result of this linacs can potentially reach much higher energies, however, since the particles are lost after each collision, it is a lot more challenging to achieve high luminosities. Both the Compact Linear Collider (CLIC) [62] and the International Linear Collider (ILC) [63] study possible electron linear colliders. The ILC aims to collide electron and positron beams at CoM energies between 250 GeV and 1000 GeV and reach luminosities of up to $5 \times 10^{34}\text{cm}^{-2}\text{s}^{-1}$ [63, p. 11]. Similarly, CLIC aims to collide beams at CoM energies between 350 GeV and 3 TeV with a peak luminosity of 6×10^{34} $\text{cm}^{-2}\text{s}^{-1}$ [62, p. 15]. The properties of the accelerators above are summarised in the Figure 2.4 which also aims to illustrate some of the benefits and drawbacks of all three types of collider.

Other future colliders include ion colliders such as the approved Nuclotron-based Ion Collider fAcility (NICA) in Russia [64] and Facility for Antiproton and Ion Research (FAIR) in Germany [65]. Another option are ion-electron colliders, two possible such colliders are currently being considered in the US JLab Electron-Ion Collider (JEIC) [66] and the electron upgrade of the Relativistic Heavy Ion Collider (eRHIC) [67]. Electrons and hadron collisions are also considered in the Large Hadron Electron Collider (LHeC), which proposes to collide LHC hadrons with electrons accelerated in a dedicated energy recovery linear accelerator [68]. Both these types of accelerators can help gain a deeper insight into the structure and spins in atomic

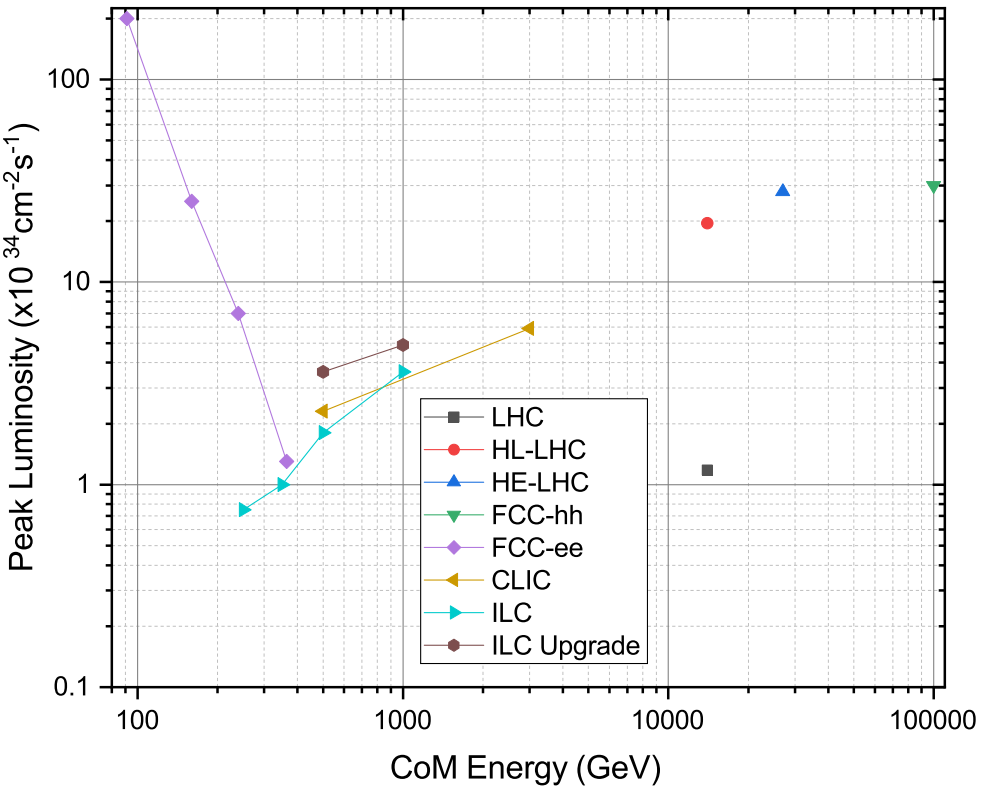

Figure 2.4: Plot showing peak luminosity and CoM energy for various colliders. Sources: LHC [30], HL-LHC [31], HE-LHC, FCC-hh, FCC-ee [32], CLIC [62, p. 15] and ILC [63, p. 12]

nuclei.

Another approach involves moving away from classical accelerator technologies and using alternative accelerating techniques such as plasma acceleration, an example of this technology was recently demonstrated in the Advanced Wakefield Experiment (AWAKE) [69].

2.2.2 High Energy Large Hadron Collider

As mentioned in Section 2.2.1, the HE-LHC plans to benefit from the (HL-)LHC's Injector Upgrade (LIU) to have a high intensity-beam but collide these at much higher

energies by using Nb_3Sn magnet technology. Since the HE-LHC would be built in the same tunnel as the LHC, the LHC's eight sector layout is adapted, broadly assigning the same functions to the individual IRs as in the LHC and shown in Figure 2.1. When optimising the individual IRs, the DS or the arc cells one is greatly constrained by the the tunnel geometry [70].

Replacing all the arc dipoles in the LHC with 16 T magnets would result in a CoM energy of 26 TeV. However, the HE-LHC aims to ideally reach a CoM energy of 27 TeV by increasing the dipole fill factor in the arcs. It aims to increase this fill factor by optimising the cell layout and by decreasing the number of cells per arc while increasing the number of dipoles in each cell. Currently, there are two arc options: a more conservative optimised LHC-like layout with 23 cells per arc and a more challenging 18-cell layout that adds an extra dipole per half cell [71, p. 45-55].

Whilst the 18-cell lattice has a large enough fill factor to reach the 27 TeV, the fact that the quadrupoles are further apart means that the β functions in the arc cells are larger, potentially causing problems at the 450 GeV injection energy. This could be solved by upgrading the SPS injector using single or double layer superconducting magnets to achieve injection energies of 900 GeV or 1300 GeV respectively [72]. Apart from the aperture one has to take great care that the geometry of these new arcs does not deviate from the geometry of the LEP tunnel by more than a few centimetres. Moreover, the DA of the machine with these new arcs and magnets has to be studied carefully at the various injection energies [73].

The main challenging factor for the EIR is that its length is greatly constrained as it was originally optimised for LEP. The experimental cavern is not planned to change

meaning that the LHC's L^* of 23 m is conserved. In order to reach the desired peak luminosity of $28 \times 10^{32}\text{cm}^{-2}\text{s}^{-1}$, the EIR needs to focus the beam to a β^* of 0.45 m in both planes. The increased beam rigidity means that this requires a new triplet.

The new triplet has to be as short as possible in order to keep the chromaticity low and to minimise the amount of space it takes up. At the same time it needs enough aperture to support a minimum BSC of 12σ instead of LHC's 6 σ since the increased beam energy puts strong limits on the collimation [74]. Moreover, the aperture also has to leave enough space for shielding to protect the triplet from the collision debris.

The separation dipoles have to be chosen so that they are strong enough to steer the more rigid beams, have space for shielding and ideally compensate for the extra space taken by the triplet. Due to the collimation limits, the beam also needs a large crossing angle of 16.85 σ making crab cavities very favourable. The design has to leave enough space for crab cavities between the D2 and the matching section, which has to be adapted to the more rigid beam, whilst not exceeding quadrupole strengths of 360 Tm^{-1}.

The DS has to be optimised to be compatible with the increased β functions and dispersion in the arc cells as well as the large beam rigidity, whilst not deviating from the LEP geometry by more than a few centimetres. On top of this it is very important to have a phase advance of $[\frac{\pi}{2}]$ from the IP to the focusing first sextupole in each plane. This can help correct for spurious dispersion caused by the crossing angle and will help the efficiency of the chromaticity correction for possible ATS optics [75].

2.2.3 Future Circular Collider

Unlike the HE-LHC, the FCC-hh would be constructed in a purpose built tunnel, the conceptual layout of this tunnel is show in Figure 2.5. Like the LHC, there are eight IRs with similar functions but labelled alphabetically. Six of these IRs are 1.4 km long, whilst the β collimation and the extraction IRs are 2.8 km long. The FCC-hh plans to have four 16 km long arcs and four shorter arcs, only 3.4 km in length [76].

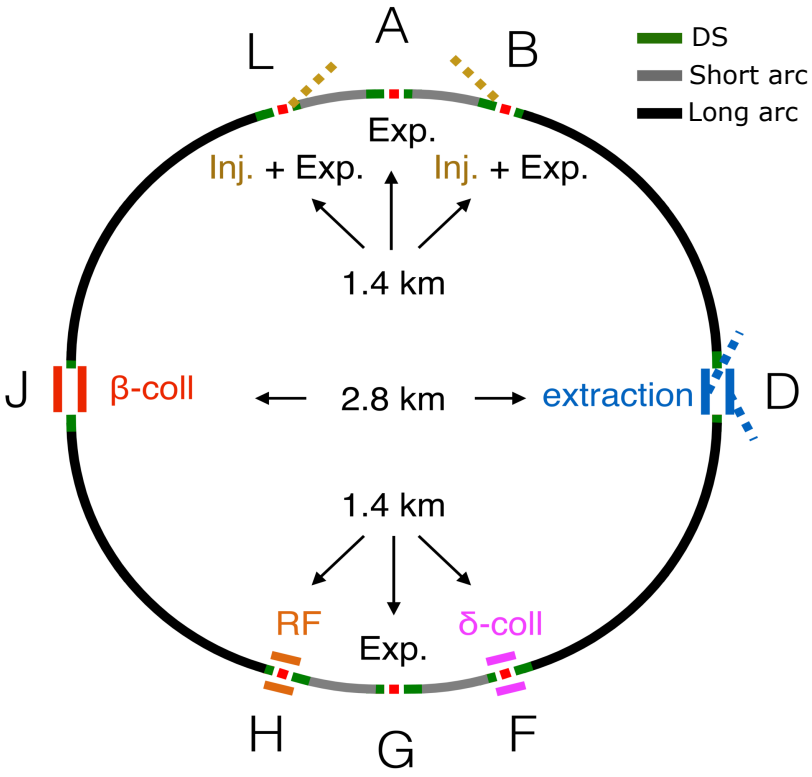

Figure 2.5: Conceptual layout of the FCC-hh.

Source: [77]

Each FCC-hh arc cell contains twelve 16 T dipoles, arc cells of this length are possible because FCC-hh plans to inject protons at 1.3 TeV from an upgraded SPS or 3.3 TeV protons from an re-optimised LHC [78]. The DS is similar to that of the LHC and is made of two cells containing eight dipoles each [79]. At top energy the FCC-hh

beam stores 8.5 GJ of energy making collimation very challenging, the acceptance is projected to be at 15.5σ [80].

The detectors in the two high luminosity EIR (A and G) are planned to consist of a main solenoid, two forward solenoids as well as two muon chambers at the end caps [81]. This setup is projected to span 24 m either side of the IP, additional space has to be budgeted to allow the detector to be opened and to leave space for a Triplet Active Shielding (TAS) absorber, initially leading to an L^* of 45 m, which was later reduced to 40 m.

The FCC-hh aims to achieve a peak luminosity of $30 \times 10^{34}\text{cm}^{-2}\text{s}^{-1}$ and plans to do this by focusing the beam down to a β^* of 0.3 m in both planes and by using crab cavities to compensate for the 12σ crossing angle.

In a first approximation the the FCC-hh triplet was constructed by scaling the LHC triplet by a factor of $\sqrt{\frac{50\text{TeV}}{7\text{Tev}}} \approx 2.67$ [82]. This triplet was then further optimised to leave the right L^* and provide the right amount of shielding to keep the integrated lifetime radiation dose between 30 and 100 MGy, depending on the nature of the superconducting coils [83]. One of the goals of this thesis is to come up with an alternative triplet design using a more systematic approach.

Apart from the the triplet, the rest of this alternative EIR is based on the baseline EIR [82]. Initially superconducting separation dipoles were considered, however, it was decided to use normal-conducting dipoles instead since these do not quench and the purpose built tunnel provides enough space. Like the LHC, the matching section is made of three individually powered quadrupoles. The rest of the IR is made of the DS and the first arc cell, whose quadrupoles can be individually powered.

2.2.4 NICA

Unlike the HE-LHC and FCC-hh, the NICA collider is already approved by the Joint Institute for Nuclear Research (JINR) in Dubna, Russia, with the construction and commissioning of an upgraded injector linac LU-20 being under way [84] and the arc dipole magnets being produced and tested [85].

By colliding ions, polarised protons and deuterons, the NICA facility aims to probe the in-medium properties of hadrons and the equation of state of nuclear matter. The high polarisation aims to give insights into the spin structure. The NICA project aims to measure collisions in two experiments; the first IP will have the Multi Purpose Detector (MPD) concentrating on heavy ion collisions, whilst the second one will have the Spin Physics Detector (SPD) concentrating on spin physics [64].

The NICA collider aims to use 1.8 T superconducting dipoles to circulate 22 bunches in a 500 m ring. This will allow it to collide protons at CoM energy of 27 GeV and heavy ions such as gold to energies up to 11 GeV/u. The predicted luminosities are $10^{32}\text{cm}^{-2}\text{s}^{-1}$ and $10^{27}\text{cm}^{-2}\text{s}^{-1}$ for protons and ions, respectively[86].

These luminosities are obtained by focusing the beam to β^* of 0.6 m using a superconducting triplet located 5.25 m from the IP. Since this L^* and the triplet are relatively short, the beams can be collided without a crossing angle with very low long range beam-beam effects after they have been separated again.

After passing through the triplet the beam is matched using six trim quadrupoles, one of which is located after the triplet and before D1, the other five located between D2 and the arc. The dispersion is suppressed using a missing dipole scheme made

of two FODO cells without any dipoles. An overview of the Twiss functions of the entire ring is shown in Figure 2.6.

Whilst the design of the machine is almost complete and the arc dipoles and quadrupoles are in production, one challenge faced by the NICA collaboration is a large reduction in the DA when tracking is performed with fringe triplet quadrupole fringe fields turned on. These fields occur due to an intrinsic effect of the finite length of the quadrupoles and exert an octupole-like kick on the particles in the beam [87].

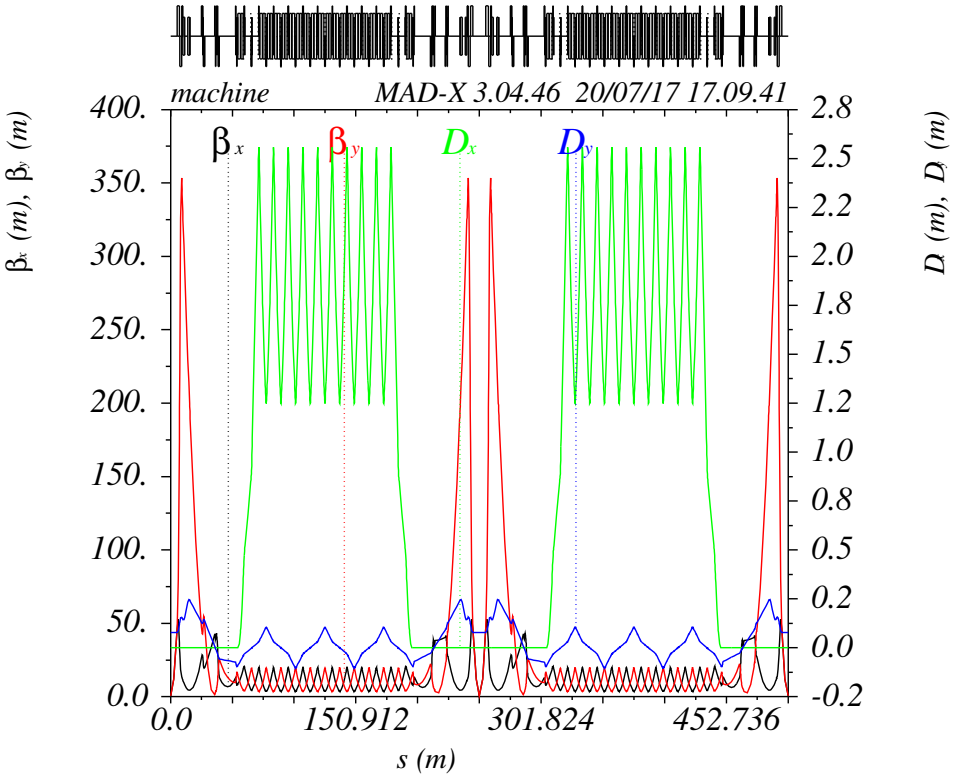

Figure 2.6: Plot showing β functions and dispersion around NICA Collider.

Chapter 3

Triplet Optimisation Code

3.1 Motivation

As outlined in Chapters 1 and 2, a fully optimised triplet is essential for a well designed EIR. Especially in synchrotrons, a short triplet can help save space, keep the chromaticity low, improve the DA and save costs. The large β functions in the triplet put lower limits on the aperture and in turn upper limits on the quadrupole gradients, forcing the triplet to be long in order to have the required integrated field.

In future colliders, this is amplified by the fact that the unprecedented amounts of collision debris require quadrupole apertures to be large enough to leave room for shielding. Moreover, the large beam rigidity calls for very high gradients. In order to tackle this challenge one of the main aims of the work in this thesis is to come up with a way to systematically find the shortest possible triplet that satisfies all the other design constraints. This is achieved with a Triplet Optimisation Code that scans through the triplet design parameter space to find the optimum solution.

3.2 Thin Lens Solution

3.2.1 Introduction

The properties of a triplet can only be fully described when the strength of each magnet has been matched using a numerical algorithm, such as MADX, and the beam size along the entire triplet has been calculated in order to work out the BSC of the triplet. Both these processes can be very computationally intensive and it would take several hours to scan through the whole parameter space. Furthermore, the solution found by the matching algorithms often depends on the initial conditions used.

To tackle both these issues, it is possible to approximate the triplet as a system of thin lenses. Whilst not being as accurate as finite element tracking, thin lens systems have the benefit that they can be solved analytically and require no numerical matching. This means that they can be used to perform a very fast scan through parameter space and provide a good guess for the initial conditions of a realistic system with finite length quadrupoles. Moreover, the strengths of the thin lenses can be used as an estimate of the apertures of the magnets they represent.

The idea of approximating the final focus using thin lenses has been used before, for example in the design of the final focus section in the CLIC [88]. In this process the final focus section is expressed as a block of elements with the overall transfer matrix

$$\mathbf{M_z} = \begin{pmatrix} -1/æ_z & 0 \\ 0 & -æ_z \end{pmatrix}, \tag{3.1}$$

where $æ_z$ are the de-magnifying factor in the x or y plane.

This system has eight constraints and was solved using eight variables in the form of four unique thin lenses and four unique drifts — meaning that this system requires one quadrupole more than is available in the triplet. In [89], the number of constraints was reduced to six by realising that $\det \mathbf{M_z} = 1$ can be used to eliminate one constraint per plane, showing that an arbitrary transfer matrix can be constructed out of three lenses and three drifts. Whilst this bears closer resemblance to a triplet solution, there is no freedom to vary any of the design parameters as desired.

For completeness, it should also be pointed out that a mathematically more rigorous process is presented in [90], which shows a focusing system as described in Equation 3.1 that can be achieved with four lenses and five drifts. This solution introduces a scaling factor, λ, by which drifts can be multiplied and focal strengths can be divided, to make the solution more applicable to real life situations, however, again this requires one quadrupole more than in a triplet.

3.2.2 Problem Formulation and Parameterisation

The novelty of the thin lens solution presented in this thesis is that it does not aim to solve for the entire transfer matrix and therefore leaves a lot more free variables that can be used to constrain the triplet layout and length but also vary design parameters to optimise the layout. In a first step it does this by approximating the triplet as three thin lenses lying at the centres of quadrupoles Q1, Q2 and Q3 as shown in Figure 3.1. The focal strength of a thin lens, g, is equal to the normalised field strength, k, times the length of the quadrupoles it represents, L_Q. The lenses in the configuration have

focal strengths g_1, g_2 and g_3 respectively. The distance from the IP to the first lens is l_1, the distances between the first and second lenses and the second and third lenses are l_2 and l_3 respectively and results in six variables.

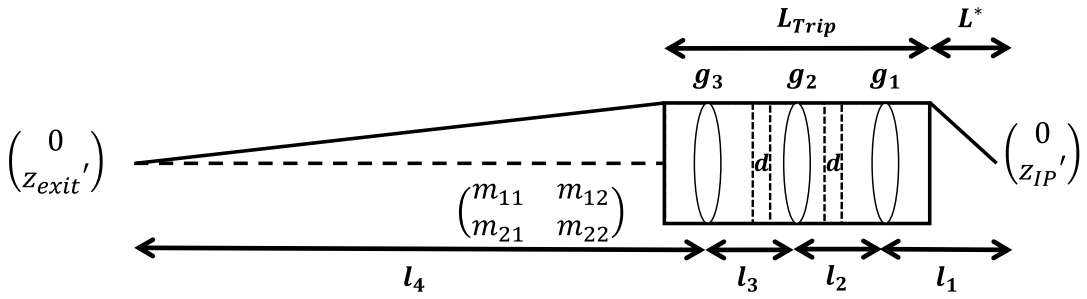

Figure 3.1: Layout of thin lens system as approximation of triplet.

The model also includes a fourth drift with an arbitrary large length l_4. The simplification then arises from the realisation that the key property of a final focus triplet is that it focuses a particle originating from a far away point at $z = 0$ and an arbitrary $z' = z'_{exit}$ to $z = 0$ at the IP, again with an arbitrary $z' = z'_{IP}$. This can be expressed mathematically as

$$\begin{pmatrix} 0 \\ z'_{exit} \end{pmatrix} = \begin{pmatrix} m_{11} & m_{12} \\ m_{21} & m_{22} \end{pmatrix} \begin{pmatrix} 0 \\ z'_{IP} \end{pmatrix} = \begin{pmatrix} m_{12} \times z'_{IP} \\ m_{22} \times z'_{IP} \end{pmatrix}. \tag{3.2}$$

From Equation 3.2, it can be seen that this condition is met if $m_{12} = 0$ in both planes – ultimately leading to two constraints. An expression for m_{12} in terms of l and g can be found using simple matrix multiplication of the drift and thin lens transfer matrices given by Equation 1.20. A further constraint is obtained from demanding that the total length of the triplet is equal to L_{Trip}. In order to parameterise this we need to find expressions for finite lengths of the quadrupoles, L_Q, the thin lenses are representing. Since the thin lens is located at the centre of each quadrupole, the half

length of Q1 is $l_1 - L^*$, hence

$$L_{Q1} = 2 \times (l_1 - L^*). \tag{3.3}$$

The half length of Q2 is l_2 minus half of the space taken up by Q1, $L_{Q1}/2$ and the separation between the quadrupoles, d. The full length is therefore

$$L_{Q2} = 2 \times (l_2 - d - \frac{L_{Q1}}{2}) = 2 \times (l_2 - d - l_1 + L^*). \tag{3.4}$$

Similarly for Q3

$$L_{Q3} = 2 \times (l_3 - d - \frac{L_{Q2}}{2}) = 2 \times (l_3 - l_2 + l_1 - L^*). \tag{3.5}$$

The overall length of the triplet is given as

$$L_{Trip} = L_{Q1} + d + L_{Q2} + d + L_{Q3} = 2 \times (l_3 + l_1 - L^*). \tag{3.6}$$

Fixing this length puts a constraint on l_3 in terms of l_1, leaving three free variables. Using this l_3 is set to

$$l_3 = \frac{L_{Trip}}{2} + L^* - l_1. \tag{3.7}$$

It was decided to add another length constraint to reduce the number of free variables further. This constraint was chosen to set the lengths L_{Q1} and L_{Q3} to be the same. This constraint is found in many colliders, such as the LHC [51], and reduces the number of different types of magnets that need to be designed and produced. This leads to

$$L_{Q1} = L_{Q3} \rightarrow 2 \times (l_1 - L^*) = 2 \times (l_3 - l_2 + l_1 - L^*) \rightarrow l_2 = l_3. \tag{3.8}$$

Furthermore, the equations for L_{Qi} can be simplified in terms of l_1 to be

$$l_{Q1} = l_{Q3} = 2 \times (l_1 - L^*), \tag{3.9}$$

$$l_{Q2} = L_{Trip} - 2 \times d - 4 \times (l_1 - L^*). \tag{3.10}$$

These relations also define the upper and lower limit of the domain of l_1 since we require $L_{Qi} > 0$.

Apart from l_1, this leaves one more free variable; this variable was chosen to be the strength of the first quadrupole, g_1. The overall transfer matrix in terms of l_i and g_i was worked out using Wolfram Mathematica [91], which was then also used to solve the set of equations yielding expressions for g_2 and g_3 in terms of g_1, l_1 as well as l_4 and the other drift lengths, which are constrained by l_1. The solutions for these two strengths are

$$g_2 = \frac{g_1 l_3 l_1^2 (l_3 + l_4) + c}{b l_3 (l_3 + l_4)}, \tag{3.11}$$

$$g_3 = \frac{-c}{l_4 l_3 (b + a l_3)}, \tag{3.12}$$

where

$$c \equiv \sqrt{l_3 (b + a l_3)(l_3 + l_4)(b + a(l_3 + l_4))} \tag{3.13}$$

and

$$a \equiv -l_1 (l_1 l_2 g_1^2 + 1), \tag{3.14}$$

$$b \equiv -l_1 (l_1 + 2 l_2 + l_2^2 g_1^2 l_1). \tag{3.15}$$

In order to find an appropriate choice of l_4 a brief study was performed that aimed to find out at which value of l_4 the solutions converge. To this end a system was set

up with $l_1 = 50$ m, $l_2 = l_3 = 10$ m and $g_1 = 0.5$ m^{-1} and the solutions to g_2 and g_3 were found using this solution whilst varying l_4 from 500 m to 4000 m. The results are shown in Figure 3.2.

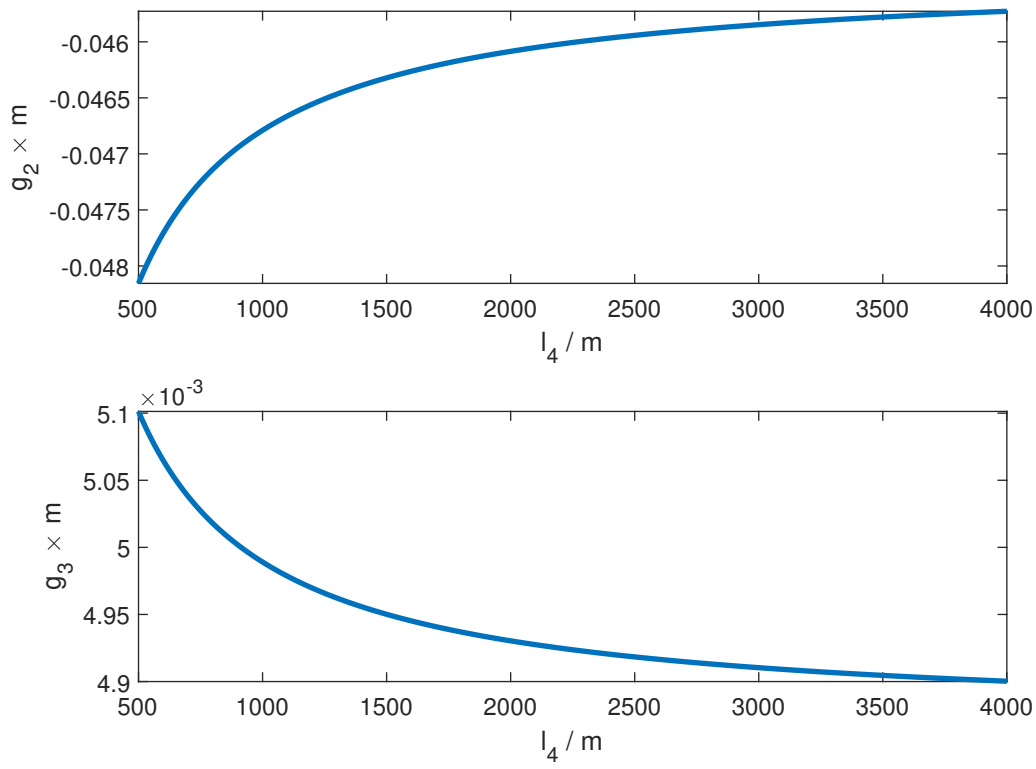

Figure 3.2: g_2 and g_3 found using the thin lens solution for various l_4 values.

From Figure 3.2 one can see that the solutions follow an asymptotic behaviour with respect to l_4. One can also see that at $l_4 = 1000$ m the solution seems to already be within about 2 % of the asymptote. Therefore, an $l_4 = 1000$ m was used in this thesis.

3.2.3 Tracking and Aperture

The thin lens solution can also be used for a first estimate of the BSC of the solution that it found. The first step required in doing this is to obtain an estimate of the

beam size in each quadrupole. This can be done by tracking the position of a 1 σ particle through the system using matrix multiplication. From Equation 1.39, a 1 σ particle has $z'_{IP} = \sqrt{\epsilon_z/\beta_z}$, this particle can be traced in both planes to work out x and y in every thin lens.

An example of various tracked particles is shown in Figure 3.3, which is produced with a triplet in the same configuration as used for Figure 3.2 but l_4 is set to 100 m for the purpose of visualisation. The plot shows the x and y co-ordinates for a tracked particle with $x'_{IP} = y'_{IP} = 1$ and a range of initial g_1.

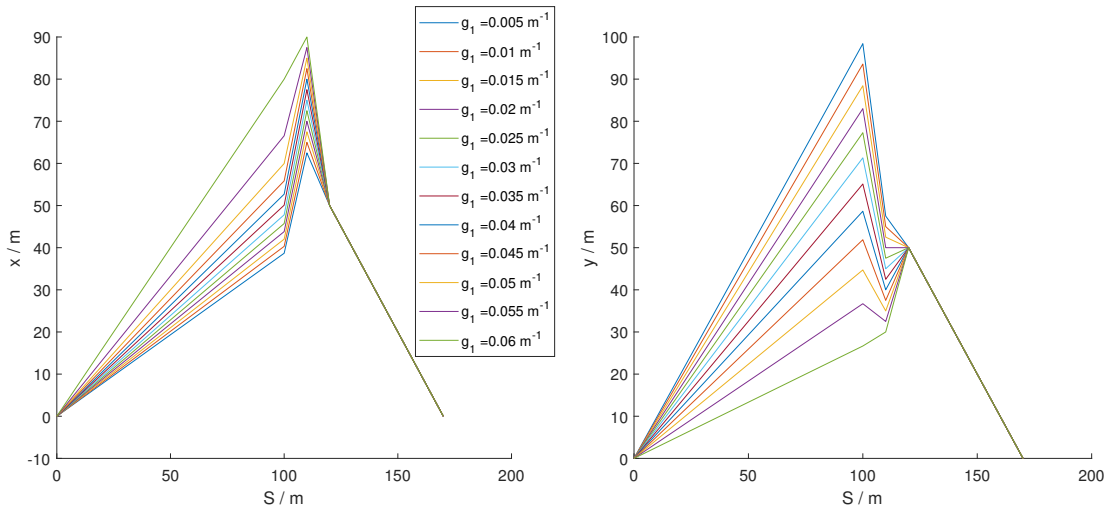

Figure 3.3: Plots showing examples of tracked particles in the horizontal and vertical planes for various solutions.

Next, the aperture of each quadrupole has to be evaluated. In order to do this the algorithm calculates the length of each quadrupole using Equations 3.3, 3.4 and 3.5 and then works out the normalised field strength $k_i = g_i/L_{Qi}$. Using Equation 1.6, the absolute magnetic gradient can be worked out to be $G_i = k_i \times (B\rho)$. This can be substituted into the approximation used in Equation 1.10 to give an estimate for the aperture radius as

$$r_i \approx \frac{B_{MAX}}{G_i} = \frac{B_{MAX}}{k_i \times (B\rho)} = \frac{B_{MAX} L_{Qi}}{g_i \times (B\rho)}. \tag{3.16}$$

Together with the tracked 1σ orbits, z_i, this can be used to obtain an estimate for the BSC to be

$$N = \frac{r_i}{\max(x_i, y_i)} = \frac{B_{MAX} L_{Qi}}{\max(x_i, y_i) \times g_i \times (B\rho)}. \tag{3.17}$$

Since B_{MAX} and $B\rho$ are simply constants that depend on the available technology and the machine specifications, these can be set to one to get a machine independent general figure of merit (FOM) that is proportional to the lowest BSC. This FOM is equal to

$$FOM = \min\left(\frac{L_{Qi}}{\max(x_i, y_i) \times g_i}\right). \tag{3.18}$$

Since all machine-dependent constants were dropped for this FOM, it is no longer necessary to track a 1σ particle and a particle with $z' = 1$ can be tracked instead.

This FOM can be used to get an estimate of the BSC of triplets over a large parameter space using a programming language such as Python [92]. Because this FOM can be worked out using a relatively small amount of simple mathematical operations a high resolution scan can be computed almost instantaneously. An example of such a scan is shown in Figure 3.4, which was performed using an FCC-hh like layout with $L^* = 45$m, $L_{Trip} = 140$m and $d = 12.5$m.

3.3 Finite Element Aperture

3.3.1 Conversion and Matching

The thin lens solutions provides a good estimate for the quadrupole strengths required to focus the beam for a given quadrupole configuration. Moreover, the FOM can be

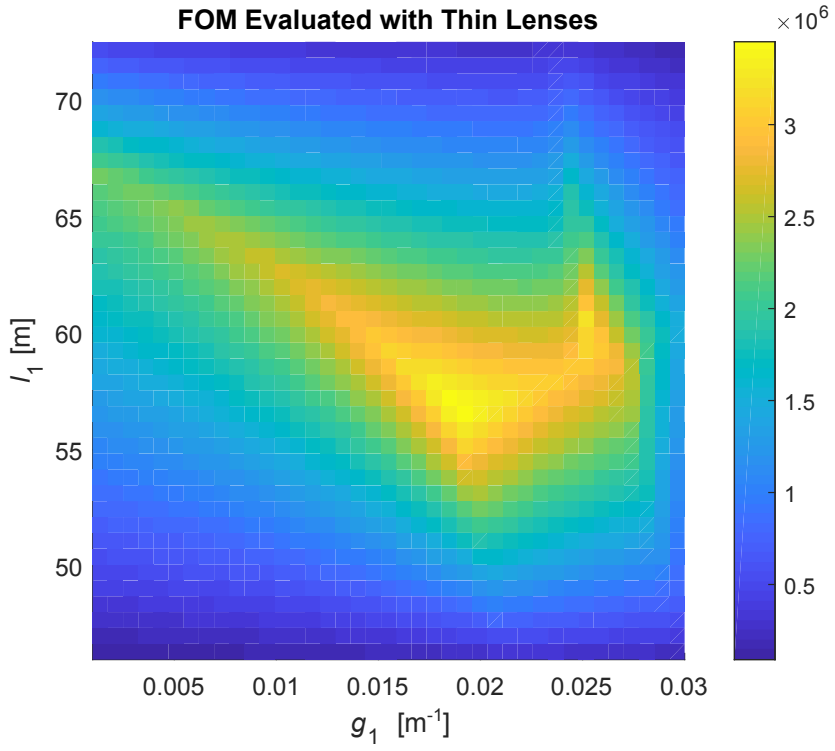

Figure 3.4: Example of a FOM scan produced using the thin lens solution.

used to get an estimate of the BSC. To get the accurate BSC, however, one has to consider a system of finite length quadrupoles, accurately matched and with the BSC calculated along every quadrupole.

To do this the algorithm has to take the solutions produced by the thin lens code and convert them to a sequence of finite length quadrupoles that can be read into MADX [8]. This conversion is done using the pymadx [93] library that can be used to generate a MADX sequence file with a triplet out of quadrupoles with lengths L_{Qi} as in Equations 3.9 and 3.10 above, and strength $k_i = g_i/L$. The sequence is then called by a MADX mother file that can also set the properties of the beam and the Twiss functions at the IP and compute the Twiss functions through the triplet. An example of the results of this conversion is shown in Figure 3.5a, where the β^* is set

to 1.1 and L^* is 45 m like initially considered for the FCC-hh. The thin lens solution gives the highest FOM for a configuration with a triplet that has a length of 54 m and the quadrupoles 3 m apart, as mentioned above, l_4 of 1000 m is used.

As one can see from Figure 3.5a, the solution does not result in the β functions going down to zero at the end of l_4. This shows the limitations of the thin lens approximation when converting to very long finite length quadrupoles.

The MADX matching module can be used to fine tune the strengths of Q2 and Q3 for finite length quadrupoles. This can be done using the built-in LMDIF matching algorithm to match β_x and β_y to zero at the exit by varying the strengths of Q2 and Q3. The LMDIF is the fastest matching method in MADX and uses the gradients of the parameters being matched to minimise the sum of their squares [8, p. 146]. This method is sufficient for this simple matching of two constraints using two variables. This can be applied to the solution shown in Figure 3.5a to obtain an optics as shown in Figure 3.5b.

To explore how much the quadrupole strength is changed by this matching, a script was written that varies g_1 and stores the thin lens solutions for g_2 and g_3 for the layout above. It then performs the matching and stores the matched quadrupole strengths. The results are shown in Figure 3.6, from which one can see that whilst there is a systematic offset between the thin lens and matched strengths they follow the same trend, indicating that the thin lens is a good approximation. The matched values are larger than the thin lens values, which is what one would expect since the finite length of the quadrupoles means that the β functions in the quadrupoles in the focusing plane are smaller than in the thin lens.

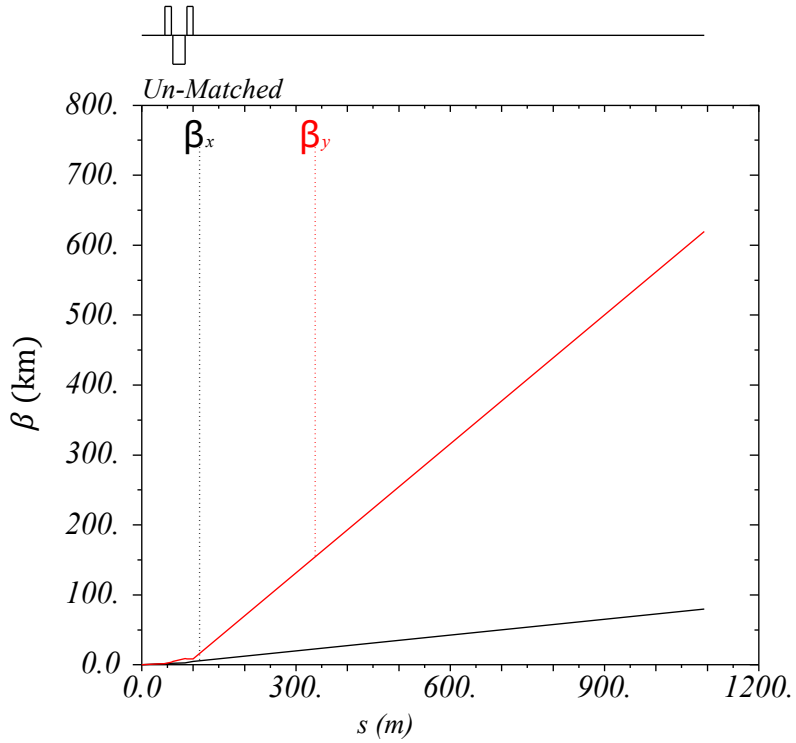

(a) Un-matched

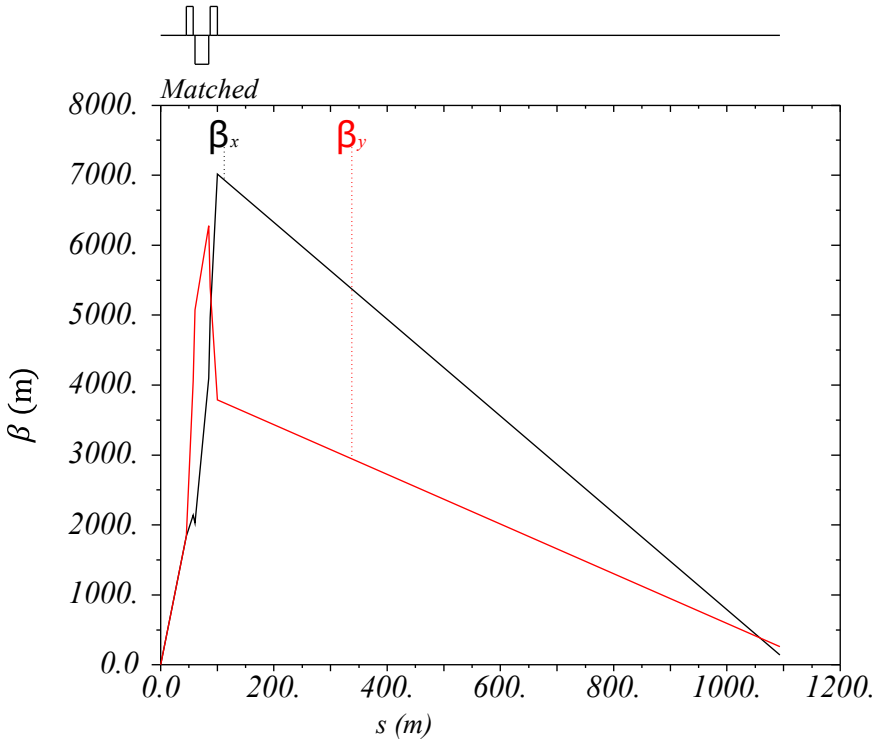

(b) Matched

Figure 3.5: Example of MADX Twiss output for a converted finite triplet.

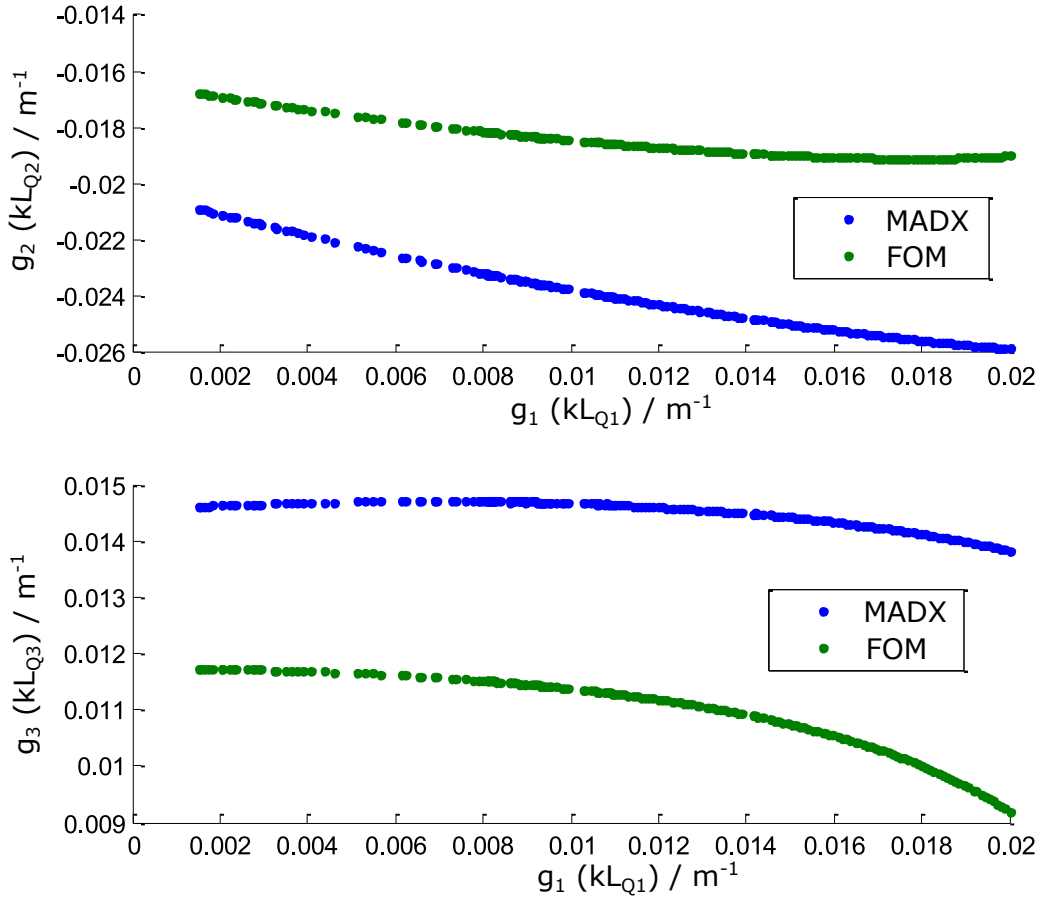

Figure 3.6: Comparison between thin lens strength, g, and matched integrated strength, kL_{Qi}.

3.3.2 Aperture Module

To evaluate the actual BSC of the matched triplet, the MADX aperture module has to be used [8, p. 153-164]. This slices each magnet into smaller segments. The β functions can then be worked out at each of these segments using matrix multiplication, rather than just evaluating it at the entrance and exit of the quadrupole. The 2D beam size can then be evaluated from the β functions and the emittance, that can be specified by the user in the algorithm, to work out the BSC at every point using Equation 1.40.

To do this MADX also has to calculate the beam pipe aperture in each quadrupole. In the first step of doing this the minimum coil radius required to achieve the gradient of the quadrupole has to be calculated. This is technology dependant and the simplest expression for this is Equation 1.10 but more complex expressions can also be implemented. This coil radius can be worked out internally in the MADX mother file.

Next MADX has to subtract the space taken up by other components such as the insulation, beam screen and shielding from the coil radius. The simplest and most common triplet beam pipe geometry is circular, but in principle MADX is capable of computing the BSC for more complex geometries too. An example of the result from running the aperture module on the same triplet as shown in Figure 3.5b is shown in Figure 3.7. The BSC was calculated with the FCC-hh beam parameters [82]. As a result of the slicing, the β functions within the quadrupoles in Figure 3.7 look smoother than in the drifts or in the previous Twiss plots.

Pymadx can also be used to read the output file containing the results of the aperture computation and store it in python. The code can then extract the minimum BSC for each of the matched triplets to find the triplet with the largest BSC. Figure 3.8 shows the results of a scan using the MADX aperture module on matched, finite triplets over the same domain as Figure 3.4. It is noticeable that the the BSC is zero for a relatively large area in parameter space, this is because the matching module was not able to find a solution in these areas and hence the optimisation code set the BSC to zero.

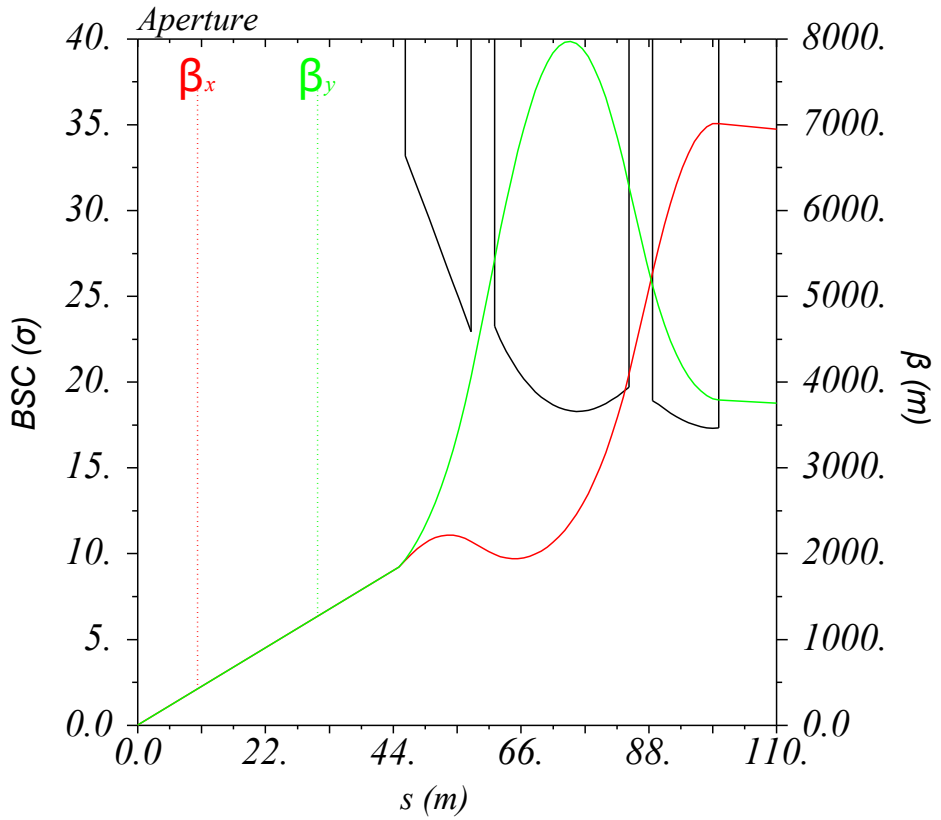

Figure 3.7: Example of MADX aperture output for a matched triplet.

A complete scan as shown in Figure 3.8 is very computationally intensive and can take several hours of CPU time to produce. This can be sped up by an order of magnitude if the domain over which this precise scan is performed is reduced to a smaller area in parameter space. The location of this area can be determined using the results of the fast FOM scan since the results of the two methods are in relatively good agreement, as one can see from Figures 3.4 and 3.8. In practice, when optimising the triplet for any machine it is advisable to start off with a large range around the maximum FOM and narrow it down based on the observed behaviour of the BSC.

It should be noted that many hadron colliders have round optics at the IP with $\beta_x^* = \beta_y^*$ and $\alpha_x^* = \alpha_y^* = 0$, with anti-symmetric optics such that normalised quadrupole

strength $k(-s) = -k(s)$ around the IP. In this case it is sufficient to perform the scan in one triplet because the anti-symmetry implies that $\beta_y(s) = \beta_x(-s)$ and $\alpha_y(s) = \alpha_x(-s)$ around the IP, so that the BSC of the triplets on the left and right side of the triplet are the the same, provided the aperture of the beam pipe is round. If an optics with unequal β^* or with a more complex beam pipe model was considered the code would have to be modified in order to do two aperture scans in MADX, one for each side. This modification can be easily applied by modifying the MADX mother file.

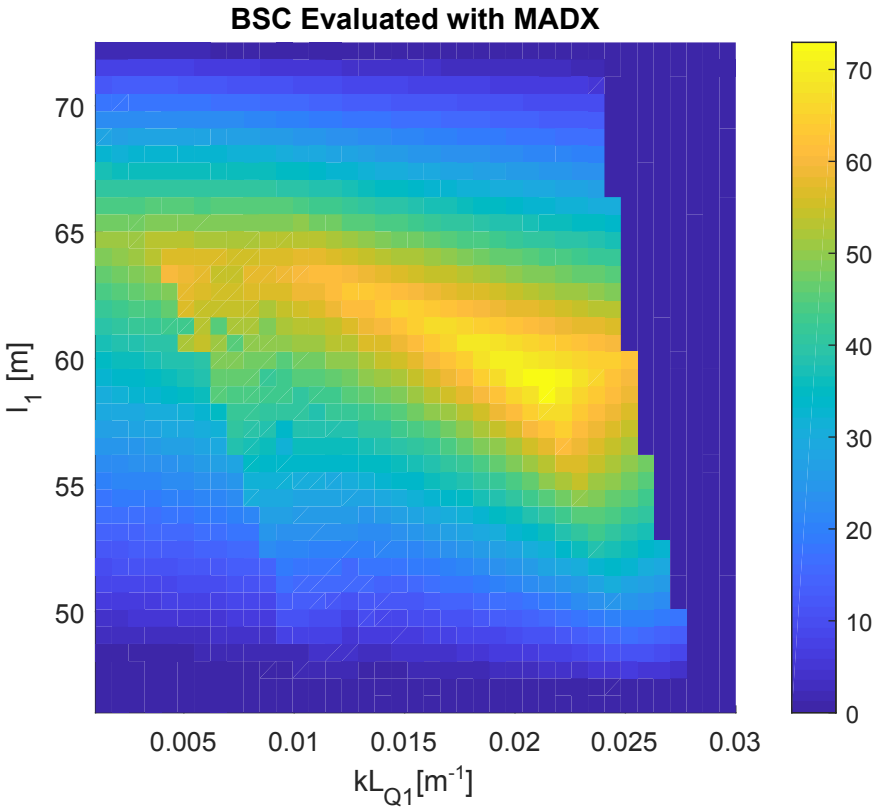

Figure 3.8: Example of BSC scan produced using MADX aperture module on matched triplets.

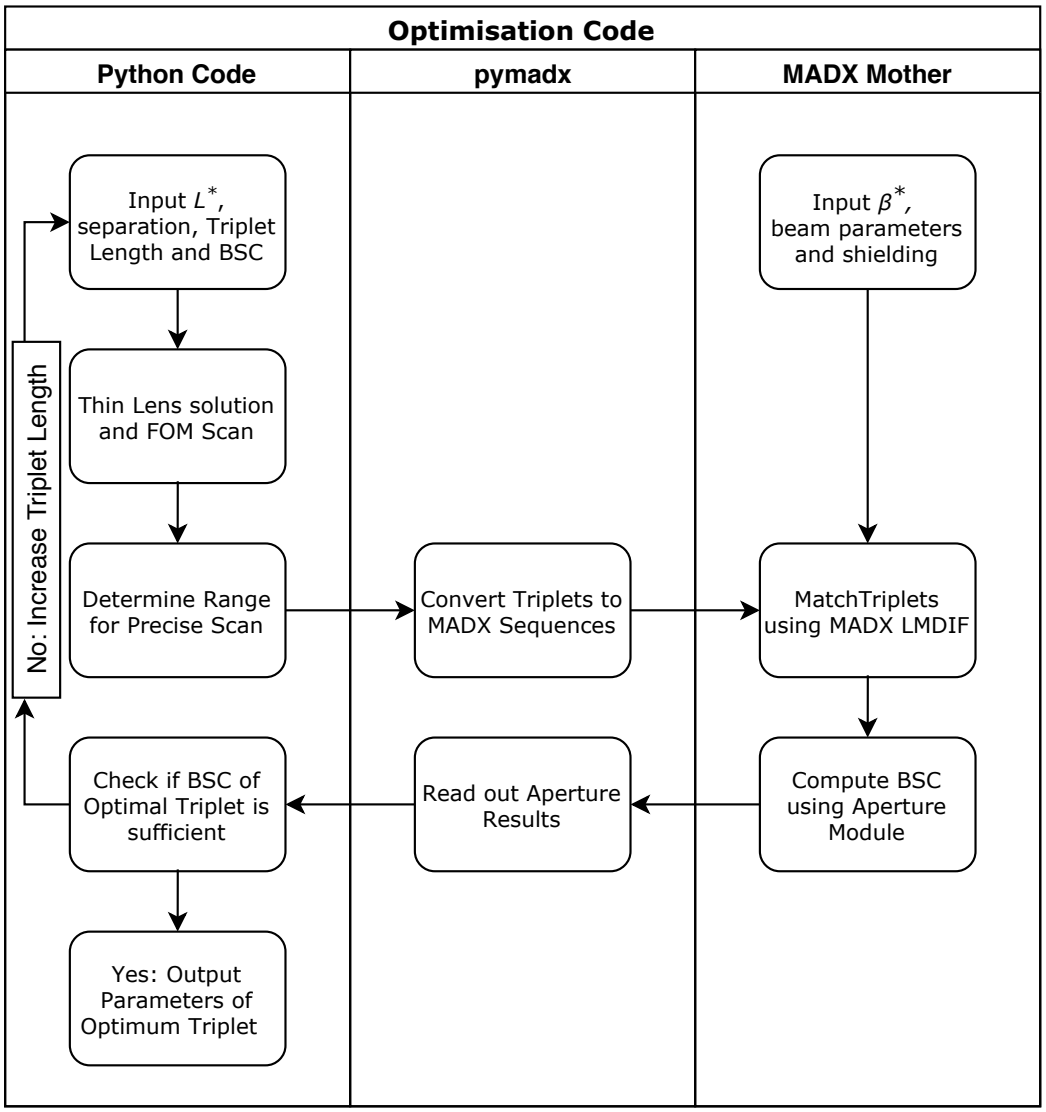

Figure 3.9: Diagram outlining functionality of the Triplet Optimisation Code.

3.3.3 Optimisation Code Overview

The functionality of the optimisation code is shown in Figure 3.9. Initially one can specify the required BSC as well as the design constraints such as L^*, the separation between quadrupoles, the amount of shielding required in each quadrupole and the relationship between aperture and quadrupole strength in the main python code and the MADX mother files. The user also has to specify the β^* and the beam parameters

in the MADX mother file for aperture calculations.

Next, a fast FOM scan is performed for this triplet length and the maximum FOM is determined. A sensible range about this maximum is then chosen for a more precise scan where the initial guess is based on the thin lens solution which is then converted to MADX using pymadx. The scan matches the solutions and works out the BSC using the precise MADX aperture module. If the configuration with the largest BSC does not fulfil the acceptance requirements the code goes back to the first step but automatically increases the triplet length. This is repeated until a triplet with enough BSC is found; the code then prints out the parameters of this triplet and produces a plot of the optics and BSC.

3.3.4 Modifications and Outlook

The Triplet Optimisation Code offers a method to systematically find a triplet that is as short as possible whilst still offering enough BSC. However, the code can readily be modified to fulfil other purposes. One could, for instance, use it for a design that is driven by limitations other than BSC. An example could be a triplet design that aims to reduce the natural chromaticity of an accelerator in order to reduce the cost and space of sextupole magnets. This could be especially interesting for triplet upgrades of existing machines where the sextupoles are already installed in the arcs.

From Equation 1.33, the chromaticity is proportional to the integral of $k\beta$, hence a new thin lens FOM can be defined that aims to approximate this as

$$FOM = \int k_z \beta_z \approx \sum_i k_{zi} \beta_{zi} L_{Qi} \propto \sum_i k_{zi} z_i^2 L_{Qi} = \sum_i g_{zi} z_i^2, \tag{3.19}$$

where $\beta_z \propto z^2$ was used and z can be determined in each lens using a tracking similar

to that for the aperture FOM. The code could then do a more precise scan of matched triplets and work out the natural chromaticity using the MADX Twiss module in a similar way as before.

Another interesting modification could arise from dropping the requirement that $L_{Q3} = L_{Q1}$. This would leave an additional degree of freedom to improve the BSC. At the same time this addition freedom would increase the computation time by an order of magnitude. For this thesis it was decided to use this constraint because it provides practicality and is common practice. However, an interesting investigation could be a more general exploration of the optimum layout. This could be done for a single triplet length to find out for which configuration the BSC is the largest and how significant the impact of the choice of $L_{Q3} = L_{Q1}$ is.

A last modification could look into ways of increasing the precision of the thin lens solution and the FOM. One of the main limitations of the thin lenses is that they represent very long quadrupoles and the β functions within these quadrupoles change largely. One way of improving this might be to use several equally spaced thin lenses with the same strength to represent each quadrupole. This could also give a better estimate of the orbit in the quadrupole and in turn improve the accuracy of the FOM. The downside to this is that it would result in a transfer matrix with g_i raised to higher orders. This might make it harder to find a solution, moreover, it would result in several roots to the equation and it would be harder to determine which of these roots is a physical solution.

3.4 Fringe Field Optimisation

The optimisation code was written primarily to create short triplets with enough BSC for the FCC-hh and later the HE-LHC, the results of which will be shown in Chapters 4 and 5. However, as discussed in Section 3.3.4, the structure of the optimisation code can easily be changed to solve other problems. One opportunity to do this is the optimisation of the NICA final focus triplet to reduce the effect of fringe fields on the DA. The DA decreases drastically once fringe fields are turned on during the tracking, this effect is thought to be largely dominated by the fringe fields in the triplet, where the β functions are the largest.

3.4.1 Application to NICA EIR

Whilst most of the NICA design is in a very mature status, the ring has a very low DA when particles are tracked with fringe fields. The NICA triplet has a total length of 4.1 m, of which 3.5 m are occupied by the triplet quadrupoles which are separated by 30 cm drifts. This triplet is used to focus the beam to a $\beta^*_{x,y} = 0.6$ m with $\alpha^*_{x,y} = 0$. Initially, the optics was symmetric around the IPs and all triplet magnets were powered in series. However, studies by members of the NICA design team showed that anti-symmetric layout with individually powered quadrupoles drastically increases the DA with fringe fields. A plot of the optics of this anti-symmetric layout is shown in Figure 3.10.

Instead of evaluating functions based on the Lyapunov exponent for many particles, for the NICA collider, the DA is determined by short term tracking, which calculates the position of particles travelling around the ring thousands of times and

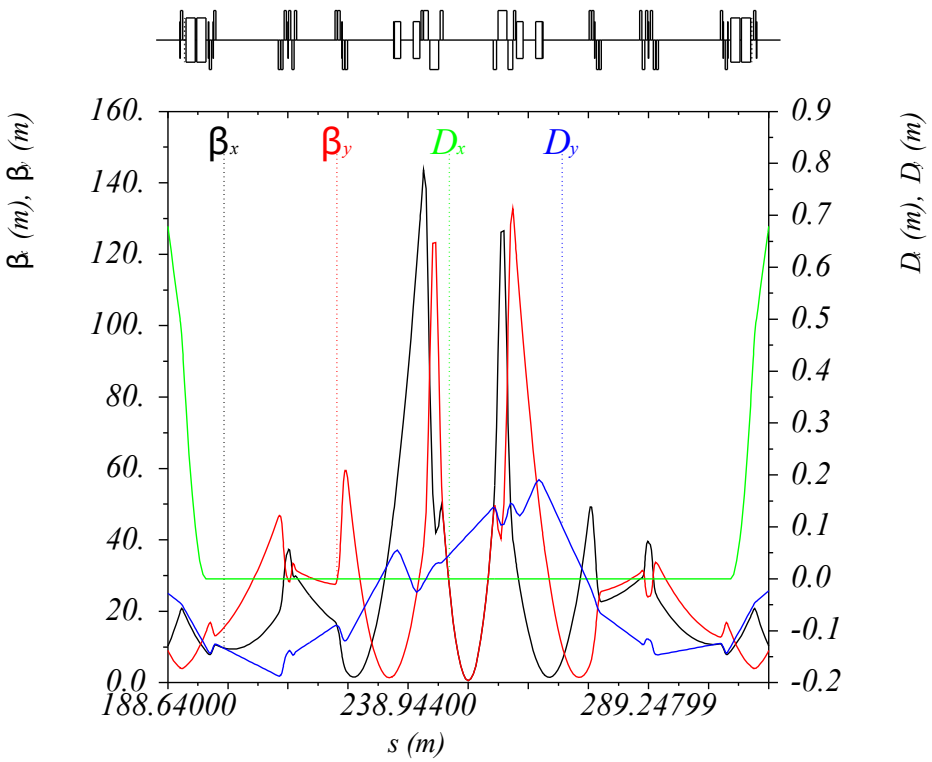

Figure 3.10: Original NICA EIR optics with anti-symmetric triplet.

checks which particles are lost. The tracking is done using the Polymorphic Tracking Code [94] (PTC) which is integrated into MADX. The PTC tracking is done for 40 particles originating at the IP with the initial x coordinate increasing from 0 to 2 cm over 2000 turns and similarly 40 particles with the initial y coordinates in the same range. PTC calculates the positions of each particle every turn for on momentum particles and a ring with no magnet errors. It then determines which particles are lost before the 2000 turns were completed. The positions obtained from this tracking are shown in Figures 3.11a and 3.11b, from which one can also get a qualitative idea of the stable area in phase space.

For these optics the PTC tracking determined that the particle with the largest amplitude that was not lost had an initial amplitude of $x_{max} = 7.0$ mm, this can also

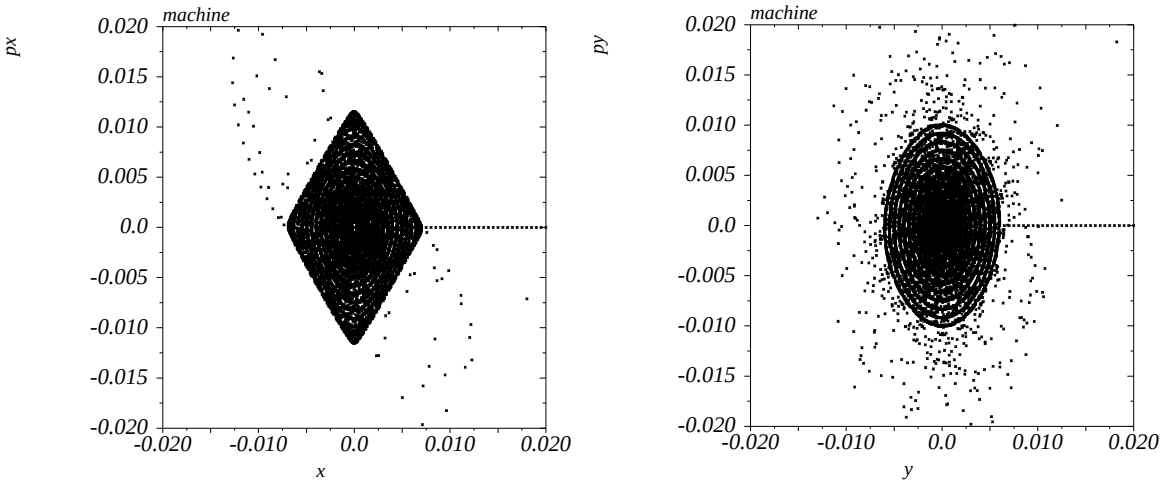

(a) Horizontal Plane (b) Vertical Plane

Figure 3.11: Results of PTC tracking for 40 particles over 2000 turns using original anti-symmetric triplet.

be seen from Figure 3.11a. Since $\alpha_x = 0$ and at the IP, one can use Equation 1.39 to show that

$$x_{max} = N_{DA}\sigma_x = N_{DA}\sqrt{\epsilon_x \beta_x}, \tag{3.20}$$

where N_{DA} is the size of the DA in units of standard deviation. This can be rearranged to give

$$N_{DA} = \sqrt{\frac{x_{max}^2}{\epsilon_x \beta_x}}. \tag{3.21}$$

Using $\beta_x = 0.6$ m and $\epsilon = 1$ µm this yields a DA of approximately 9.0 σ. The last stable particle in the vertical plane originates at $y_{max} = 6.0$ mm. Since β^* and ϵ are the same in both planes, the DA in the vertical plane can be worked out using the same constants to give 7.7 σ.

3.4.2 Tracking with Fringe Field Kicks

Since the fringe fields in the triplet are thought to be one of the biggest factors contributing to the low DA [95], an optimisation of the triplet to reduce this effect could

help improve the DA. The infrastructure created for the triplet optimisation code can be exploited for this optimisation. The thin lens solution and translation to MADX can be used to define a wide variety of triplets, however, instead of testing these triplets for BSC, the code can test for a metric that tries to measure the magnitude of the fringe field effects.

Because the design of NICA is in a very mature stage, there is very little room to adjust the length of the triplet, therefore it can be kept constant during these scans with $L_{Trip} = 4.2$ m and $d = 0.3$ m. Moreover, the constraint $L_{Q1} = L_{Q3}$ was not applied in this design as it was not valid in the initial design. This leads to a new free variable so that l_2 can also be varied.

The scan was set up to probe thirty values of l_1 and l_2 as well as six values of g_1. The lower resolution in g_1 than in the other variables can be justified by the results of Figure 3.8 that show the BSC slopes steeper as you go along the l_1 axis than as you go the $k_1 L_{Q1}$ axis. This is probably because for a given spatial configuration, the MADX matching might converge to a similar solution.

The triplets are imported into MADX and matched in the same way as was done for the aperture code. The key difference being that this was done for all triplets and there was no selection performed using thin lenses. Since the aperture module was not used in this case the MADX computations are significantly faster. The strengths of the matched quadrupoles are read out using pymadx.

Since PTC tracking would require a more carefully matched machine, which has to be done by hand for each triplet, a simplified tracking is done in the python script. This tracking traces the paths of 200 random particles originating from the

IP through the triplet using the transfer matrices for a finite quadrupole and drift given by Equations 1.19 and 1.18. The same random particles with initial positions and momenta are computed using normal distributions in x, y, x' and y' with a zero mean and a variance of $\sigma_z = \sqrt{\epsilon_z \beta_z^*}$ and $\sigma_{z'} = \sqrt{\epsilon_z / \beta_z^*}$, as defined in Equation 1.39, were used for each triplet.

Initially, the tracking is performed without fringe field effects and the co-ordinates of each particle at the exit is recorded. The tracking is then repeated but with fringe fields kicks applied to each particle at the entrance and exit of each quadrupole. The fringe field kicks at the entrance are given as [96]

$$\Delta x = \frac{k}{12}(x^3 + 3xy^2), \tag{3.22}$$

$$\Delta x' = -\frac{k}{4}[(x^2 + y^2)x' - 2xyy'], \tag{3.23}$$

$$\Delta y = -\frac{k}{12}(3x^2 y + y^3), \tag{3.24}$$

$$\Delta y' = \frac{k}{4}[(x^2 + y^2)y' - 2xyx'], \tag{3.25}$$

where the sign is reversed at the exit.

The effect the fringe fields have on the particles can be determined by comparing the final positions of the particles without and with fringe field kicks. To quantify how big this effect is, a second figure of merit was defined as

$$FOM_{fr} = \sum_i |\mathbf{z}_{0,i} - \mathbf{z}_{fr,i}| \times \sum_i |\mathbf{z'}_{0,i} - \mathbf{z'}_{fr,i}|, \tag{3.26}$$

where $\mathbf{z} = \begin{pmatrix} x \\ y \end{pmatrix}$, $\mathbf{z'} = \begin{pmatrix} x' \\ y' \end{pmatrix}$ and the indices 0 and fr refer to the particles tracked without and with fringe fields respectively. For every spatial configuration, the triplet strength solution with the lowest FOM_{fr} is recorded and the corresponding FOM_{fr}

is written into a file for further evaluation and processing.

3.4.3 Symmetric and Anti-Symmetric Solutions

As mentioned above, the NICA collaboration found that the DA was improved when an anti-symmetric optics was implemented. To test the hypothesis if anti-symmetric triplets are automatically advantageous and to understand the general relationship between symmetry of the triplets and DA, the code was modified again to explore EIRs with different symmetries.

This is done by creating and matching triplets as before but then performing the tracking not from the IP to the exit through a single triplet but from the entrance of the system, through a triplet, the IP and another triplet to the other exit of the system. The second triplet can be set to be symmetric or anti-symmetric compared to the first matched one.

Since the optics at the entrance depend heavily on the matching, the coordinates of the tracked particles at the entrance are determined by tracking 200 particles from the IP distributed in the same way as described in Section 3.4.2 back to the entrance of the system without any fringe field kicks. The particles are then tracked to the exit of the system with fringe field kicks with a symmetric and anti-symmetric layout. Due to symmetry, the tracking without fringe field does not have to be repeated since $\mathbf{z_{exit}} = \mathbf{z_{entrance}}$ in the symmetric case and $\begin{pmatrix} x_{exit} \\ y_{exit} \end{pmatrix} = \begin{pmatrix} y_{entrance} \\ x_{entrance} \end{pmatrix}$ in the anti-symmetric case. The FOM_{fr} is recorded for both the symmetric and anti-symmetric cases and written into separate files.

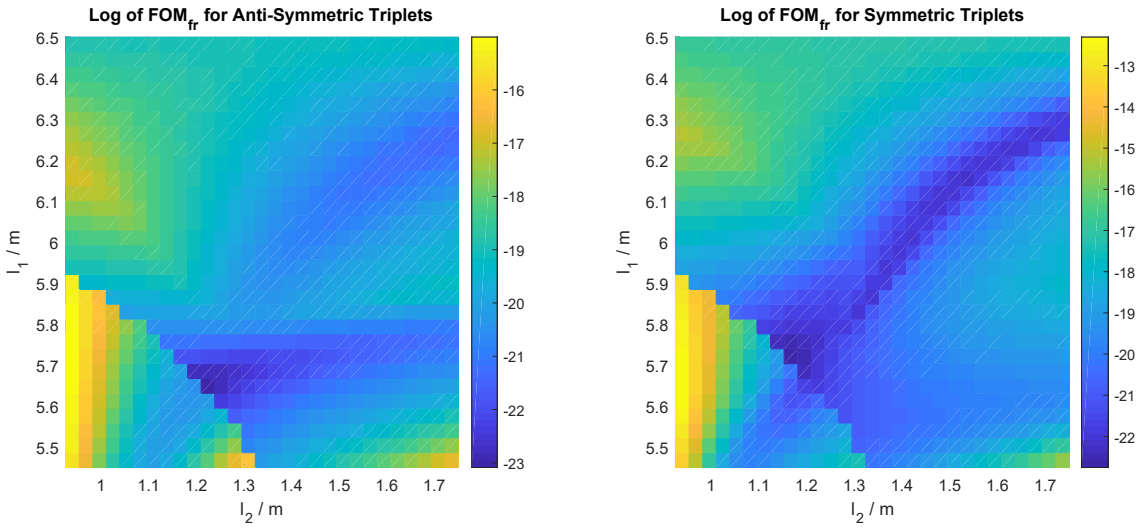

Figure 3.12: Log of FOM_{fr} for symmetric and anti-symmetric triplet configurations.

3.4.4 Results

The results from the optimisation code are shown in Figure 3.12, where the logarithm of the FOM_{fr} is plotted to show the difference between the various configurations more clearly. Overall the results of the two scans show very similar structures for the symmetric and anti-symmetric case with the lowest FOM achieved with an anti-symmetric triplet with $l_1 = 5.63$ m and $l_3 = 1.21$ m.

For a better comparison of the symmetric and anti-symmetric layouts, the FOM was compared for each layout and the results are plotted in Figure 3.13, where blue squares represent areas where anti-symmetric triplets are preferable and yellow represents areas where symmetric triplets have a lower FOM. From this one can see that the anti-symmetric configuration is indeed better in most situations, however, in the areas where the FOM is especially low, the symmetric configuration seems to be better.

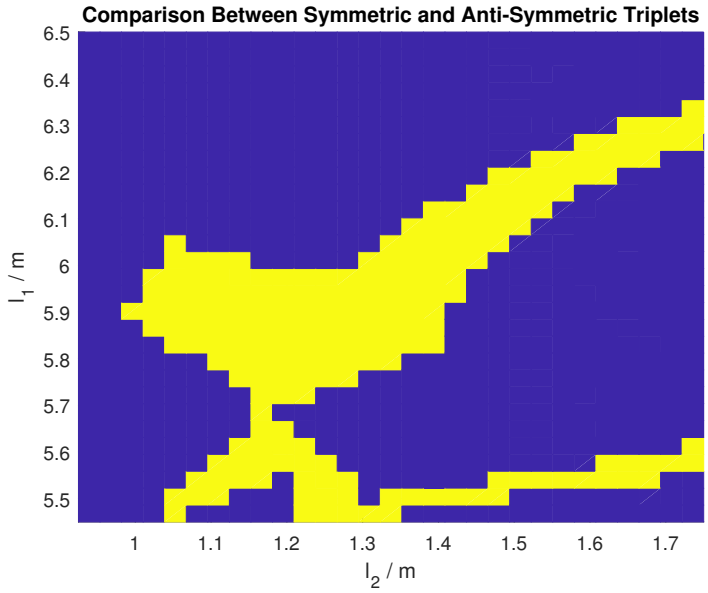

Figure 3.13: Comparison of FOM_{fr} between symmetric and anti-symmetric triplets.

The design parameters of the optimum triplet found are shown in Table 3.1. A significant observation one can make from these results is that the last quadrupole is field free, making this triplet a doublet solution. The doublet was integrated into the EIR and the optics was re-matched, the result is shown in Figure 3.14.

	Q1	Q2	Q3
Length [m]	0.82	0.76	1.93
k [m^{-2}]	0.758	0.707	10^{-12}

Table 3.1: Table showing design parameters of optimum triplet found using NICA optimisation.

The DA was tested using the short term tracking with PTC and fringe fields. The results are shown in Figures 3.15a and 3.15b with the last surviving particle at $x_{max} = 8.0$ mm and $y_{max} = 5.5$ mm. This translates to a DA of 10 σ in the horizontal and 7.1 σ in the vertical plane. Compared to the original triplet this is an improvement of 11% in the horizontal and a decrease of 8% in the vertical plane.

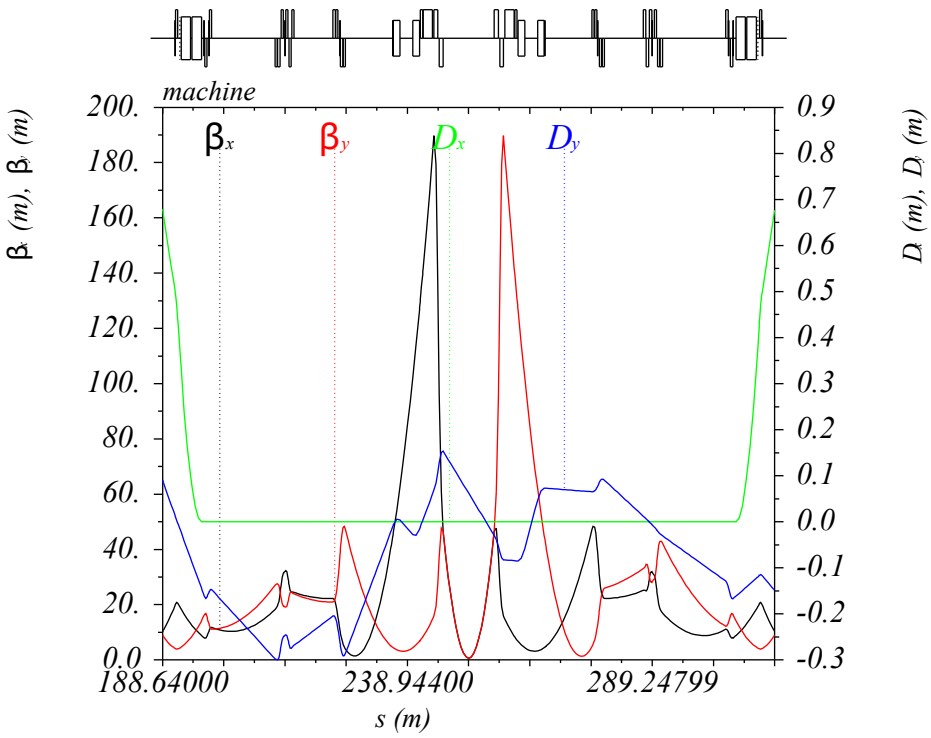

Figure 3.14: NICA EIR optics with optimised triplet.

Overall, however this translates to a large improvement in the DA that supports the results of the FOM.

In order to increase the DA further the entire space available can be used for the doublet so that the focusing can be achieved with lower gradient quadrupoles. To do this the code can be modified to restrict $L_{Q3} = 2$ cm and only use the strengths of Q1 and Q2 for the matching. This was done and parameters of the optimum doublet found is shown in Table 3.2. In this case the optimum solution was found in a symmetric case, so a symmetric triplet was integrated into the EIR and matched to the arc as shown in Figure 3.16.

Again the tracking was repeated using the PTC tracking module for short term DA tracking in MADX with the new optics. The results are shown in Figures 3.17a and 3.17b. The last stable particles after 2000 circulations are at $x_{max} = 8.5$ mm

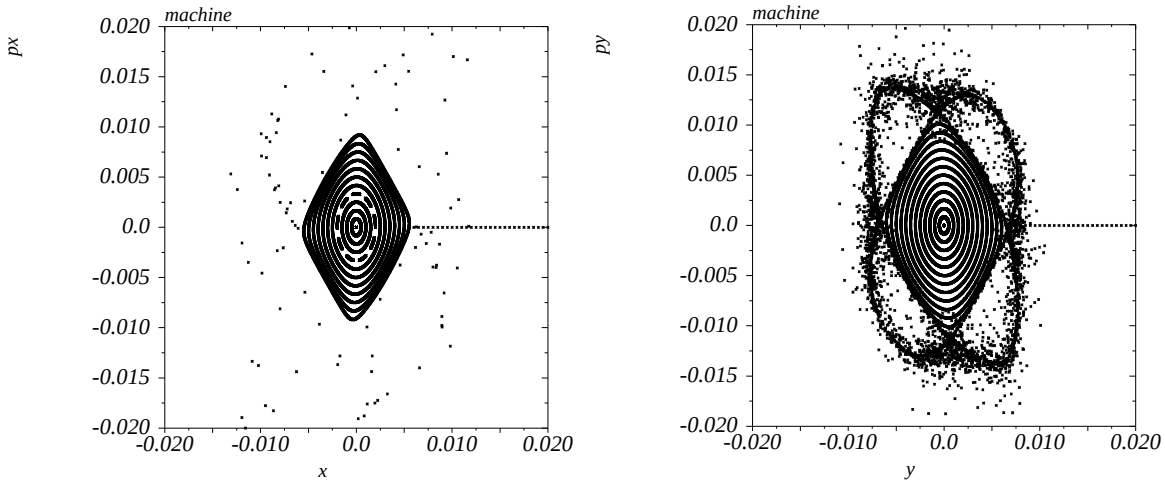

(a) Horizontal Plane (b) Vertical Plane

Figure 3.15: Results of PTC tracking for 40 particles over 2000 turns using optimised anti-symmetric triplet.

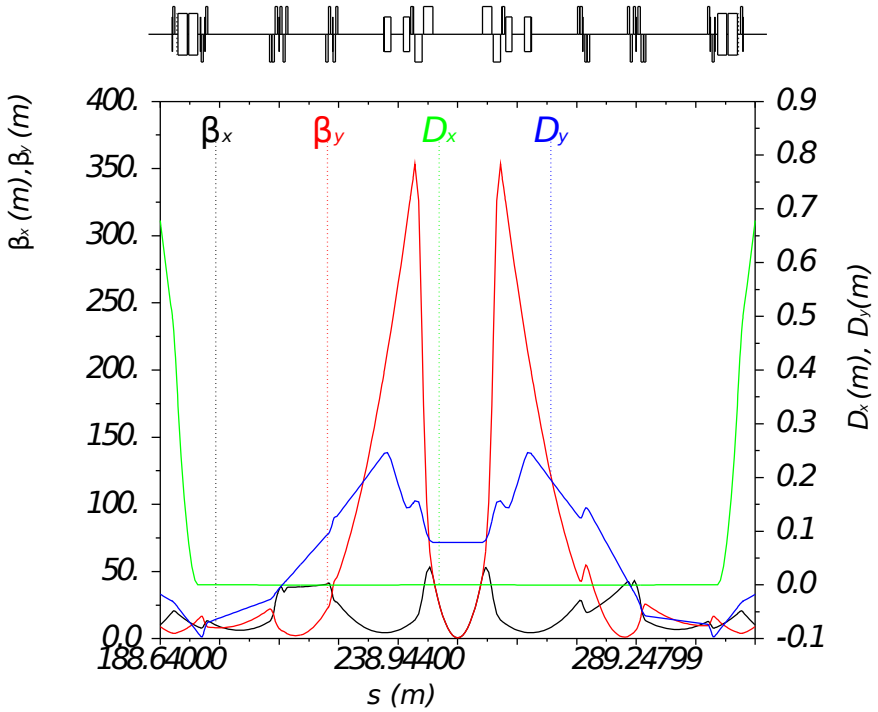

Figure 3.16: NICA EIR optics with optimised doublet.

	Q1	Q2	Q3
Length [m]	1.97	1.51	0.02
k [m^{-2}]	0.239	0.239	10^{-12}

Table 3.2: Table showing design parameters of optimum doublet found using NICA optimisation.

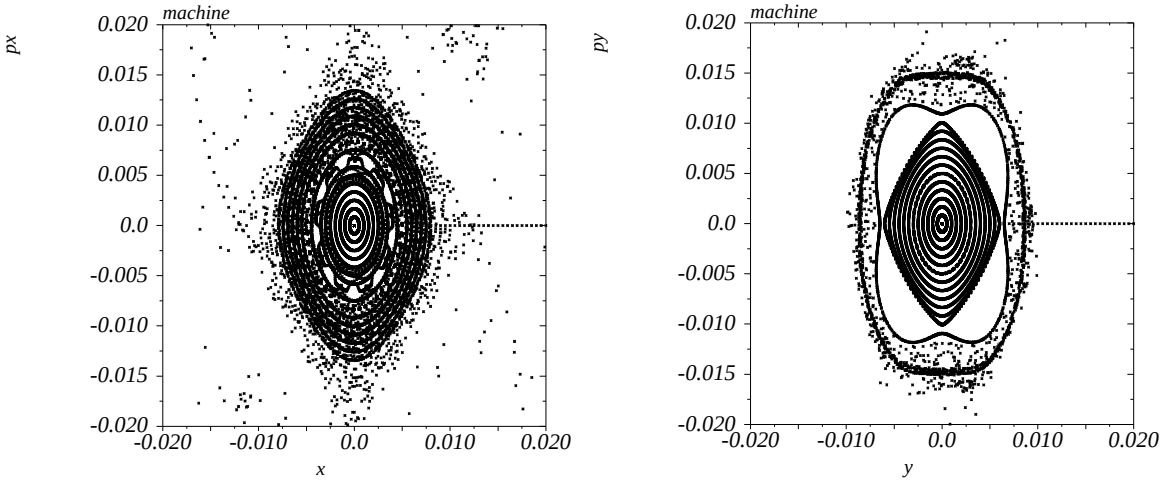

(a) Horizontal Plane (b) Vertical Plane

Figure 3.17: Results of PTC tracking for 40 particles over 2000 turns using optimised symmetric doublet.

and $y_{max} = 9.0$ mm, which corresponds to 11.0 σ and 11.6 σ respectively. This is a significant increase in DA by 22% in the horizontal and 51% in the vertical plane compared to the original anti-symmetric triplet. Moreover, these values of over 10 σ mean that the DA is a lot more robust once magnet errors are added on top of the fringe fields and more long term tracking is applied.

Overall, the optimisation of the NICA triplet has shown that the triplet code can be altered very easily to fulfil other tasks instead of aperture optimisation. By using a FOM that is based on a simplified particle tracking and by scanning through the parameter space important insights into the effect symmetry has on the DA with fringe field effects were made. The fact that the triplet optimisation converged to a

doublet like configuration inspired the installation of a doublet in order to increase the DA, the benefit of which was not initially obvious. Most importantly, the optimisation code helped come up with a design with a much larger DA than before, providing the NICA collaboration a possible alternative should the low DA of the initial design persist and cause problems.

3.5 Conclusion and Outlook

In the first half of this chapter a Triplet Optimisation Code was introduced that can be used to find the shortest possible triplet that has apertures large enough to accommodate enough shielding and is able to fulfil the optics requirement. In a first approximation the code uses an analytic solution obtained from a simplified thin lens system. The novelty of this solution is that it simplifies the focusing properties of a triplet to a single constraint per plane, leaving many degrees of freedom for the optimisation. The code then uses a thin lens FOM to identify a smaller area in parameter space in which a more precise scan can be performed. The more precise scan uses the thin lens solutions as a first guess that is converted into a finite length equivalent and passed into MADX for precise matching and aperture computations.

This Triplet Optimisation Code can be used to quickly and systematically find the shortest possible triplet for a given accelerator. On top of this, the tools developed during this process can be modified in order to solve other triplet optimisation problems. This is demonstrated by exploring the effect of fringe fields on the DA of the NICA accelerator. To do this, the paths of test particles are tracked through the EIR with a pair of matched triplets with and without fringe field effects to identify the

configurations where the fringe fields have the smallest impact. This process resulted in a symmetric doublet which significantly increases the DA once integrated into the lattice. The fact that the optimisation resulted in a doublet shows the benefit of this type of optimisation, which assumes very little prior information. This motivates further expanding the range of applications of these tools to a wider selection of machines and problems. One aspect not considered in this study is the impact the size of the magnetic aperture has on the fringe fields. The doublet has significantly larger β functions in the triplet requiring a larger aperture. exploring this would be a possible extension of this study.

Chapter 4

FCC-hh Triplet Optimisation

4.1 Motivation

As mentioned in Chapter 2, the baseline design for the FCC-hh EIR contains a triplet based on a scaled LHC triplet. Before optimisation, this triplet was so long that the EIR length had to be increased from 1.4 km to 1.6 km. Along with the more general reasons for finding a short triplet outlined in Section 3.1, this was another motivation to find a short triplet using the optimisation code. Moreover, designing a triplet without basing it on any prior assumptions or knowledge about ideal designs can lead to a design more tailored to the individual situation. Or alternatively, if the alternative design converges to a triplet similar to the baseline, it could confirm the assumptions used so far.

4.2 Design Goals

The triplet has to be able to achieve a β^* of at least 0.3 m and ideally have a β^* reach slightly lower than this, which would provide a handle to increase the peak luminosity if needed. It also has to support a crossing angle of 15.5 σ, which translates to 176 µrad in the $\beta^* = 0.3$ m case with a HL-LHC like normalised emittance of 2.2 µm. The

triplet has to do this whilst leaving a BSC of 15.5 σ. This has to be achieved for on momentum particles with no alignment tolerances but with closed orbit tolerances of 2 mm and a β beating of 20 %.

The aperture also has to have enough space for shielding to protect the triplet from collision debris. Since the levels of debris produced in the FCC-hh are unprecedented and the way this debris is spread along the triplet depends largely on the design and the length of the triplet, the amount of shielding required to protect the triplet was initially unknown. Therefore, the triplet optics design was done in close co-operation with energy deposition studies done using the FLUKA code [97].

The way this co-operation works is that a first estimate of the required shielding is made and the Triplet Optimisation Code is used to find the ideal triplet for this case. This triplet is then integrated into the EIR and the shielding is slightly adjusted to be compatible with the matched optics. The energy deposition in the matched triplet is then tested using a FLUKA model. Based on the results the shielding estimate is increased or decreased and the optimisation, matching and testing is repeated. This is done until a triplet that meets all criteria is found, this work flow is illustrated in Figure 4.1. Moreover, if design criteria in the machine slightly change during the optimisation process, they can be adjusted in the various processes during the iterations.

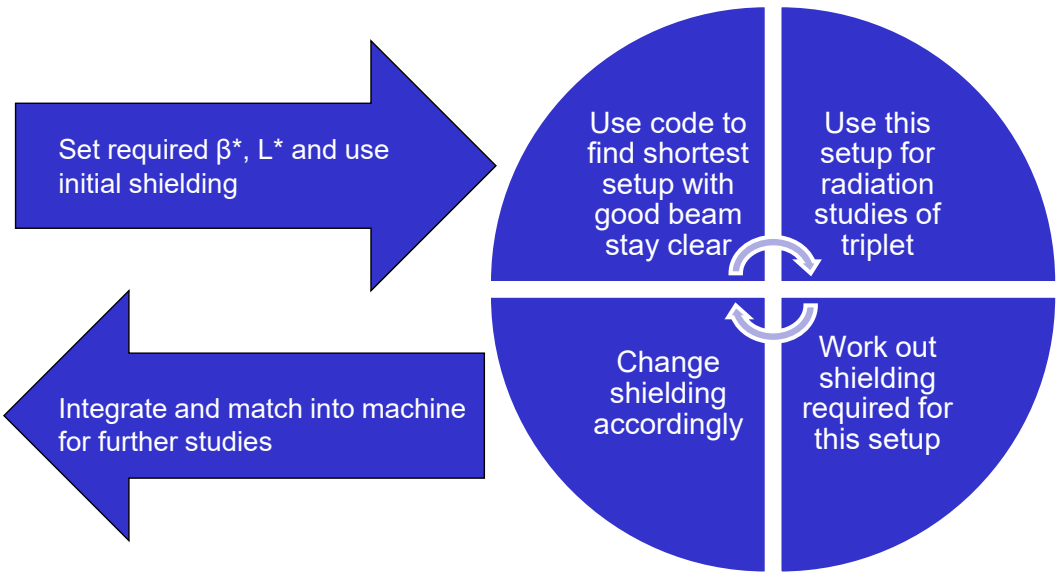

Figure 4.1: Illustration of work flow for co-operation of optics design and energy deposition studies.

4.3 Application of Triplet Code

4.3.1 Input and Modifications

Based on the design specifications of the BPMs and orbit correctors, that have to be nested in the FCC-hh triplet, the main quadrupoles Q1, Q2 and Q3 had to be separated by 5 m drifts to allow enough space to install these elements. Moreover, the main quadrupoles have to be split into sub-magnets that are no longer than 15 m for transport purposes. Each sub-magnet has to be housed in an individual cryostat; the end caps and connectors of these cryostats take up some space, resulting in the sub-magnets having 2 m drifts between them.

Since the triplet code only takes into account the drifts between the main quadrupoles, the distance between the sub-magnets has to be added to these drifts in a first approximation. Based on the results in [82] it can be expected that the triplet found

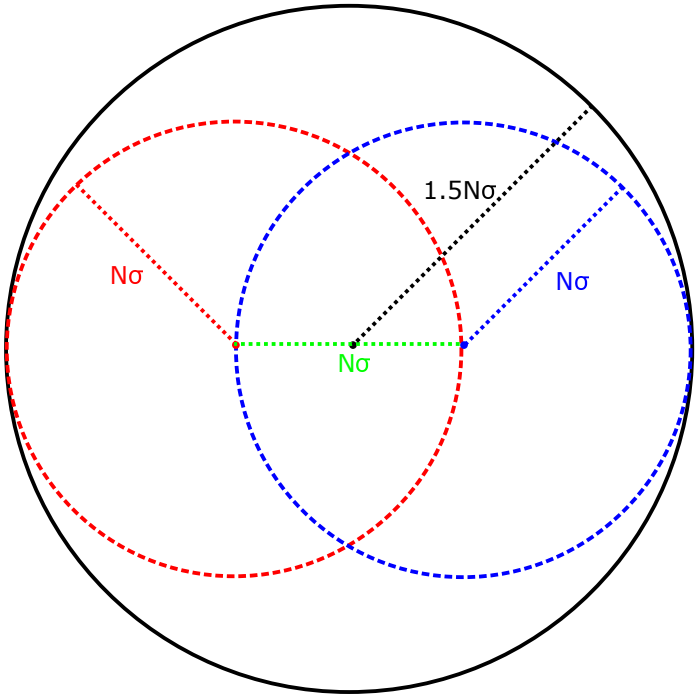

Figure 4.2: BSC equivalent for two beams with $N\sigma$ separation and $N\sigma$ BSC each.

has a magnetic length of ~ 100 m. This would result in 100 m/15 m ≈ 7 sub-magnets spaced by 2 m each. Hence the quadrupole separation in the triplet code was set to $5 \text{ m} + \frac{14 \text{ m}}{2} = 12$ m.

The BSC is calculated using the beam parameters of the FCC-hh with the tolerances outlined above. Whilst the individual beams need a BSC of 15.5 σ, this BSC also has to take into account the reduction of the BSC due to the beams not travelling through the centre of the quadrupoles. The crossing angle of 15.5 σ results in a beam-beam separation of 15.5 σ in the quadrupoles. As illustrated in Figure 4.2, this is equivalent to one beam with $1.5 \times 15.5\ \sigma = 23.25\ \sigma$ BSC travelling through the centre of the quadrupole. Hence, the Optimisation Code is set to find the shortest possible triplet with 23.25σ minimum BSC.

The final drift, L^*, is set to 45 m and the β functions at the IP are set to $\beta_x^* =$

$\beta_y^* = 0.2$ m, which is slightly lower than the experimental requirements but ensures the triplet is able to have some margin to achieve lower β^*. After an initial run with larger BSC scans around the highest FOM, it was found that an interval of $l_1 \pm 6\%$ and $g_1 \pm 0.005$ m^{-1} at a resolution of 25×12 around the maximum FOM was most suitable for the precise scan in this situation. Finally, l_4 was set to 500 m as an approximation of the distance between the triplet and the matching section.

4.3.2 Field vs. Aperture

Initially the coil aperture for a given quadrupole gradient was approximated using Equation 1.10, with $\Delta B = 11$ T. After consultation with the FCC-hh magnet design team an estimate of the achievable gradient for a set of coil radii was produced [98], the estimates produced by the magnet team are shown in Table 4.1. In order to find a function that describes the relationship between the radius, r, and the gradient, G, as described in Table 4.1, the data was fitted using a function of the form

$$r = \frac{A}{G^\alpha}, \tag{4.1}$$

where α and A are determined from the fitting. The line of best fit was found with $A = 29.96$ and $\alpha = 1.215$. The fact that $\alpha > 1$, as we would expect from Equation 1.10, implies that Equation 1.10 is an overestimate at very high gradients. The values from Table 4.1 as well as the exponential fit of Equation 4.1 are shown in Figure 4.3, which also shows points calculated using Equation 1.10 and $\Delta B = 11$ T.

Radius [mm]	50	60	70	80	90	100	110	120	130
Gradient [Tm^{-1}]	193	166	149	133	120	110	102	94	88

Table 4.1: Estimate of gradients achievable for a given coil radius.

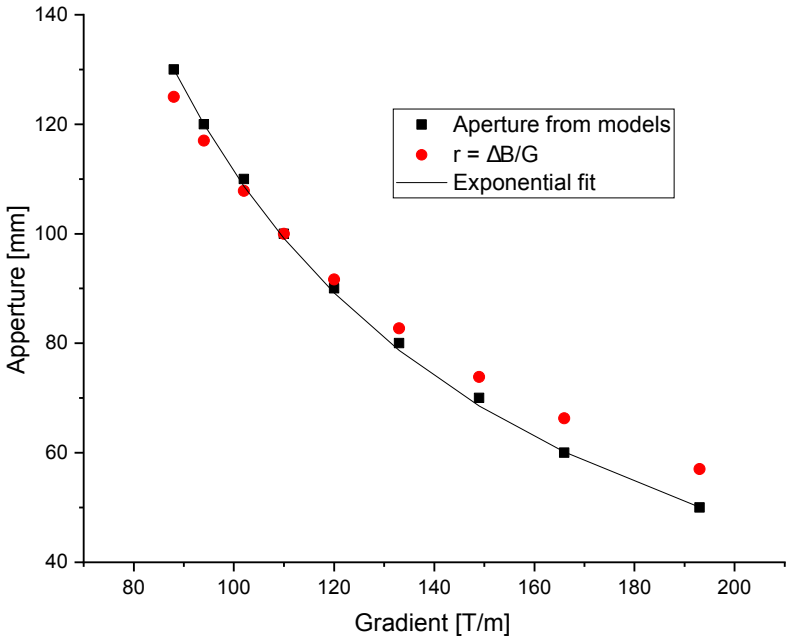

Figure 4.3: Magnet aperture for a given coil radius from model estimates, exponential fit and $\Delta B/G$ estimate.

From Figure 4.3, one can see that the $\Delta B/G$ is a relatively good first approximation, therefore it was kept for the thin lens FOM.

The MADX mother file was modified to read out the strength of the matched triplet quadrupoles and work out the coil radii using Equation 4.1. The MADX code then subtracts the widths of the cold bore, the liquid helium cooling channel, the kapton insulation, the beam screen and the beam screen insulation from the coil radius to work out the aperture available for the beam and shielding. The widths of these components for the FCC-hh were established together with the beam screen and magnet design team and are shown in Table 4.2. Finally, the width of the shielding has to be subtracted from this radius to work out the aperture available for the beams. This circular aperture can then be used for the the MADX aperture module.

In the first iterations the aperture for each quadrupole was calculated individually

Component	Radial Thickness
Cold bore	5.44 % of coil radius
Liquid helium cooling	1.5 mm
Kapton insulation	0.5 mm
Beam screen	2.05 mm
Beam screen insulation	2 mm

Table 4.2: Radial thickness of various components installed between quadrupole coil and beam in the FCC-hh.

Source: [99]

and all quadrupoles had different apertures. However, it was soon found that the collision debris would be spread more evenly throughout the triplet and there would be less peaks if all quadrupoles had a similar aperture. Therefore, the code was modified to use the largest quadrupole gradient from all three quadrupoles to compute the coil radius of all magnets. This would not only help reduce radiation peaks, but also reduce the number of different types of magnets that have to be designed and produced for the triplets.

4.3.3 Energy Deposition Studies

Whilst the energy deposition studies were not done in the scope of this thesis, the co-operation between the optics design and the energy deposition studies is an integral part of the work. Therefore, for completeness, the FLUKA model is briefly described here, a more detailed overview can be found in [100] and [101].

The collision debris at the IP was taken from proton-proton collision simulations using the DPMJET-III generator [102]. As well as the quadrupoles and dipole kickers, the full FLUKA model contains a Target Absorber Neutral (TAN) in front of the triplet, to shield it from the debris. A typical cross section of the FLUKA model of the

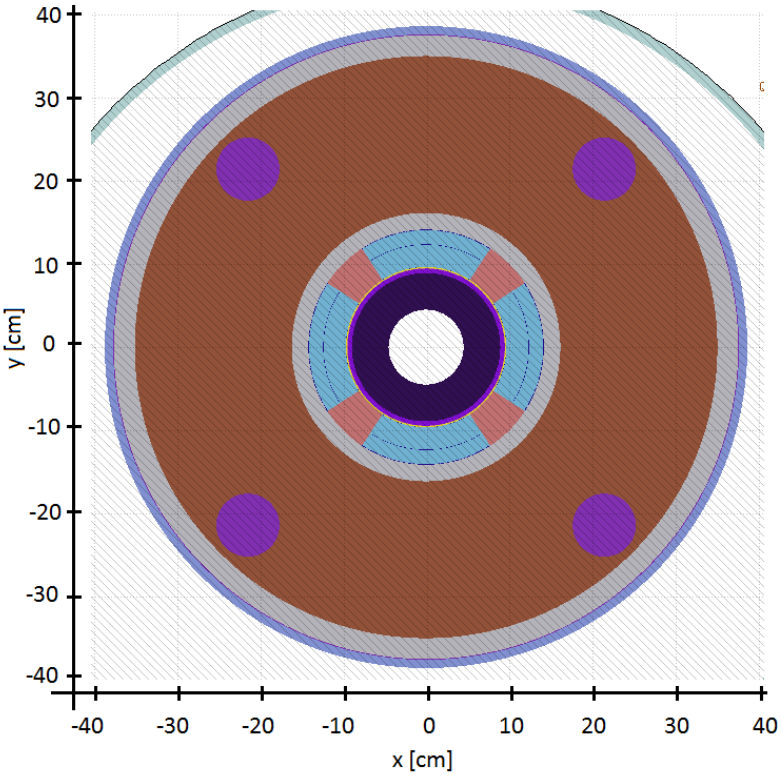

Figure 4.4: Transverse cross section of a quadrupole as in the FLUKA model.

Source: [101]

quadrupoles is shown in Figure 4.4, the model allowed one to easily parameterise the various apertures and thicknesses and adapt the model during the design iterations.

4.4 45 m L^* Solution

After several iterations the optimum solution is found for a triplet that has a uniform coil aperture and a shielding that varies from quadrupole to quadrupole. In the studies it was found that the largest amount of debris is deposited in Q1 and the lowest amount in Q3. At the same time the β functions are smallest in Q1 so it makes sense to have more shielding in Q1 and less in Q3. The Optimisation Code was run with 40 mm of shielding in Q1, 30 mm in Q2 and 20 mm in Q3. The

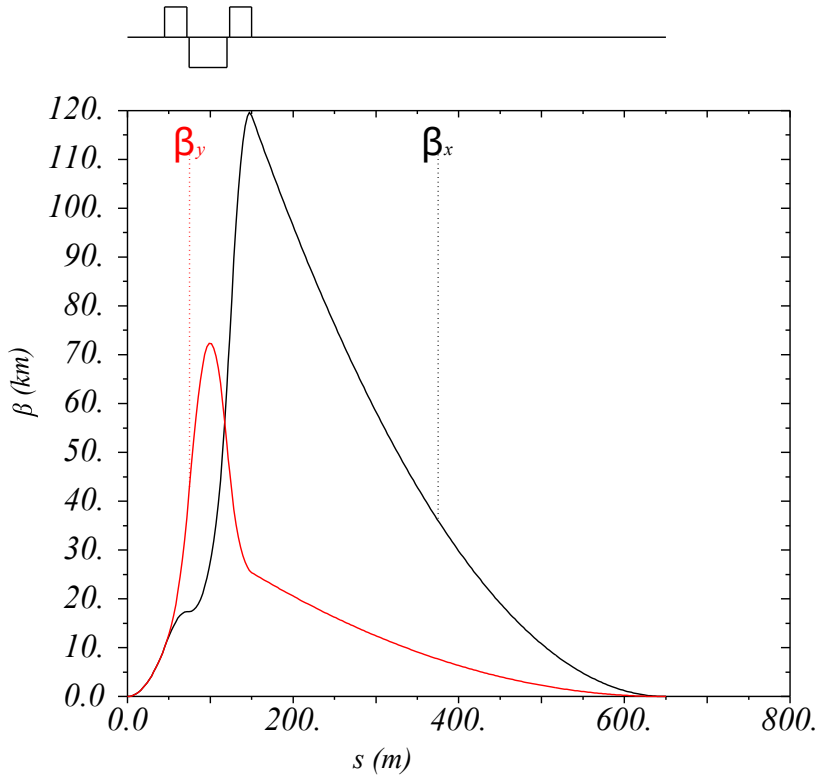

Figure 4.5: Optics of result from Optimisation Code for FCC-hh.

optimum triplet found using the code has quadrupole lengths of $L_{Q1} = L_{Q3} = 26.7$ m and $L_{Q2} = 45.5$ m and is shown in Figure 4.5.

In order to fulfil the requirement of not having magnets longer 15 m the quadrupoles have to be split into shorter sub-magnets. One of the advantages of having a uniform coil aperture is that fewer different magnet types have to be designed and built, this would be an even bigger advantage if all sub-magnets had the same length. Therefore the quadrupole length can be rounded to the nearest multiple of 15 m and split into sub-magnets of 15 m. In this case this implies increasing the length of Q1 and Q3 by 2.3 m and constructing it out of two 15 m sub-magnets, whilst decreasing the length of Q2 by 50 cm and splitting it into three 15 m sub-magnets.

This split triplet can then be integrated into the FCC-hh EIR and re-matched

to give acceptable β functions in the matching section. Since the triplet is relatively compact, the matching section and D2 dipole can be moved 100 m closer to the IP to shorten the EIR to the required 1400 km. The matching section and DS can then be used to match the Twiss functions and dispersion to the arc. Finally, the BSC of the triplet is computed for the integrated and split configuration and the shielding can be increased or decreased in order to give the right BSC for a 0.2 m β^*. The final design parameters for the integrated triplet after this process are shown in Table 4.3.

Parameter	**Quadrupole**		
	Q1	Q2	Q3
Sub-magnets	2	3	2
Sub-magnet length [m]	15	15	15
Coil radius [mm]	98.3	98.3	98.3
Gradient [Tm^{-1}]	106	110	97
Shielding [mm]	44.2	33.2	24.2

Table 4.3: Design parameters of integrated split triplet.

The matched optics with the ultimate β^* of 0.3 m is shown in Figure 4.6, the figure also shows the orbit of the beam for a crossing angle of 15.5 σ in the horizontal plane. The EIR can also be matched and integrated for when the β^* has been reduced to 0.2 m and 0.15 m with the 15.5 σ crossing angle adjusted accordingly. The BSC for these three configurations is shown in Figure 4.7.

From Figure 4.7, one can see that at $\beta^* = 0.3$ m the BSC is larger than 20 σ and therefore lies well above the allowed minimum of 15.5 σ. The BSC goal is also achieved for $\beta^* = 0.2$ m optics, however, for $\beta^* = 0.15$ m the BSC is slightly lower than 15.5 σ. This is tolerable given that the main purpose of a β^* lower than the ultimate 0.3 m would be to have a handle to increase luminosity if it is lower than

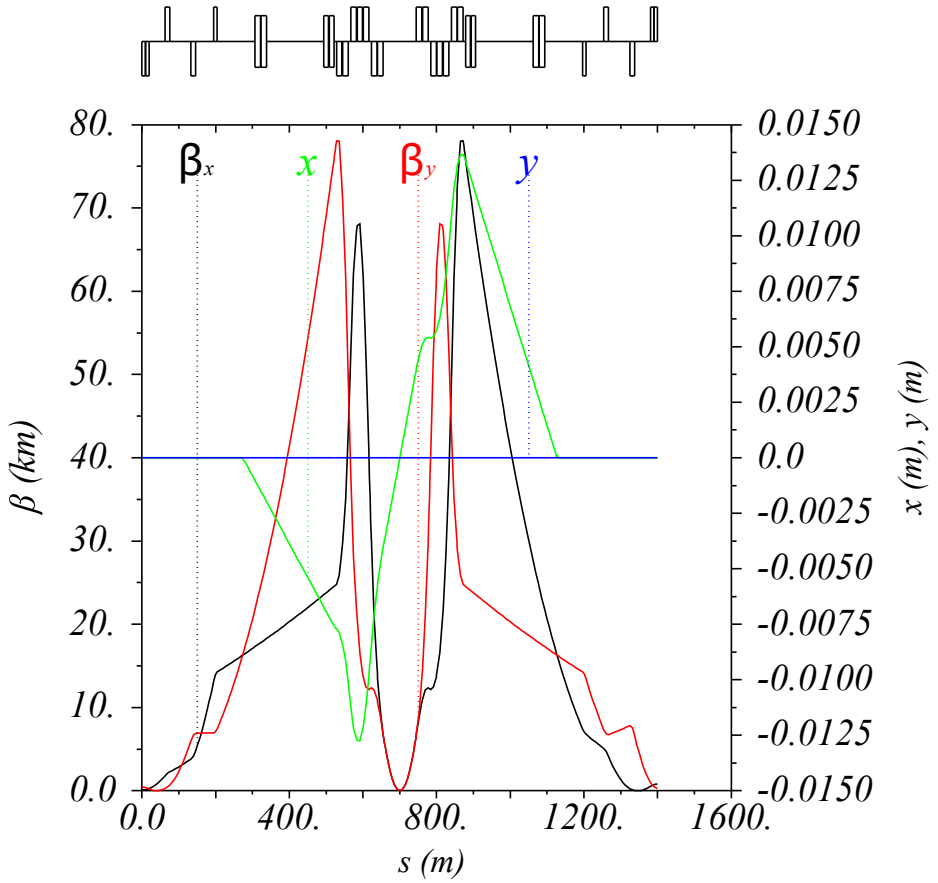

Figure 4.6: β functions and orbit for EIR optics with integrated split triplet.

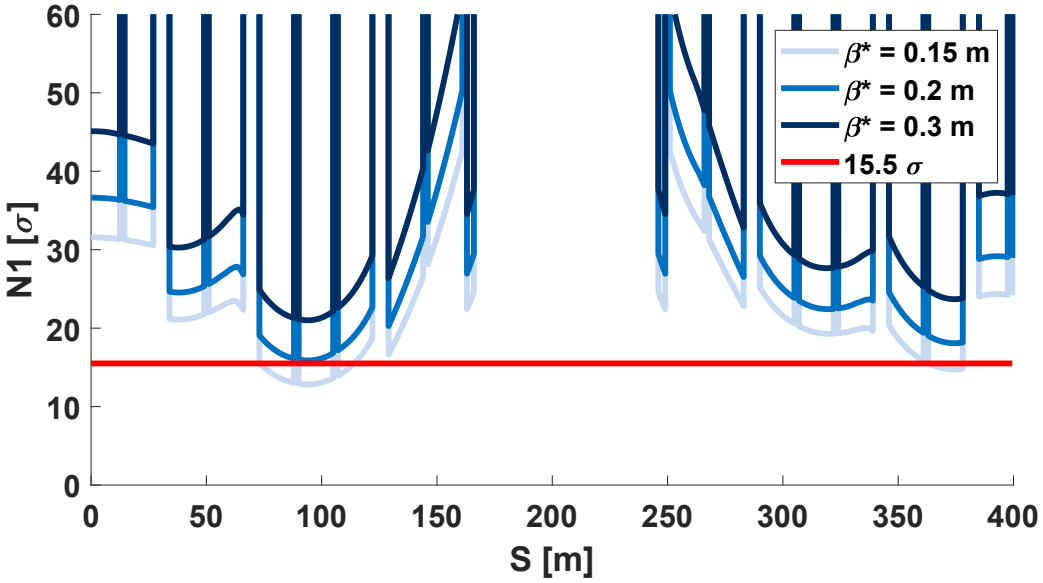

Figure 4.7: BSC for $\beta^* = 0.15$ m, 0.2 m and 0.3 m with integrated split triplet.

expected and one of the main reasons for the luminosity to be lower than expected is a lower beam current than expected. If this is the case then collimation system can probably afford tighter settings which would result in a lower allowed BSC, therefore the $\beta^* = 0.15$ m optics might become a viable in this situation.

4.5 40 m L^* Solution

4.5.1 Motivation

An update of the design of the main detector around the IP reduced the space required for constructing and manoeuvring the detector in the experimental cavern [103]. This gave the opportunity to potentially reduce the L^* from 45 m to 40 m. From Equation 1.45, one can see that the β functions at the entrance of the triplet increase with the square of L^*. Therefore, this reduction of L^* by 10 % could potentially mean a decrease in the triplet β functions by about 20 %.

The reduction in the β functions would decrease the orbit distorting terms given by Equation 1.37 and hence increase the dynamic aperture and make corrections easier. Moreover, the lower β functions would also decrease the natural chromaticity of the synchrotron which would mean that less or weaker sextupoles can be installed in the arcs, which can potentially save a lot of cost and space.

In order to test the effect of the L^* on the chromaticity, the chromatic Montague functions, W, of the synchrotron can be plotted for the three scaled LHC triplet designs presented in [82]. The three triplets have an L^* of 36 m, 45 m and 61 m, and have all been integrated into the same lattice version. The W functions are computed with the arc sextupoles turned off and the results of this study are shown

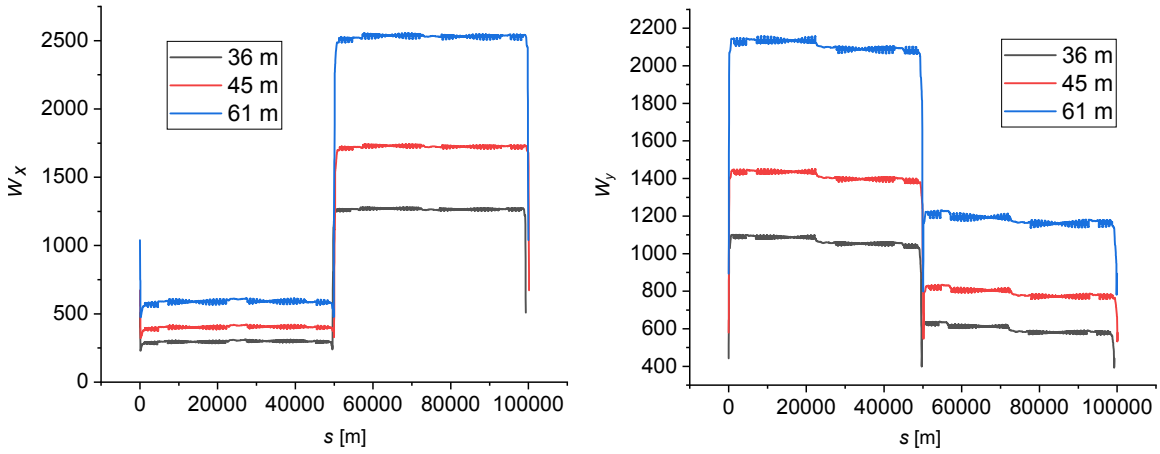

(a) horizontal plane

(b) vertical plane

Figure 4.8: Montague functions for EIR layouts with 36 m, 45 m and 61 m final drifts in the horizontal and vertical planes.

in Figures 4.8a and 4.8b.

As one can see from Figures 4.8a and 4.8b the chromatic effects depend heavily on the L^* as one would expect. For example, the 20 % reduction in L^* from 45 m to 36 m results in a reduction of maximum Montague functions by about 20 % in both planes. Similarly, the increase in L^* by 33 % to 61 m results in an increase of the Montague functions by about 33 %. This provides a good motivation to decrease the L^* to 40 m.

4.5.2 40 m L^* Solution

In order to provide for the 40 m final drift, the triplet found for the 45 m case can be moved 5 m closer to the IP. The correction package and D1 dipole can also be moved by this amount. The new configuration requires the triplet to be slightly re-matched since the focal point in the two planes will have shifted. This re-matching changes the strength of the quadrupoles by up to 2 %. This change is not very significant,

still the apertures can be recalculated and the BSC can be computed again. The parameters of the re-matched triplet are shown in Table 4.4.

Parameter	**Quadrupole**		
	Q1	Q2	Q3
Sub-magnets	2	3	2
Sub-magnet length [m]	15	15	15
Coil radius [mm]	96.5	96.5	96.5
Gradient [Tm^{-1}]	106	112	99
Shielding [mm]	44.2	33.2	24.2

Table 4.4: Design parameters of integrated split triplet at $L^* = 40$ m.

The re-matched optics are shown in Figure 4.9, from which one can see that whilst the maximum β function does not change much, the β functions closer to the IP decrease significantly. The two EIR were integrated into different versions of the lattice at different times, therefore, a plot comparing the Montague functions is not possible. Instead the chromaticity due to the triplet can be worked out using Equation 1.35, which reduces to

$$Q_z = \frac{1}{4\pi} \int_{Triplets} k(s)\beta_z(s)ds, \tag{4.2}$$

since the dispersion is suppressed to zero. Due to the anti-symmetry, it is sufficient to work out this integral over both triplets in one plane, since it will be the same in the other plane. The integral can be evaluated analytically from the strengths of quadrupoles and the Twiss functions at the entrance of the sub-magnets. For the 45 m L^* this integral is 1790 m^{-1}, which reduces by 4.2 % to 1718 m^{-1} for the 40 m L^* as would be expected.

The minimum BSC of the triplet at for the ultimate $\beta^* = 0.3$ m increases slightly

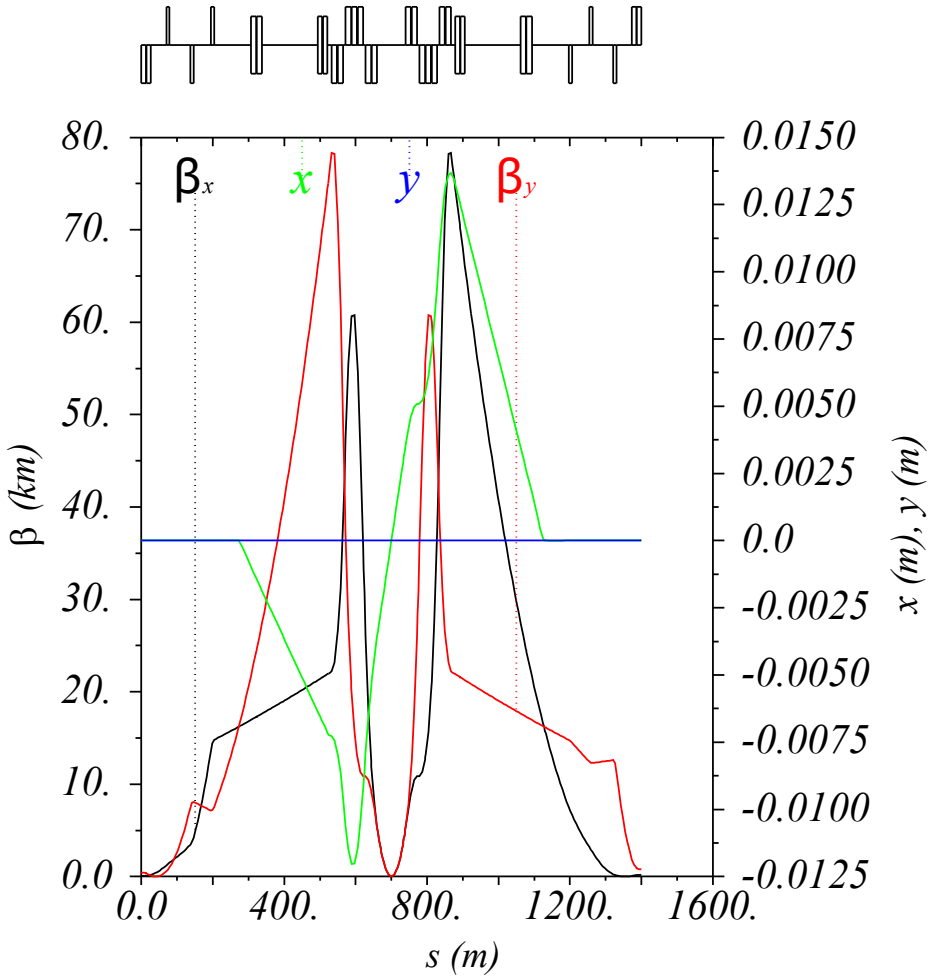

Figure 4.9: β functions and orbit for EIR optics with integrated split triplet at $L^* = 45$ m.

after the shift to the 40 m L^* as seen in Figure 4.10, which shows the BSC for the same three β^* values as for the triplet at the 45 m L^*. This slight increase is most likely due to the smaller orbit in the triplet, which is a direct consequence of moving the triplet closer to the IP. Moreover, as seen from Figure 4.10, the β^* reach improves slightly but remains largely unchanged for this configuration.

Energy deposition studies for this triplet using the FLUKA mode have been performed and the peak dose for an integrated luminosity of 10 ab^{-1} for a vertical and horizontal crossing angle are shown in Figure 4.11 [101]. The peak dose can be fur-

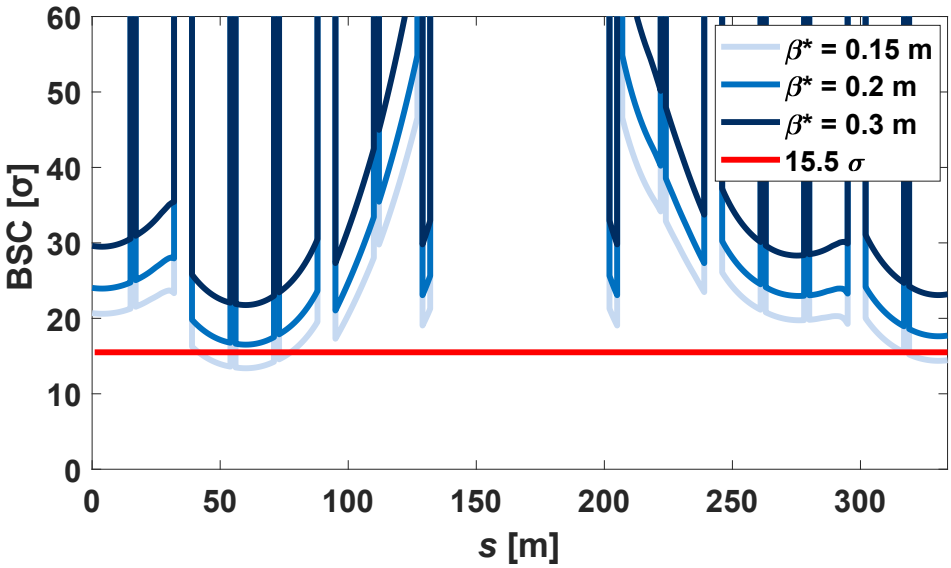

Figure 4.10: BSC for $\beta^* = 0.15$ m, 0.2 m and 0.3 m with integrated split triplet at $L^* = 40$ m.

ther reduced by implementing a scheme where the crossing happens in the horizontal plane for half the fills and in the vertical plane for the other half — this can reduce the largest peak dose to 15 MGy. The FCC-hh aims to achieve an integrated lifetime luminosity of 30 ab^{-1}, this would result in a maximum peak dose of 45 MGy, which is close to the lower bound of the acceptable peak dose of 30-100 MGy.

4.5.3 Flat Beam Alternative

The round β^* optics for the ultimate luminosity goal in the FCC-hh depend heavily on the crab cavity technology. This technology has thus far only been used in collisions for electron colliders and feasibility for high energy proton colliders will not be known until they have been installed and tested in the HL-LHC upgrade [104]. In the event of crab cavities not being able to perform as expected, the peak luminosity would decrease as described by the reduction factor R_L from Equation 1.43. In the case of

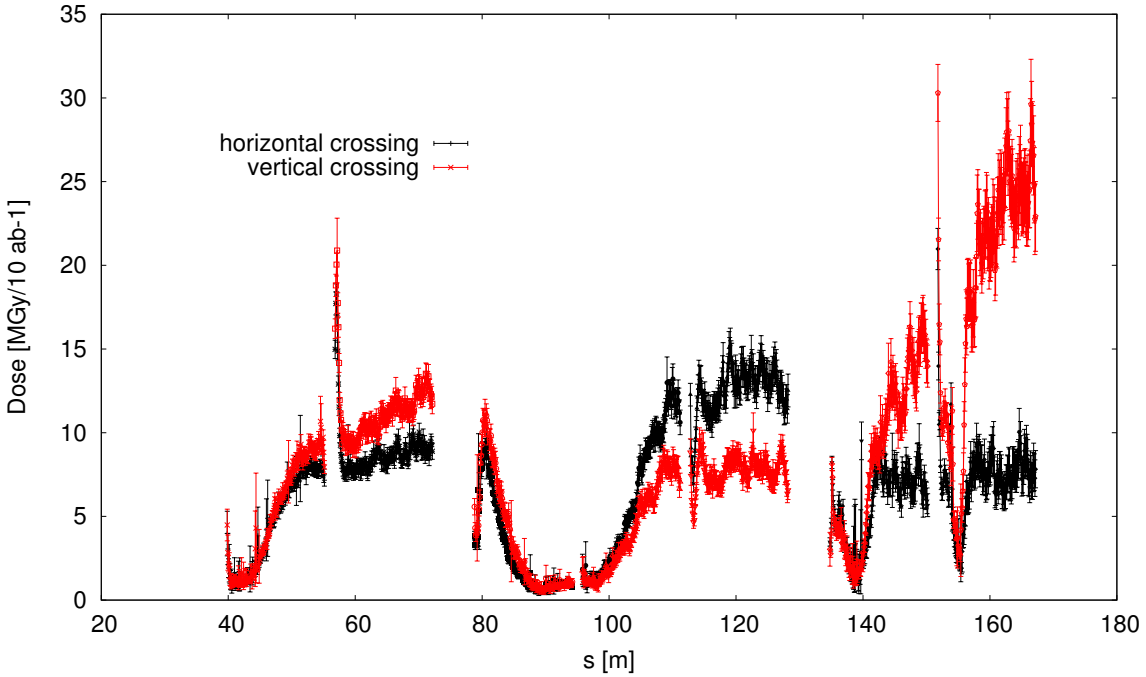

Figure 4.11: Peak dose profile for the round optics.

Source: [101]

the FCC-hh, this would result in a decrease in the integrated luminosity of around 30 % [101].

This reduction can be countered by designing an optics with a lower R_L, such an optics would need a low crossing angle, θ, and a large beam size, σ_z, in the crossing plane. The crossing angle is proportional to ${\beta^*}^{-\frac{1}{2}}$ and the beam size is proportional to ${\beta^*}^{\frac{1}{2}}$, so one has to increase β^* in the crossing plane. At the same time one would want to avoid decreasing the ideal luminosity given by Equation 1.42. The ideal luminosity is proportional to $(\sigma_x\sigma_y)^{-1}$, therefore, when the β^* is increased in the crossing plane it has to be decreased in the other plane. This results in a so called flat optics where the β^* in the crossing plane is larger than the β^* in the non-crossing plane. The ratio between the β^* is referred to as the flat beam factor.

One consequence of having different β^* is that it results in a different beam-beam tune shift in the two planes. In order to keep this effect low, the crossing angle in terms of $\sigma_{z'}$ has to be increased [105]. An extensive study of the integrated luminosity evolution for beams with different flat beam factors was performed and it was found that the loss in integrated luminosity could be reduced to less than 20 % by using a flat beam configuration with $\beta^* = 1.2$ m in the crossing plane and $\beta^* = 0.15$ m in the non-crossing plane [101].

The optics with these parameters can be matched with the alternative triplet. This is done for both a horizontal and vertical crossing plane so that the crossing plane can be altered between the two high luminosity EIRs and between different runs to reduce the peak radiation dose. The optics with the crossing in the horizontal plane is shown in Figure 4.12. Since, the β functions in the triplet depend on $1/\beta^*$, the β functions in the crossing plane are a lot smaller than in the other plane. The crossing angle used for this optics is 114 µrad, which is equivalent to 19.5 σ.

Whilst a β^* of 0.15 m resulted in a BSC below 15.5 σ for round optics, the low β^* is not an issue in the flat case because the orbit bump due to the crossing angle is in the other plane. Moreover, since the absolute crossing angle is 35 % lower than in the round case, the orbit bump in the triplet is also 35 % lower in the the flat optics. This leads to a relatively large BSC as shown in Figure 4.13. The BSC for the flat beam optics is slightly larger than that of the 0.3 m round optics, showing that there is room to squeeze the β^* in the non-crossing plane further to increase the luminosity if needed. Moreover, there is a lot of margin to increase the crossing angle further should beam-beam studies find that the separation has to be increased.

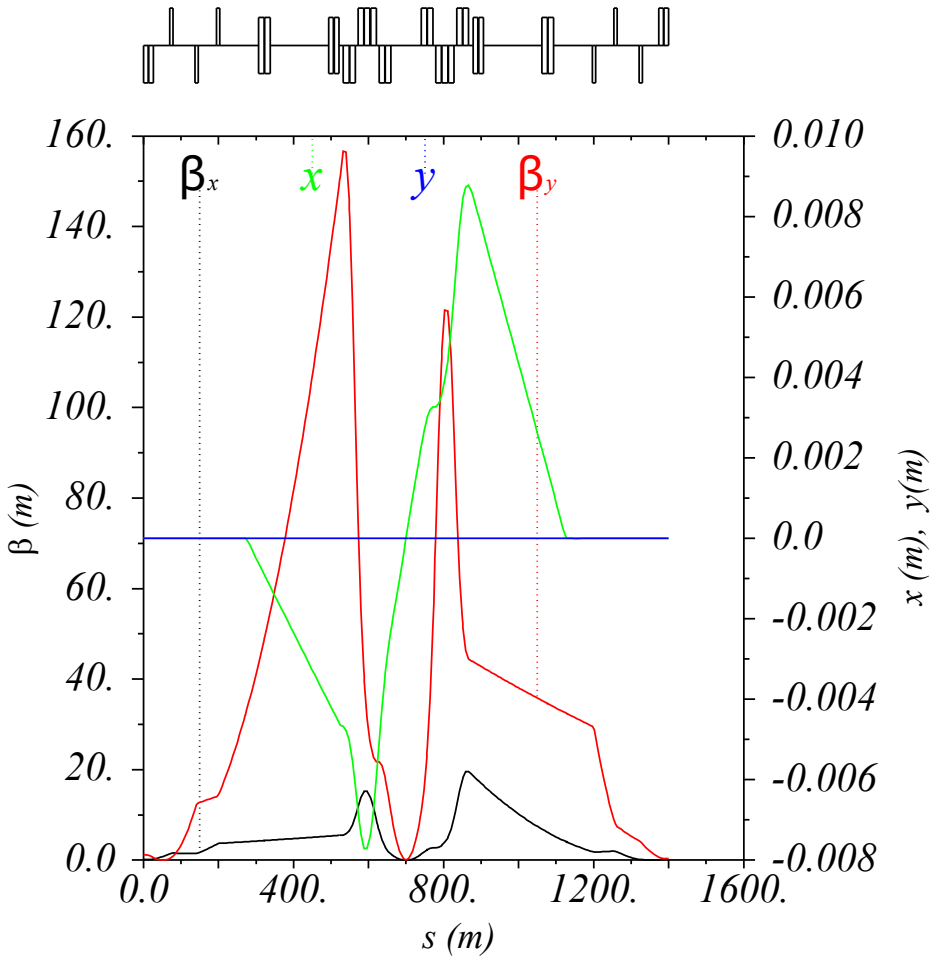

Figure 4.12: β functions and orbit for 1.2 $\times$ 0.15m flat optics with optimised split triplet and 40 m L^*.

The matched optics can also be used for energy deposition studies. Since the optics were matched for crossing in both planes the peak dose can be calculated for scenarios where the crossing is in the horizontal and vertical planes [101]. The results of this study are shown in Figure 4.14, from which one can see that the peak radiation dose is largely not affected by the change to the flat optics. Again, the peak dose could be reduced to 15 MGy/10ab^{-1} by alternating the crossing plane.

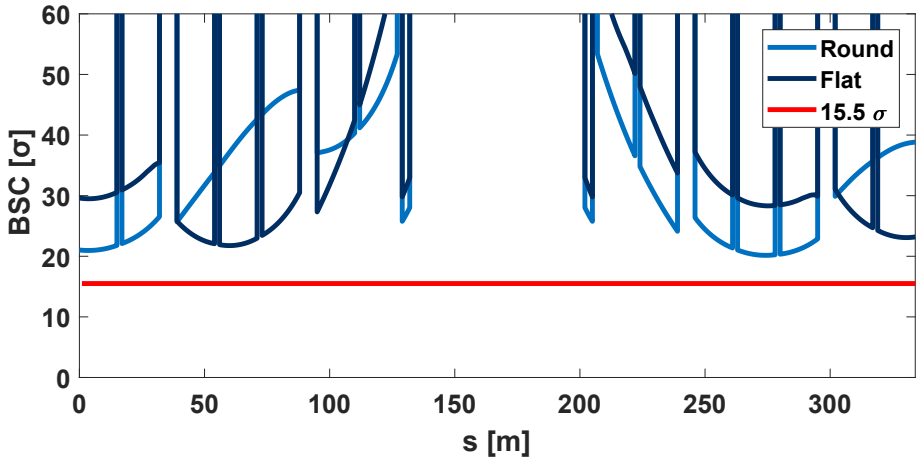

Figure 4.13: BSC for round $\beta^* = 0.3$ m and flat 1.2×0.15m optics with integrated split triplet at $L^* = 40$ m.

4.5.4 Injection Optics

For completeness, the EIR also has to be matched with an optics that gives sufficient BSC at injection. There are currently various injection scenarios for the FCC-hh, the scenario with the lowest injection energy aims to inject 1.3 TeV protons from a superconducting SPS. Since the normalised emittance is conserved, the emittance is significantly larger at injection energy than at the collision energy of 50 TeV. This results in much larger beam sizes for the same β functions. A special injection optics has to be designed to ensure the BSC is large enough at injection.

These injection optics require a large β^* so that the β functions in the triplet remain small enough to provide enough BSC. The beams would be injected with these optics and then accelerated to collision energy whilst keeping the normalised magnet strengths constant, before slowly changing the optics to squeeze the β^* values for collisions. Since the normalised strength of the triplet magnets remains unchanged the injection optics have to be achieved using the strength constraints for the matching

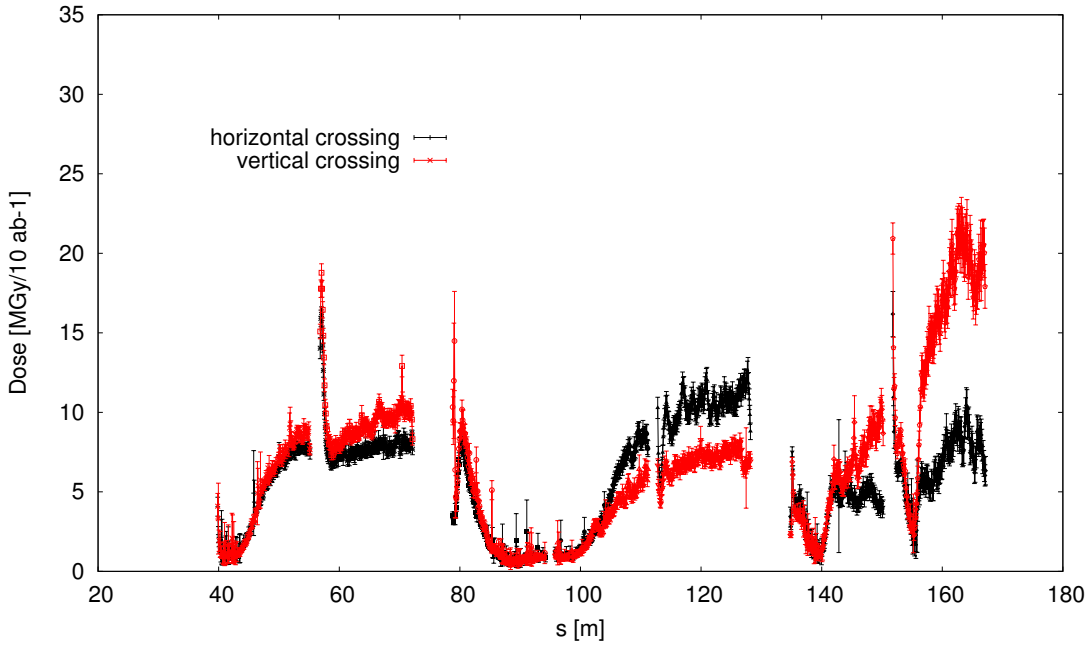

Figure 4.14: Peak dose profile in MGy per 10 ab^{-1} in the optimised split triplet, for the flat optics.

Source: [101]

and DS quadrupoles at collision energy. For the alternative triplet presented in this thesis an injection optics was matched with $\beta^* = 6$ m in both planes. The β functions for these injection optics are shown in Figure 4.15.

The BSC for this optics can also be computed using MADX, for this computation an orbit bump for a 15.5 σ separation was matched and turned on since the beams are not collided in these optics. The resulting BSC plot is shown in Figure 4.16, from which one can see that the BSC is above 20 σ for these optics. This BSC is more than sufficient but it could be increased further by increasing the the β^* even more. This is not done in this case as the resulting optics would deviate more from the collision optics making the squeezing process more complicated and time consuming as well as making it harder to maintain a constant phase advance between injection

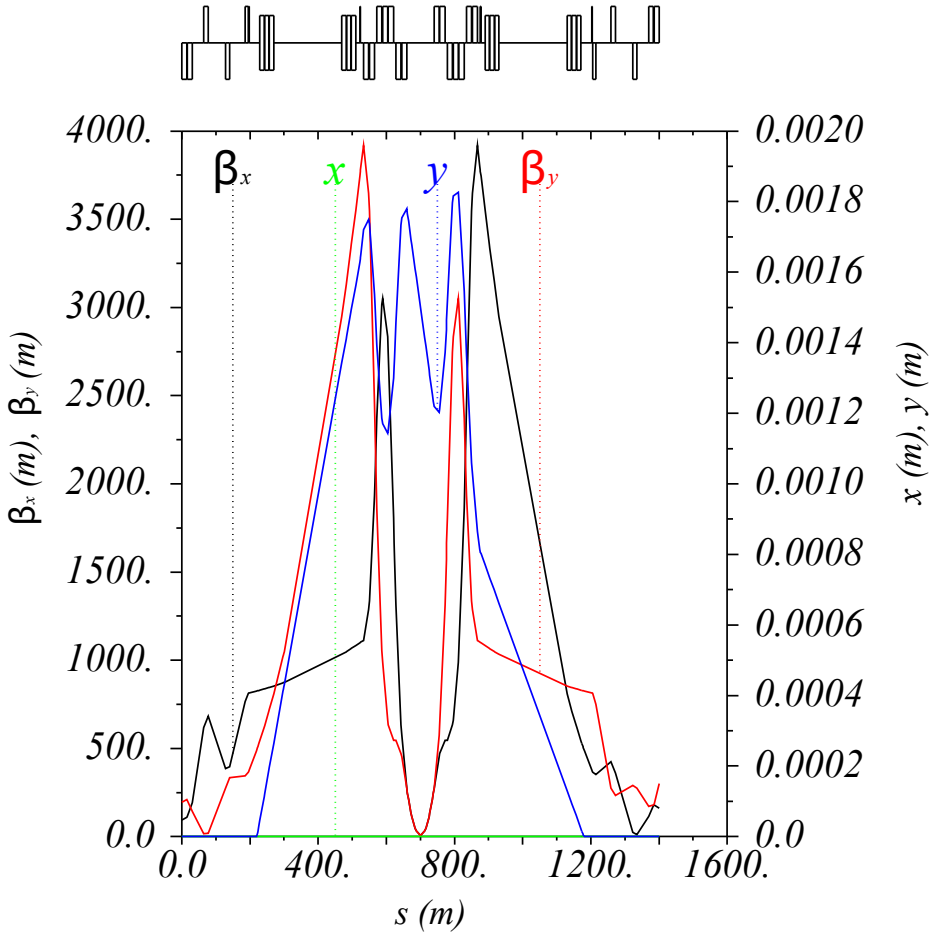

Figure 4.15: FCC-hh injection optics with $\beta^* = 6$ m in both planes and 15.5 σ vertical separation bump.

and collision optics.

4.6 Comparison to Baseline

The final design of the alternative triplet can be directly compared to the final version of the baseline triplet that was designed and modified in parallel and also moved to an L^* of 40 m [106]. The optics of this baseline design are shown in Figure 4.17 and the design parameters of the individual quadrupoles are presented in Table 4.5

As one can see from the from Figure 4.17, the peak β functions in the baseline triplet are about 70 km in both plane. The fact that they are equal is a direct result

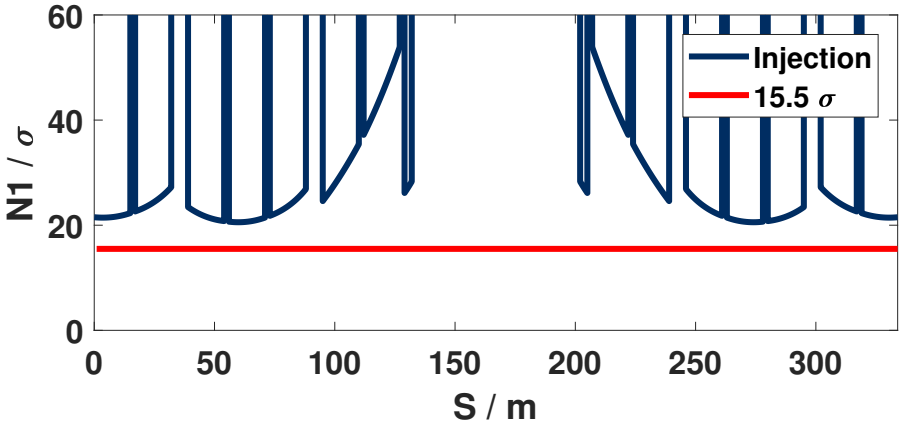

Figure 4.16: BSC for optimised triplet with 1.3 TeV beam energy and $\beta^* = 6$ m injection optics.

Parameter	**Quadrupole**		
	Q1	Q2	Q3
Sub-magnets	2	4	2
Sub-magnet length [m]	14.3	12.5	14.3
Coil radius [mm]	82	105	105
Gradient [Tm^{-1}]	130	105	105

Table 4.5: Properties of quadrupole groups in 40 m L^* baseline triplet.

from the triplet being scaled from the LHC triplet design — the LHC triplet was designed to have equal maximum β functions in order to have the maximum aperture in a uniform beam pipe and can be seen in Figure 2.1.3. The fact that the peak β functions are not equal in the optimised triplet is a result from the optimisation taking into account the varying shielding as well as the fact that all quadrupoles have the same gradient. Therefore, it can be argued that the alternative triplet is optimised more for this experiment.

The magnetic length of the alternative triplet 105 m which is 2.5 m shorter than the baseline triplet, because the baseline triplet requires one split more than the alternative triplet the extra drift means the overall length of the baseline triplet is

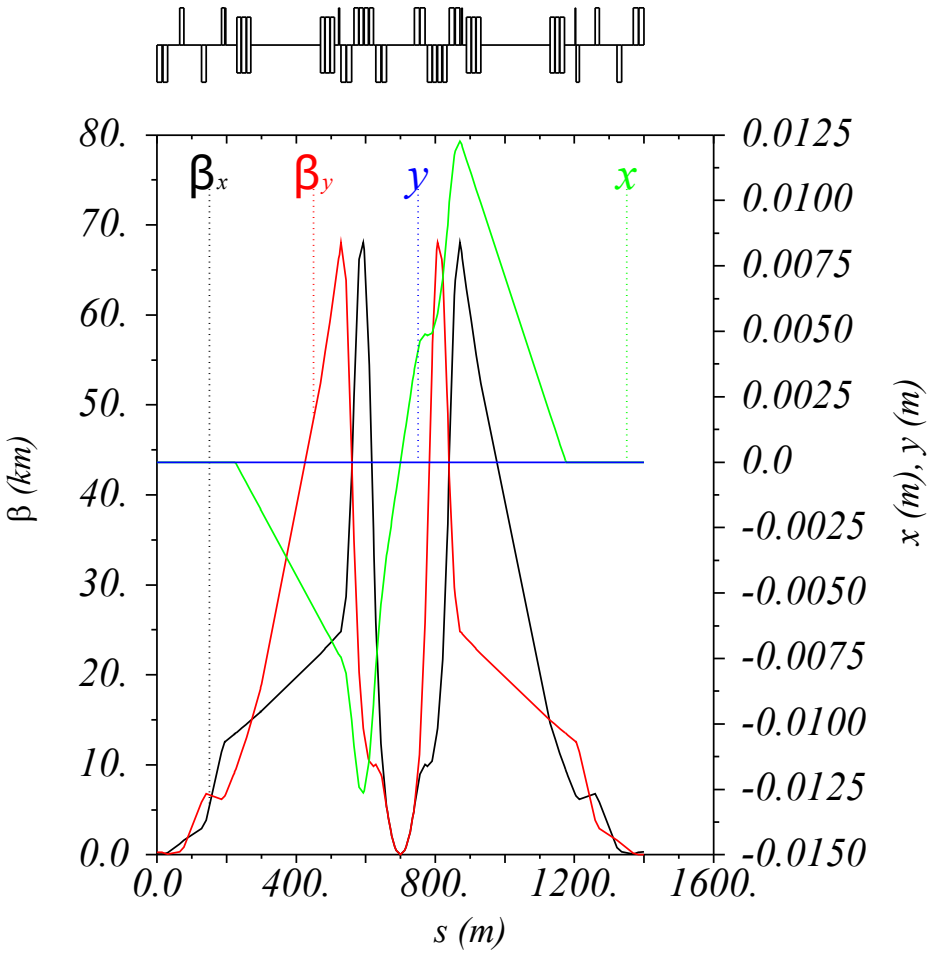

Figure 4.17: β functions and orbit for EIR optics with baseline triplet at $L^* = 40$ m and 15.5 σ horizontal crossing angle bump.

4.5 m longer than the alternative. The biggest benefit of the alternative triplet is that it was designed so that it can be made of a single magnet family, whilst from Table 4.5 one can see that the baseline triplet needs three different quadrupole families with two different lengths and two different coil apertures.

The fact that only one family is needed means that it is less complex to design the different magnets and easier to manufacture them. Moreover, the triplet requires a smaller pool of backup magnets which is another cost saving factor. Another potential benefit of making the triplet of identical magnets arises from the fact that, as shown

in Figures 4.11 and 4.14, the peak dose is not equal in every magnet. The lifetime of the quadrupoles could be increased by swapping magnets that are in areas with large doses with magnets in areas where the doses are lower. This could be done during the scheduled long shut downs of the FCC-hh.

The baseline triplet comes with two shielding options, the first option considers a uniform 15 mm shielding and has a β^* reach of 0.1 m. The second option, is more comparable to the alternative triplet presented here, uses a uniform 35 mm of shielding and has β^* reach of 0.2 m. The peak lifetime dose deposited in the baseline triplet with the 35 mm shielding is about 75 MGy for a 30 ab^{-1} lifetime, meaning the magnets have a similar lifetime [107].

Both the baseline and alternative triplet EIRs are integrated in the same lattice so the DA of the FCC-hh can be evaluated with either one. For the alternative triplet the DA was computed for the round and flat optics with errors in the arc dipoles as predicted from the magnet team and triplet errors scaled from the errors of the HL-LHC triplet [108]. The DA was computed in Sixtrack for 60 error seeds with and without non-linear correctors as described in Equation 1.37 and the results are shown in Figure 4.18.

Without any correctors, the minimum DA is above 16.4 σ for the round optics and 12.2 σ for the flat optics — in both cases this is slightly higher than the 11.6 σ of the baseline design [109]. When applying non-linear correctors, the DA increases to 25.4 σ and 20.4 σ for the round and flat optics, which is comparable to the 24.6 σ of the baseline. One reason for the slightly larger DA of the alternative triplet could be shorter magnetic length, nevertheless it should be noted that both triplets easily

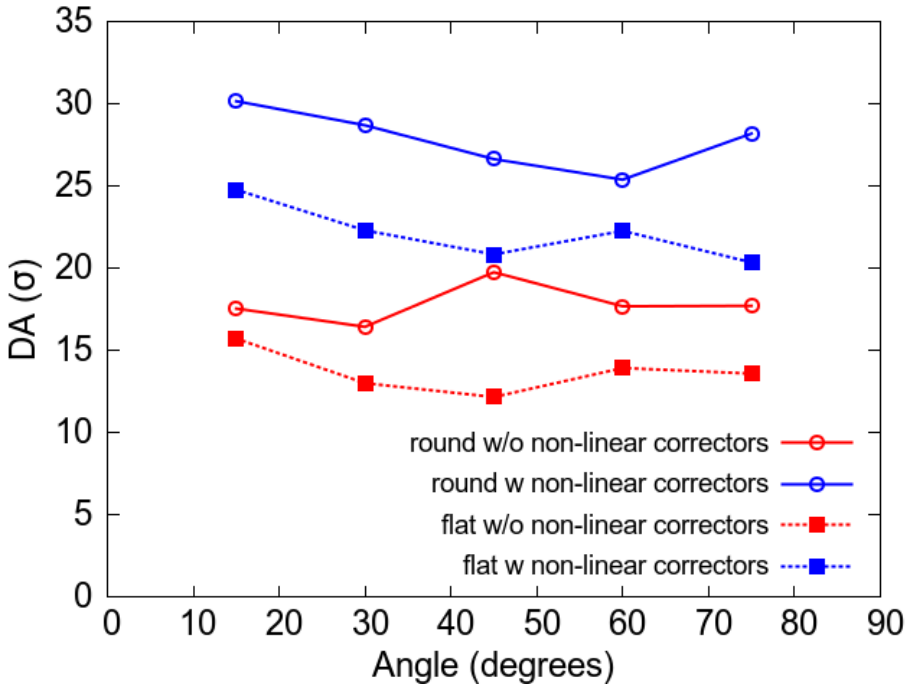

Figure 4.18: Minimum DA for various angles over 60 seeds and errors in the arc and EIRs for alternative round and flat optics with and without non-linear correctors.

Source: [108]

fulfil the design goal of a 10 σ DA.

Overall, the alternative triplet has a very similar performance to the baseline triplet in both energy deposition and DA. The largest benefits of the alternative design is that the triplet is shorter, the individual quadrupoles are made of identical sub-magnets. This work has also shown that it is possible to have a specially designed flat optics that could help recover luminosity if the crab cavities do not work.

4.7 Conclusion and Outlook

This chapter has shown the successful implementation of the Triplet Optimisation Code introduced in Chapter 3 in order to find an optimised triplet for the FCC-hh. During the process it has been shown how findings from energy deposition studies were

used to further constrain the solutions to produce a triplet with a uniform aperture. It has also been shown how results can be interpreted and slightly modified when installing the triplet into the lattice.

The close co-operation with energy deposition studies was a key feature of this process. The flexibility of the algorithm and the speed at which it finds solutions was key in this as it meant many iterations could be made. The final triplet designed for the 40 m L^* configurations is comparable to the baseline option in many respects, however, it has the benefit of being made of seven identical magnets. Moreover, this thesis also shows that a flat optics is viable in FCC-hh EIR, which could be used if crab cavities are not available. This design has to be updated if there are further changes to the design requirements. If the changes are small, like the change in L^*, this can be done without changing the triplet. However, if larger changes are required the optimisation can be redone with the knowledge gained from this iteration as a starting point. This knowledge can also be used when applying these methods to other future accelerators that may face similar challenges.

Chapter 5

HE-LHC Optics

5.1 Introduction

This Chapter will show how the knowledge obtained from the FCC-hh triplet optimisation in Chapter 4 can be applied to the HE-LHC. The HE-LHC triplet faces similar challenges due to the high collision debris and novel technologies. Moreover, the length of the triplet is arguably more crucial as the length of the EIR is fixed by the tunnel layout.

The optimisation will go further and come up with a proposed design for the remaining EIR, including separation dipoles, space for crab cavities and a matching section. This is required since there was no previous dedicated HE-LHC design. The compatibility of the proposed EIR with the rest of the machine is also tested with extensive DA studies at collision. This work also includes implementing a spurious dispersion correction scheme and a redesign of IR4, which contains the RF cavities, to help tune the machine.

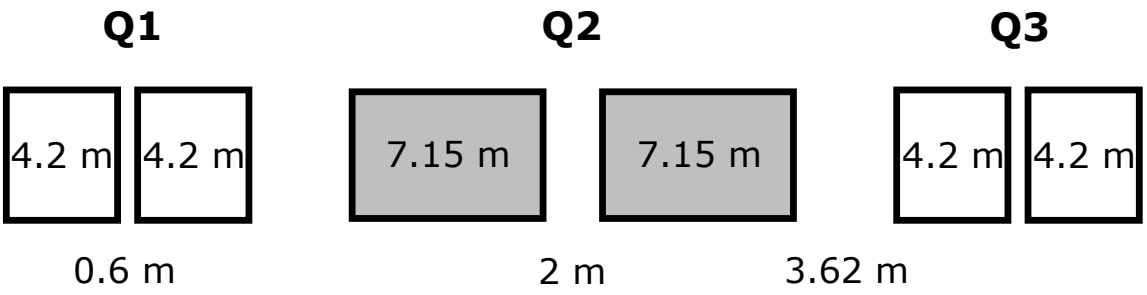

Figure 5.1: Overview of HL-LHC V1.2 Triplet.

5.2 Requirements and Starting Point

The HE-LHC would be constructed in the same tunnel as the LHC and HL-LHC, therefore, the geometry and layout of the HE-LHC has to be very similar to that of the LHC. For this reason, the lattices of the LHC and HL-LHC are a good starting point for the HE-LHC. However, these lattices will have to be heavily modified to include the new arc designs and make the IRs compatible with the increased beam energy and the Nb_3Sn magnet technology.

Whilst the LHC lattice V6.503 is used as the starting point for most of the HE-LHC, the triplet installed in the HL-LHC V1.2 [31] lattice is used as a starting point for the triplet design. This triplet is designed to be made of Nb_3Sn superconducting quadrupoles, which is the same technology intended to be used in the HE-LHC [110]. The triplet has a total length of 41.5 m and all three quadrupoles are 3.62 m apart and are split into two sub-magnets. Q1 and Q3 consists of two 4.2 m sub-magnets with 0.6 m separation whilst Q2 is made of two 7.15 m sub-magnets with a 2 m separation in which BPMs and dipole kickers can be installed. An overview of the triplet is shown in Figure 5.1.

The simplest way to obtain an estimate of the triplet length needed for the HE-LHC is by scaling the HL-LHC triplet with momentum, p. For a fixed magnetic gradient, the normalised strength, k, scales as $1/p$. Hence, in order to keep the same integrated strength kL, the length of the triplet would have to scale with p. This approximation assumes the gradients and subsequently the apertures in the triplet magnet remain the same. This holds if the beam sizes, $\sqrt{\epsilon\beta}$ remain roughly the same. Which is true, since on the one hand a longer triplet results in larger β functions since $\beta \propto L \propto p$ but on the other hand $\epsilon \propto 1/p$ so that. Based on this the HE-LHC triplet would need to be $\frac{13.5 \text{ TeV}}{7 \text{ TeV}} \times 41.5 \text{ m} \approx 80 \text{ m}$ long. This is a substantial increase, considering that the straight section has a length of only 268.9 m from the IP to the DS.

Therefore, the first task for the HE-LHC EIR design is to optimise the triplet in order to keep it as short as possible. Like in the FCC-hh, the optimisation also has to include finding the right amount of shielding since both the energy and the peak luminosity will be much higher than in the HL-LHC. The increased shielding is a factor that was not taken into account in the scaling and could potentially make the triplet even longer.

The triplet then has to be integrated in the lattice. Since there was no HE-LHC EIR design before this thesis, the whole EIR has to be adapted for the optimised triplet and for the other challenges arising from the HE-LHC beam. New separation dipoles are needed to steer the more rigid beams and achieve the increased arc beam separation for the HE-LHC. Moreover, the high collision debris means that the dipoles have to be designed in such a way that enough shielding can be fitted to protect them

sufficiently.

The matching section of the EIR has to be adapted for the HE-LHC, a starting point for this was the HL-LHC lattice version SLHC V6.1a, which is close to the LHC design but already has some space reserved for the crab cavities, which will also be needed for the HE-LHC. Since the magnet technology of the HE-LHC is identical to that of the FCC-hh the matching quadrupoles' gradients must not exceed 360 Tm^{-1}. This may result in changing the length of the matching quadrupoles in order to achieve the desired integrated strengths.

A similar principle applies to the optimisation of the DS, however, the lengths of the quadrupoles have a significant effect on the overall geometry of the ring. Consequently, this optimisation has to be done in close collaboration with the rest of the lattice design team. This collaboration also has to be extended to integrating the EIR into lattices with both the 18 and 23-cell arc options. This integration has to include the implementation of spurious dispersion correction schemes and detailed DA studies.

5.3 Triplet Optimisation

The design constraints used for the HE-LHC triplet optimisation are partly based on the those of the HL-LHC but largely assume FCC-hh technology. The HL-LHC triplet shown in Figure 5.1 uses Nb_3Sn technology, hence its separations between the quadrupoles can be taken as a good estimate for the separations required in the HE-LHC triplet. Since the optimisation code only simulates three quadrupoles the various separations can be absorbed into two separations of 5.22 m between the

three main quadrupoles. Apart from this, FCC-hh constraints were assumed, so that the same magnet model as for the FCC-hh was used with the coil radius varying in a power law as stated in Equation 4.1. Moreover, the different magnet and beam screen components as described in Table 4.2 were subtracted from the coil radius to work out the beam screen radius.

Since the HE-LHC plans to use the same injector chain as the HL-LHC, the aperture was computed in MADX using the HL-LHC beam parameters with a normalised emittance of 2.5 μrad, a momentum spread, $\frac{\Delta p}{p}$, of 2×10^{-4}, a closed orbit tolerance of 2 mm and a beam halo of 6 σ. The fractional parasitic dispersion was set to 0.1 in both planes and β beating of 20 % was used. Based on the findings for the FCC-hh in Chapter 4 it was decided to constrain the quadrupoles to have a uniform coil aperture in order to have a more even distribution in debris.

At the start of the design process the HE-LHC required a β^* of 0.25 m, therefore, this was used for the optimisation. The minimum BSC in the code was set to 18.75 σ to accommodate two beams with 12.5 σ BSC each and a crossing angle of 12.5 σ [111, pp. 29–35]. The initial guess for the sufficient amount of shielding was a uniform 10 mm shielding [112]. The triplet optimisation was done together with the energy deposition in the same way as for the FCC-hh. The energy deposition studies were done using a modified version of the FLUKA model used in the FCC-hh optimisation [113].

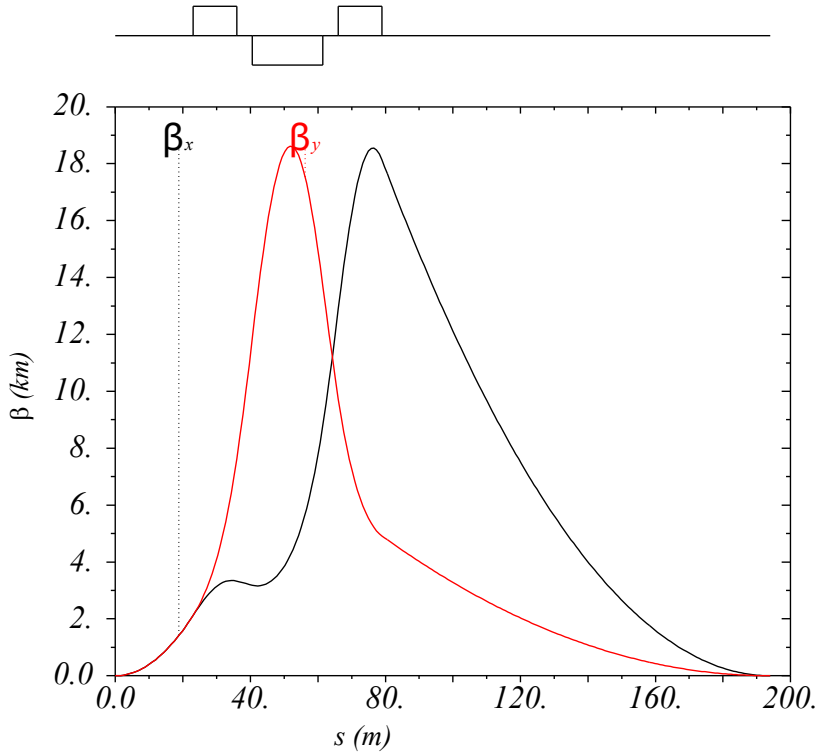

Figure 5.2: Optics result from Triplet Optimisation Code for HE-LHC.

5.3.1 Solution and Integration

The triplet found at the end of the optimisation process was found with a uniform shielding of 20 mm. The triplet has a total length of 56 m which is only 35 % longer than the HL-LHC triplet and therefore much better than expected. The solution is shown in Figure 5.2, the lengths of Q1 and Q3 are 12.9 m and Q2 is 20.9 m long. This means that the total magnetic length of the triplet only increases by 50 % compared to HL-LHC. It should also be noted that the maximum β functions in both planes are almost equal, this is probably a result of the shielding being uniform during the optimisation.

Whilst for the HL-LHC Q1 and Q3 were split for manufacturing reasons this is not done for the HE-LHC triplet since the magnet specifications are assumed to be

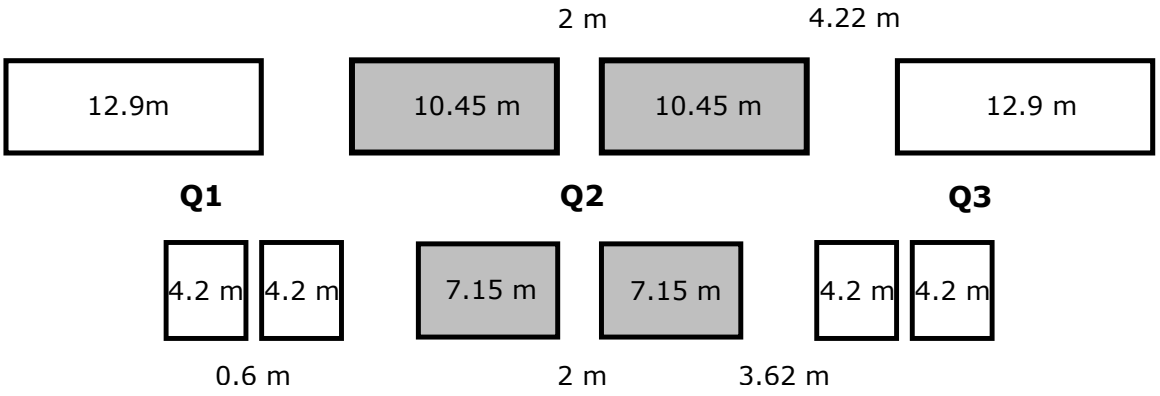

Figure 5.3: Optimised HE-LHC triplet (top) in comparison with HL-LHC triplet (bottom).

the same as for FCC-hh, which requires a maximum length of 15 m. At the same time, Q2 has to be split into two 10.45 m sub-magnets separated by 2 m to allow for instrumentation like in the HL-LHC. The 0.6 m separation between the sub-magnets of Q1 and Q3 in the HL-LHC are absorbed into the drifts between the main quadrupoles as a safety margin, resulting in a total separation of 4.22 m. A layout of the integrated HE-LHC triplet is shown in Figure 5.3, for reference it is shown next to the layout of the HL-LHC triplet drawn to scale.

The realistic triplet is integrated into the SLHC V6.1a EIR lattice, using macros that are defined in the original lattice file, to help remove the LHC triplet from the LHC lattice and replace it by a user specified triplet. The macros also allow the user to specify the location of the separation dipoles and matching quadrupoles, however, these locations are left unchanged in order to ensure there is enough room between the D2 and the matching quadrupoles to fit the crab cavities.

Using this setup the triplet was re-matched so that the β functions in both planes are low enough in the matching section for a $\beta^* = 0.25$ m optics. The β, α and

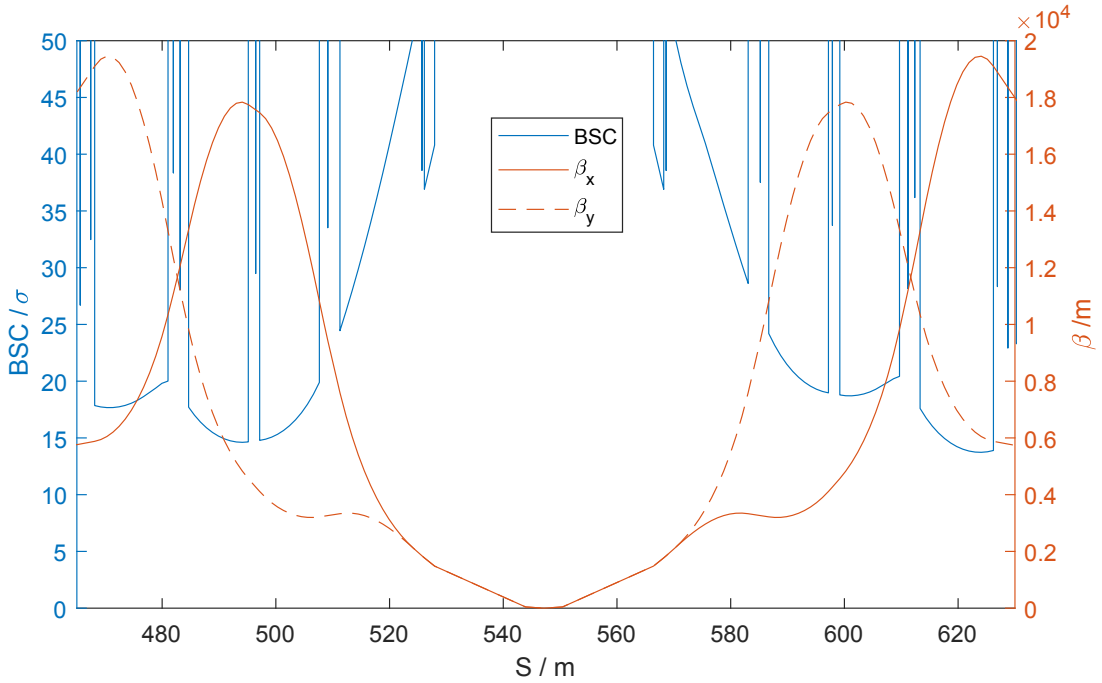

Figure 5.4: β functions and BSC for HE-LHC triplet at a β^* of 0.25 m and a crossing angle of 12.5 σ.

dispersion functions were then matched to the arc, before matching the 12.5 σ crossing angle, this corresponds to an absolute half crossing angle of 135 µrad. The coil apertures were calculated using the gradient of the strongest triplet quadrupole and set to be constant throughout the triplet, the properties of the sub-magnets are shown in Table 5.1. Next the BSC was computed using the MADX aperture module and the resulting β functions and BSC in the triplet are shown in Figure 5.4.

Parameter	**Quadrupole**		
	Q1	Q2	Q3
Sub-Magnets	1	2	1
Sub Magnet Length [m]	12.9	10.5	12.9
Coil Radius [mm]	70.4	70.4	70.4
Gradient [Tm^{-1}]	145	146	145
Shielding [mm]	20	20	20

Table 5.1: Properties of quadrupoles in the HE-LHC triplet.

As seen in Figure 5.4, the re-matching of the triplet resulted in the first β function peak to be slightly reduced. The minimum BSC in the triplet is about 14 σ, which gives a very low margin to further decrease the β^*. At the same time, the BSC in the Q1 magnet is above 24 σ meaning that more shielding could be fitted into this quadrupole if needed. A final point to note is that from Table 5.1, we can see that the fields of the quadrupoles are much larger than the ones in the FCC-hh triplet, this is mainly due to the fact that much less shielding is needed and hence the coils can be tighter.

5.3.2 β^* and Crossing Angle Change

During the design process, the β^* was changed from 0.25 m to 0.45 m to provide for a slower burn off and a more even luminosity evolution [60]. This reduces $\sigma_{z'}$ at the IP significantly, so that a separation of 12.5 is achieved with a half crossing crossing angle of 135 µrad. However, the half crossing angle was was kept at 165 µrad due to beam-beam considerations [114]. In terms of beam size, this results in a crossing angle of 16.785 σ. An advantage of the fact that the magnitude of change in the half crossing angle is the same as that for $\sqrt{\beta^*}$, is that the voltage required in the crab cavities remains unchanged.

Since the increase in β^* means that the β functions in the triplet will decrease, the 0.45 m optics can be achieved with the optimised triplet. The optics can be changed by adjusting the matching section whilst leaving the triplet unchanged. An advantage of using the same triplet for the 0.45 m optics instead of optimising it again is that it will provide more margin for β^* reduction if needed since it has been demonstrated

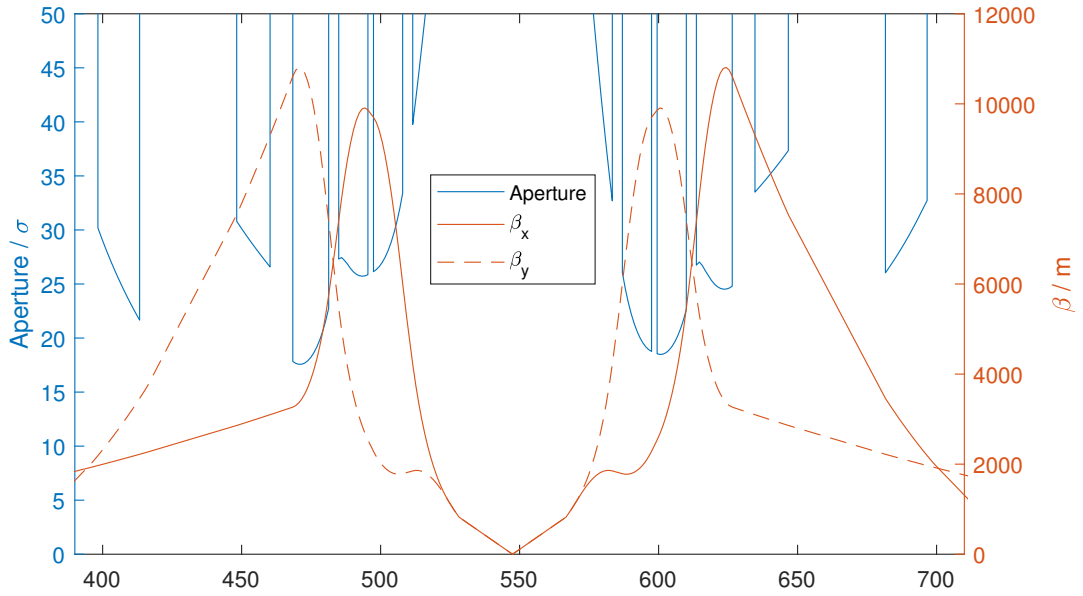

Figure 5.5: β functions and BSC for HE-LHC triplet at a β^* of 0.45 m and a crossing angle of 16.785 σ.

to leave enough BSC for a β^* of 0.25 m. This provides a good margin to increase the luminosity if needed, in a similar way as was done for the FCC-hh.

The β functions and BSC for the optics with the 0.45 m β^* are shown in Figure 5.5. The BSC shown is calculated for a scenario with the crossing angle in the vertical plane. The fact that the crossing angle is relatively large results in a significant reduction in BSC when the β functions in the vertical plane are large. This effect is especially dramatic in Q3 in the left triplet about 460 m in Figure 5.5, where the BSC reaches its minimum at about 18 σ. Since the orbit is still relatively small in Q1 the aperture in this quadrupole is larger than 30 σ meaning that more shielding can be installed in Q1 if needed. Figure 5.5 also shows the BSC in the separation dipoles without any shielding, the apertures of these magnets will be explored further in section 5.4.

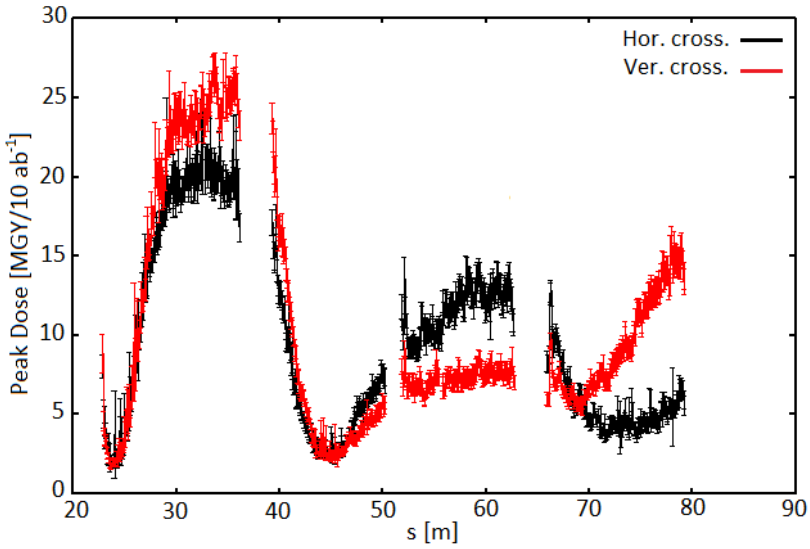

Figure 5.6: Energy deposition in HE-LHC triplet.

Source: [113]

Energy deposition studies of this triplet show that for both vertical and horizontal crossing the shielding is sufficient to keep the total dose below 25 MGy for an integrated luminosity of 10 ab^{-1} [113], which is roughly equal to the expected integrated luminosity of the HE-LHC [32]. This means that the triplet radiation dose stays safely below the 30 MGy lower limit. The energy deposition is shown in Figure 5.6, from which one can see that the largest dose is in Q1 — increasing the shielding in this quadrupole could potentially reduce the radiation dose even further to keep it below 15 MGy throughout. Currently, this is not needed but it is a viable option should the expected lifetime luminosity increase.

5.4 Separation Dipoles

5.4.1 Requirements

The separation between the two rotating beams is 194 mm in the (HL-)LHC arcs [115], the magnet design in the HE-LHC requires this separation to be increased to 250 mm in order to use larger arc dipole coils [111, p. 59]. On top of achieving this larger separation, the HE-LHC separation dipoles also need to be strong enough to do this at the high beam rigidity. Moreover, D1 has to be moved further away from the IP than in the (HL-)LHC to make room for the longer triplet. Since moving D2 further back is not possible as it would reduce the space for the crab cavities and matching section, the separation has to be achieved over a shorter space.

These challenges can be met by using stronger superconducting dipoles, however, the strength of these dipoles is limited by their aperture. The apertures have to be large enough to give enough BSC to the two beams but also leave some room for shielding. The strength of D1 is limited by the high amount of magnetic flux that arises due to the large aperture and has to be returned [116]. Similarly, the field in the D2 magnet is limited by the flux density in the separation yoke [117]. This flux is a lot higher than in the arc dipoles because the dipole fields in both apertures have the same orientation.

The simplest way to reduce the field of the dipoles is to increase their length, however, since the space for the crab cavities and triplet have to stay fixed, this can only be done by reducing the drift space between the two dipoles. Furthermore, the longer the separation dipoles are, the more the curved paths of the beam deviate from

the centre of the dipole, reducing the BSC.

Therefore, a careful optics study is needed to explore all separation dipole options and find the one that best fulfils the requirements outlined above. In order to ensure the magnets are realistic, this has to be done together with the HE-LHC magnet design team. Further energy deposition studies are needed to ensure the magnets have enough aperture to install shielding to protect them from the radiation. The options also need to consider the placement of a target absorber neutral (TAN) between D1 and D2 to protect D2 and all the following magnets from neutrons.

5.4.2 Solutions

The HL-LHC design includes plans for replacing the LHC's warm separation dipoles with a pair of superconducting NbTi dipoles. In this configuration D1 is 6.25 m long and has a field of 5.6 T and D2 has a length of 7.8 m and a field of 4.5 T. The first scenario explored for the HE-LHC is one with the dipole lengths remain unchanged, in this case the HE-LHC would require fields of 18.6 T and 14.8 T, which is more than 200 % larger than in the HL-LHC and therefore unrealistic. On the other hand, to maintain the strengths of the HL-LHC it would require a D1 magnet made of two 10 m sub-magnets and a D2 magnet made of two 12.5 m sub-magnets, however, this would only achieve the necessary separation if the crab cavities were removed and D2 moved next to Q4. Both these options are shown in Table 5.2.

With these two extremes in mind and after consulting with the magnet design team a more realistic set up can use a 12 m D1 dipole together with a 15 m D2 with fields of 9.7 T and 7.7 m respectively, this is also shown in Table 5.2. This

configuration would not decrease the space available for the crab cavities and ensures that D2 does not have to be split. Moreover, the fields are slightly more than 70 % larger than those in the HL-LHC. In this configuration D1 has a coil radius of 80 mm each aperture in D2 can have a coil radius of 38.5 mm.

Configuration		Length [m]	Field [T]	Increase in Field [%]
HL-LHC	D1	6.25	5.6	-
	D2	7.8	4.5	-
HL-LHC length	D1	6.25	18.6	+230
	D2	7.8	14.8	+200
HL-LHC strength	D1	2×10	5.8	+3
	D2	2×12.5	4.6	+3
HE-LHC	D1	12	9.7	+73
	D2	15	7.7	+71

Table 5.2: Different separation dipole options in the HL-LHC and HE-LHC.

After including the space needed for the beam screen and magnetic components, it was found that D1 has a similar BSC to the triplet if it has a shielding of 21.5 mm, which is slightly larger than the shielding in the triplet and therefore provides similar protection. With this shielding the radiation dose is kept below 20 MGy [118] as shown in Figure 5.7a.

The apertures of the two beams in D2 have to be in parallel for manufacturing reasons. At the same time, the two beams travel through the dipoles at an angle which reduces the BSC and only allows for a uniform 9 mm shielding. This relatively low shielding results in a high integrated peak dose of almost 100 MGy, as shown in Figure 5.7b.

The beam envelopes in the horizontal and vertical planes are plotted in Figures 5.8a and 5.8b. The tungsten shielding shown in Figure 5.8a is not arranged

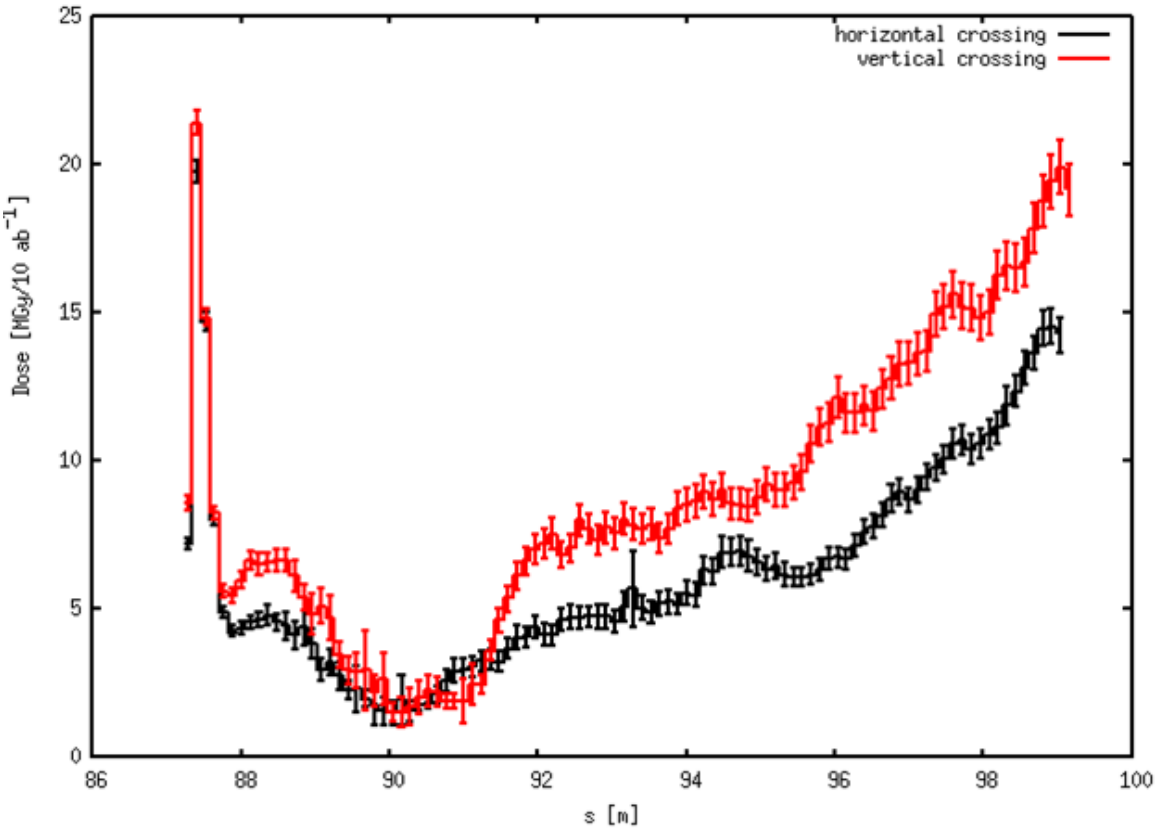

(a) D1

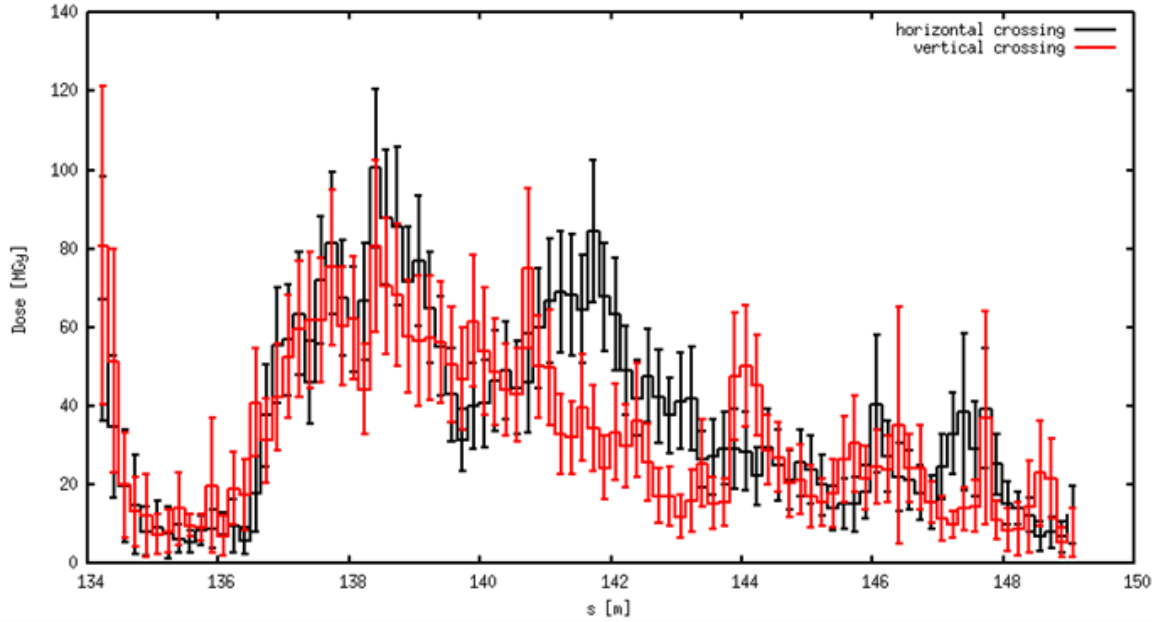

(b) D2

Figure 5.7: Energy deposition in separation dipoles for 10 ab^{-1} integrated luminosity.

Source: [118]

in a uniform distribution but in a way so that it is equidistant from the beam. Whilst a uniform shielding would only be allowed to have a thickness of 9 mm, this varied shielding can have a thickness between 9 mm and 27 mm. At the entrance of the magnet this results in less shielding on the inside, however, this section of the dipole is in the shadow of the TAN so this should be tolerable. At the other end, the shielding is thicker on the inside which protects the dipole from lower momentum debris being steered into the dipole. This type of shielding can reduce the peak dose from 100 MGy to 40 MGy for an integrated luminosity of 10 ab^{-1} [118].

5.4.3 Crab Cavities

The crab cavities are located between D2 and Q4, where about 20 m are reserved for them and further beam instrumentation [104]. The crab cavity voltage is given by Equation 1.44, but for low β^* and θ it can be simplified to

$$V_c = \frac{cE_b\frac{\theta}{2}}{\pi f\sqrt{\beta^*\beta_{crab}}}, \tag{5.1}$$

where β_{crab} is the β function in the crab cavities, which is of the order of 1500 m in these optics. Assuming a cavity frequency of 400 MHz this results in a crabbing voltage of 10 MV per side. The HL-LHC aims to supply 6.8 MV either side of the IP using two cavities housed together in a 6.6 m cryostat [104]. The 10 MV could therefore be achieved with three such cavities per beam either side of the IP, taking up about 10 m and leaving enough space for interconnects, instrumentation and other components.

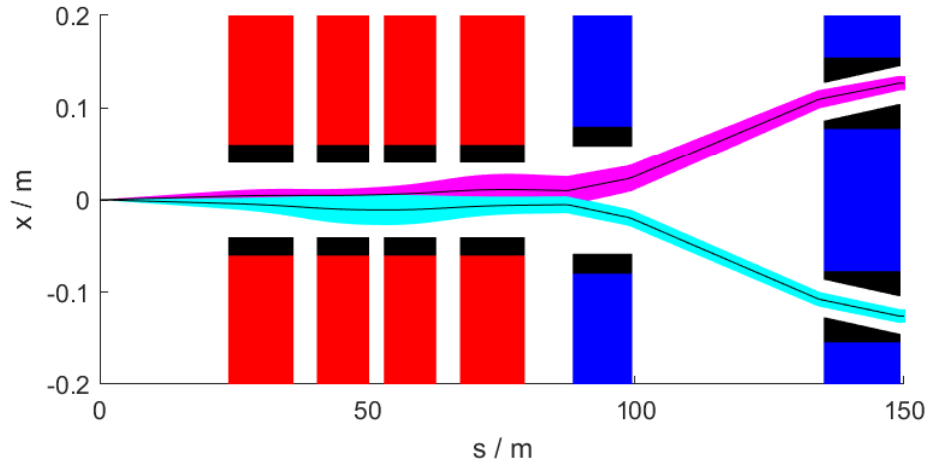

(a) Horizontal

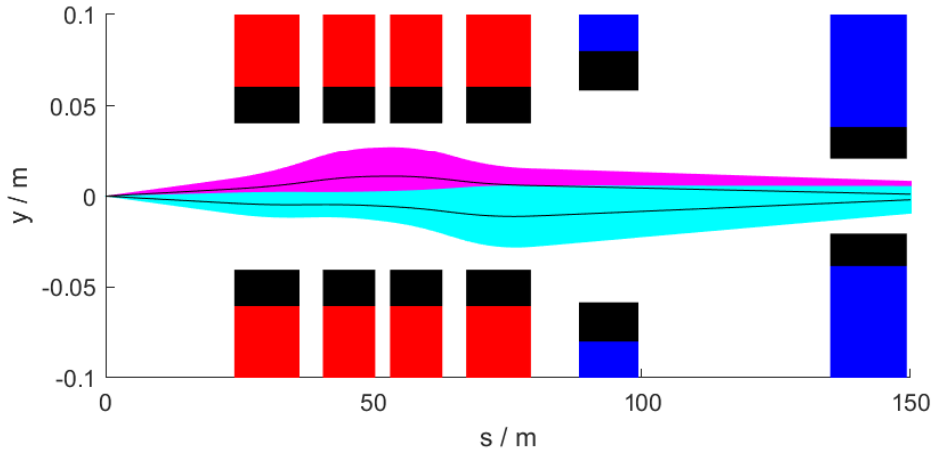

(b) Vertical

Figure 5.8: 12.5σ beam envelopes through quadrupoles (blue), dipoles (red) with shielding (black) for beam 1 (magenta) and beam 2 (cyan).

5.5 Matching

The aim of the matching section and dispersion suppressor is to match the optics so that the Twiss functions are at the correct value at the arc interface and ensure that there is no dispersion in the IP. On top of this it is important to have the right phase advance between the IP and the arc sextupoles. In the LHC, this phase advance is matched to be $\frac{2n-1}{2}\pi, n \in \mathbb{Z}^+$ from the IP to the first sextupole in that plane [42].

This phase advance is important in order to have a high efficiency in the chromaticity correction but also for correcting the spurious dispersion induced by the crossing angle bump using an HL-LHC like scheme. In the case of the FCC-hh the spurious dispersion correction had a significant positive impact on the DA [108], moreover, this would become more important should an ATS optics be used for the HE-LHC.

5.5.1 Matching Section

Since the dipoles are chosen in such a way that the position of D2 remains the same as in the SLHC V6.1a lattice and because the room reserved for the crab cavities is more than sufficient, the location of the matching quadrupoles can be adapted from the SLHC V6.1a lattice. The LHC's NbTi matching quadrupoles have a maximum gradient of 200 Tm^{-1} [30, p. 222] and the HE-LHC aims to use FCC-hh technology with a 80 % higher maximum gradient of 360 Tm^{-1}. At the same time the HE-LHC has a 93 % higher beam rigidity than the HL-LHC, meaning that longer quadrupoles are needed to achieve the same integrated fields.

It is not known how much longer these quadrupoles have to be, therefore the required length was determined from the matching. To do this the matching is initially done without any maximum strength constraints in the quadrupoles. The solution was then taken and the integrated strength of each quadrupole was calculated to work out the required length such that the maximum field is below 360 Tm^{-1}. The matching was then repeated with the longer quadrupoles and no constraints to determine if the quadrupoles are long enough. This was performed until a sufficient solution was found, the final results are shown in Table 5.3.

Quadrupole	Length [m]		Increase [%]
	LHC	HE-LHC	
Q4	3.4	3.4	0
Q5	4.8	5.8	20
Q6	4.8	7.2	50
Q7	2×3.4	2×5.1	67

Table 5.3: Lengths of HE-LHC matching quadrupoles compared to LHC quadrupoles.

From Table 5.3 one can see that the length of the matching quadrupoles increases most for the magnets farther away from the IP. One reason for this might be the fact that the β functions are smaller in this region and the focusing effect is proportional to the β functions. Considering the typical drift between the quadrupoles is about 20 m, as seen in Figure 5.8, these increases of a few metres do not reduce these drifts significantly.

5.5.2 Dispersion Suppressor

The DS is adopted from the (HL-)LHC with two FODO cells with two arc dipoles between each pair of quadrupoles. The three quadrupoles are individually powered so they can be used to match the dispersion. On top of this the first three arc quadrupoles are individually powered so that they can help match the optics to the arc. In the LHC the matching is also helped using the first FODO cell, however, this is done using short trim quadrupoles which allows all main arc quadrupoles to be powered in series [68]. The decision to power the first three arc quadrupoles independently may result in slightly higher costs but results in a lot more flexibility.

In the LHC the length of the three quadrupoles in the DS is 4.8 m, this length was adapted for the majority of the HE-LHC [71]. However, in order to help the matching,

the length of these quadrupoles in the two EIR is increased by 25 % to 6 m. This increase results in a slight shift in the DS dipoles, which can be compensated by changing the drift between the arc and the DS. This might have an impact on the geometry, in this case this would have to be improved in further iterations. The length of the arc quadrupoles cannot be changed since this is dictated by the arc cell design which is driven by energy reach, geometry and correction schemes [71].

5.5.3 Matching Results

Using the modified matching section and DS, the IR optics can be matched to the arcs for both the 18 and 23 arc cell lattice. The matched optics for the 18 arc cell layout is shown in Figure 5.9 and the optics for the 23 cell layout is presented in Figure 5.10. In both cases the Twiss functions are matched to the arc and the dispersion is sufficiently suppressed.

In both lattices, matching is done by matching each side of the EIR separately, starting from the IP with $\beta_z = \beta^*$ and $\alpha_z = D_z = 0$. MADX usually computes the Twiss functions from left to right, so in order to match from the IP to the left arc the matching script extracts and reflects this section before matching it and passing the resulting strengths back into the original sequence. First, only the β functions are matched to the arc and the strengths are saved. Next, the α functions are added to the constraints, before adding the dispersion constraint. Another constraint implemented is that the β functions have to be below 3000 m due to aperture constraints. The matching is done using various weightings of the strengths of the individual quadrupoles in order to avoid converging on local minima to obtain the best result.

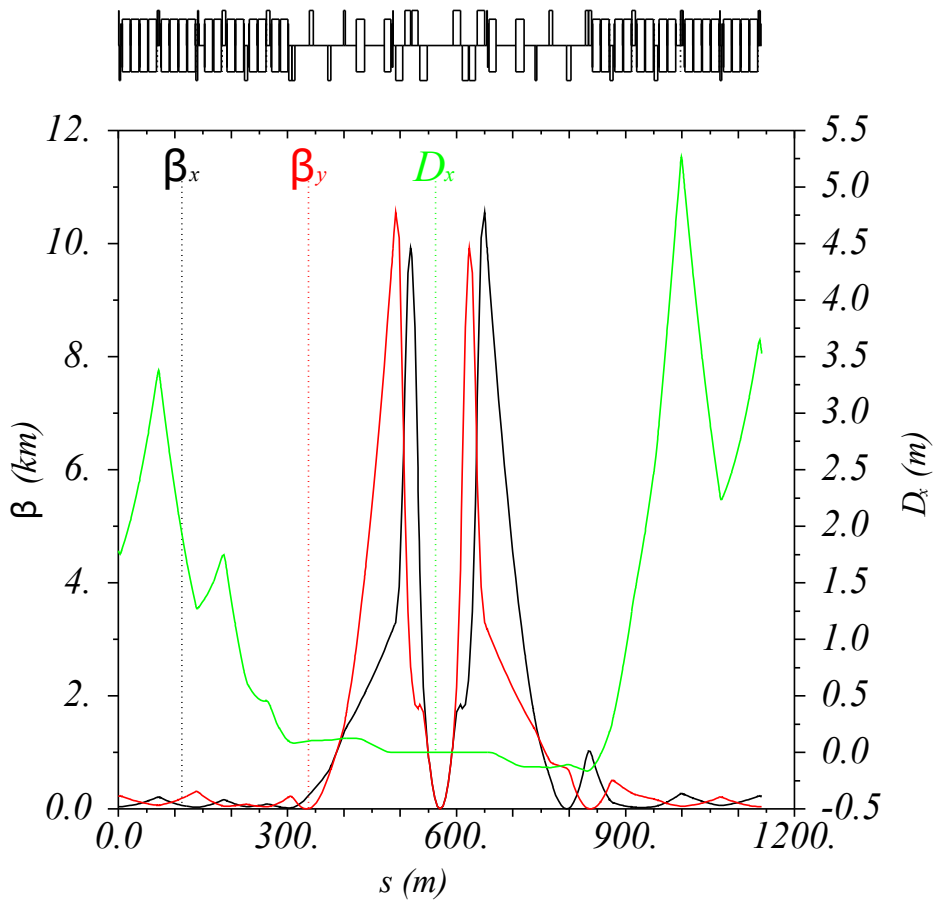

Figure 5.9: EIR collision optics for HE-LHC with 18 arc cell layout.

The only limitation of the matching shown in Figures 5.9 and 5.10 is that the phase advance in the horizontal plane on the right hand side of the EIR could not matched to be exactly $\frac{2n-1}{2}\pi, n \in \mathbb{Z}^+$ but is off by 0.14π in the 18 cell layout and by 0.06π in the 23 cell layout. The most likely reason for this is that in order to suppress the very large arc dispersion on the right hand side of the EIR, the β functions in the DS have to be relatively large, putting a limit on the possible phase advance. Since the arc dispersion in the 23 cell layout is lower than in the 18 cell layout, the effect is not as dramatic in this situation.

Another point worth noting about the dispersion peak on the right side of EIR is

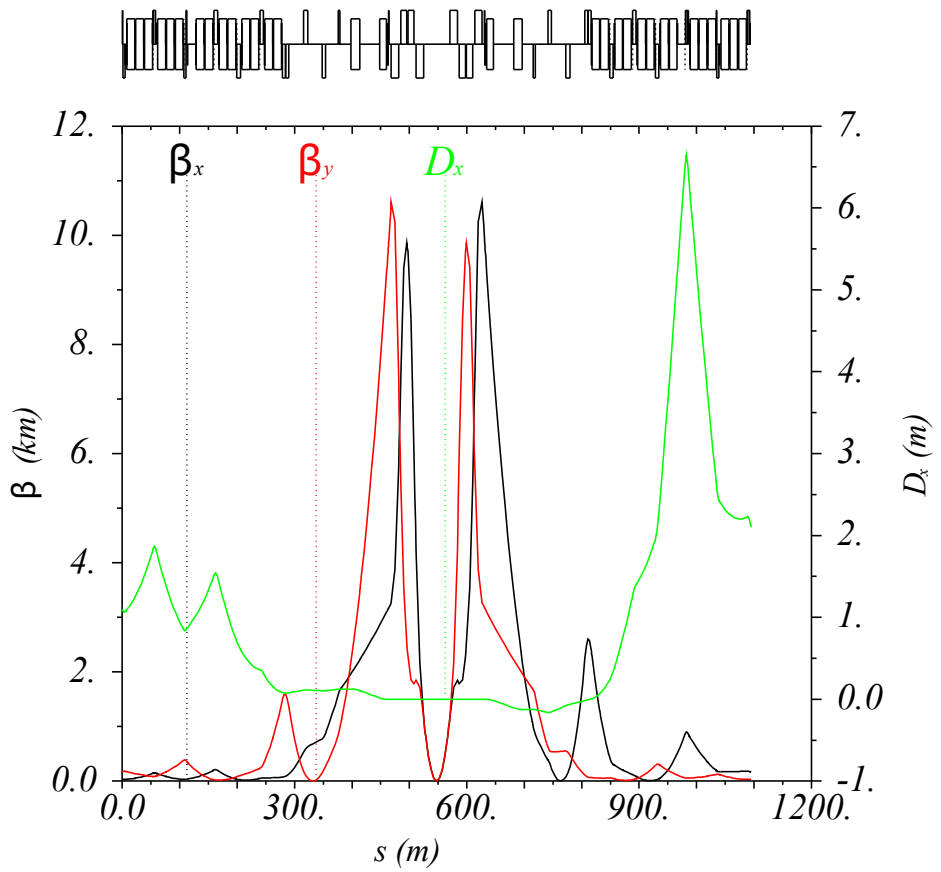

Figure 5.10: EIR collision optics for HE-LHC with 23 arc cell layout.

that the peak of the dispersion is in the gap between the DS and the first arc cell, which means there is space for a collimator at location of the dispersion peak. This is especially desirable for ion runs since the collisions produce ions with different charge to mass ratios, these particles can be treated as off momentum particles that are most likely to be lost in areas of large dispersion. Since the right hand side is downstream of the IP for beam 1, a collimator in this region can prevent these particles from being lost in the cold magnets.

5.5.4 Spurious Dispersion Correction

The EIR matching ensures that the dispersion contributions from the arc dipoles, DS and separation dipoles cancel at the IP to give zero dispersion. This matching does not consider the dispersion due to the dipole fields of the orbit kickers used to achieve a crossing angle or separation at the IP. If the beam is on an orbit with a crossing angle, as shown in Figure 5.11a for a lattice with the 23 cell arc layout and the EIR presented above, spurious dispersion arises. This produces a dispersion wave that propagates through the entire machine, as shown in Figure 5.11b. In the example in Figure 5.11 the crossing angle is in the horizontal plane in IP1 and in the vertical for IP5 and causes the arc dispersion to be larger than nominal in both planes.

This dispersion wave can have a negative impact on the dynamic aperture because it breaks the periodicity in the arcs. It also changes the beam size which has an effect on the luminosity and functionality of the other IRs. One method of dealing with this dispersion wave that was proposed for the LHC involves inducing an orbit bump in the arcs adjacent to the EIR [119]. These bumps should be in the same plane as the respective crossing angles and can be produced using the first two orbit kickers in the arc. The kicks can be matched in such a way that the resulting orbit through the quadrupoles and sextupoles cancels out the effect of the dispersion wave so that the dispersion in the next IR is back to the nominal value. Finally, the last two arc kickers can be used to steer the beam back onto the nominal orbit.

The correction works because the offset orbit through the quadrupoles and sextupoles induces dipole and quadrupole like fields as outlined in Section 1.2.4. The

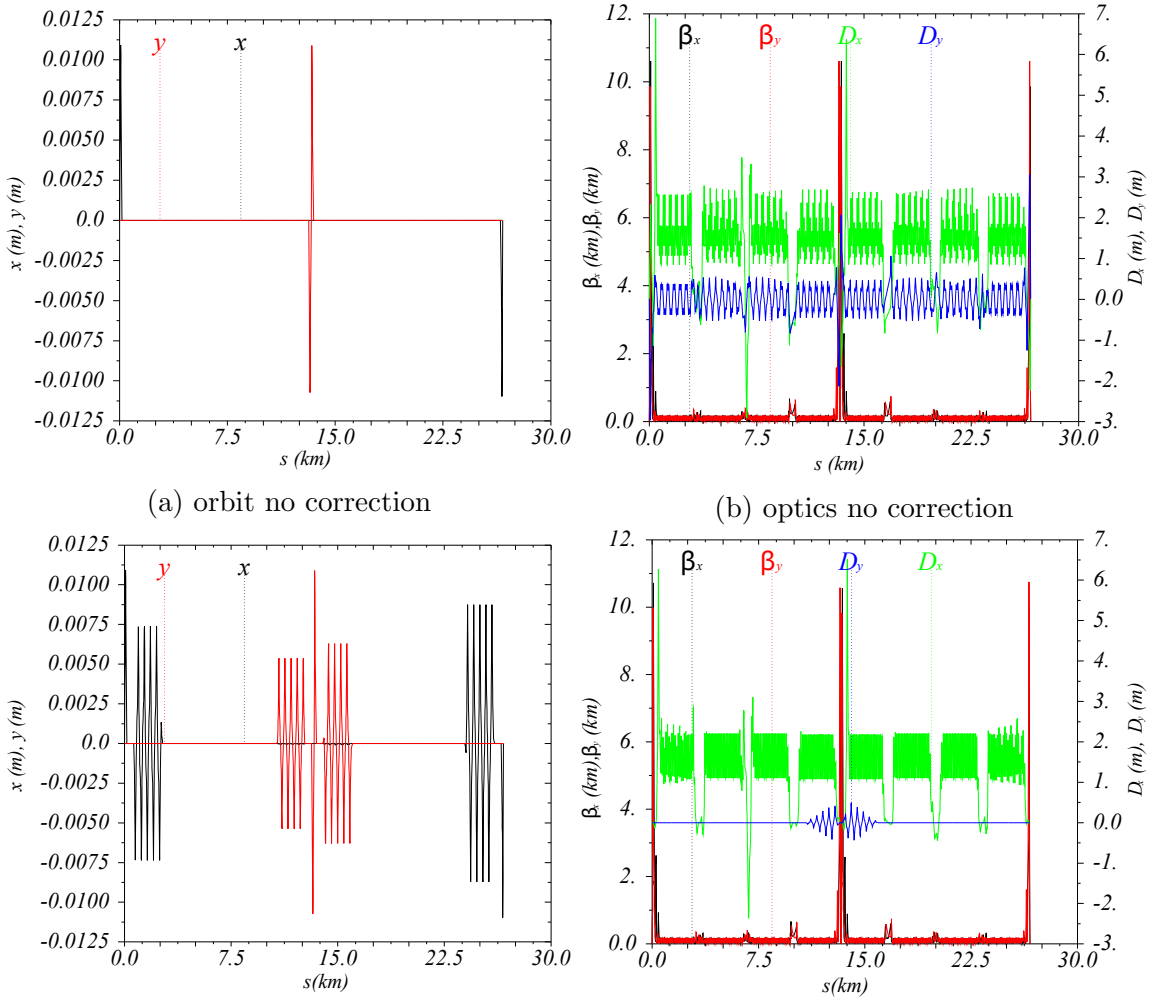

(a) orbit no correction

(b) optics no correction

(c) orbit with correction

(d) optics with correction

Figure 5.11: Beam orbit and optics without and with spurious dispersion correction for collision optics with horizontal crossing in IP1 and vertical crossing in IP5.

phase advance of $\frac{2n-1}{2}\pi, n \in \mathbb{Z}^+$ to the first arc sextupole ensures that correction orbit does not induce skew terms. The fact that this condition is not met in the horizontal plane in the right hand side of the EIR in the matched optics has a direct impact on the spurious dispersion suppression scheme. The first effect is that the dispersion and orbit can only be matched correctly if a small bump in the non-crossing plane is induced simultaneously as shown in Figure 5.11c.

Another effect is that the orbit bump is slightly larger in the arc on the right of

the EIR, which is where the slight mismatch is located. Moreover, the orbit bump due to the horizontal crossing angle is larger than that in the vertical plane with a maximum amplitude of almost 9 mm. This is quite a significant deviation given that the HE-LHC beam screen is roughly 27.6 mm wide and 24.4 mm high [120]. However, this correction is only used with the collision optics which is used at top energy. At this energy the emittance will have decreased by a factor 30 and hence the beam size would be $\sqrt{30}$ times smaller than at 450 GeV injection, meaning there should be enough space for a bump taking up about one third of the aperture.

5.5.5 Injection Optics

There are currently three injection scenarios for the HE-LHC. The most cost efficient approach considers an injection from the current SPS at 450 GeV whilst the other two assume an upgraded SPS with superconducting magnets made with one or two layers of superconductor reaching energies of 900 GeV and 1300 GeV, respectively [72]. Since the injection energy is not fixed, the injection optics have to provide enough aperture for the 450 GeV injection, which has the largest emittance.

The injection optics designed for this purpose has a β^* of 11 m, similar to that of the HL-LHC. Since the triplet β functions are relatively small, the chromaticity and spurious dispersion correction are not important. Therefore, the phase advance from the IP to the sextupoles does not have to be matched. However, the overall phase advance of the EIR should be the same as for the collision energy to avoid tune changes during the squeezing process.

The injection optics designed with these requirements is shown in Figure 5.12.

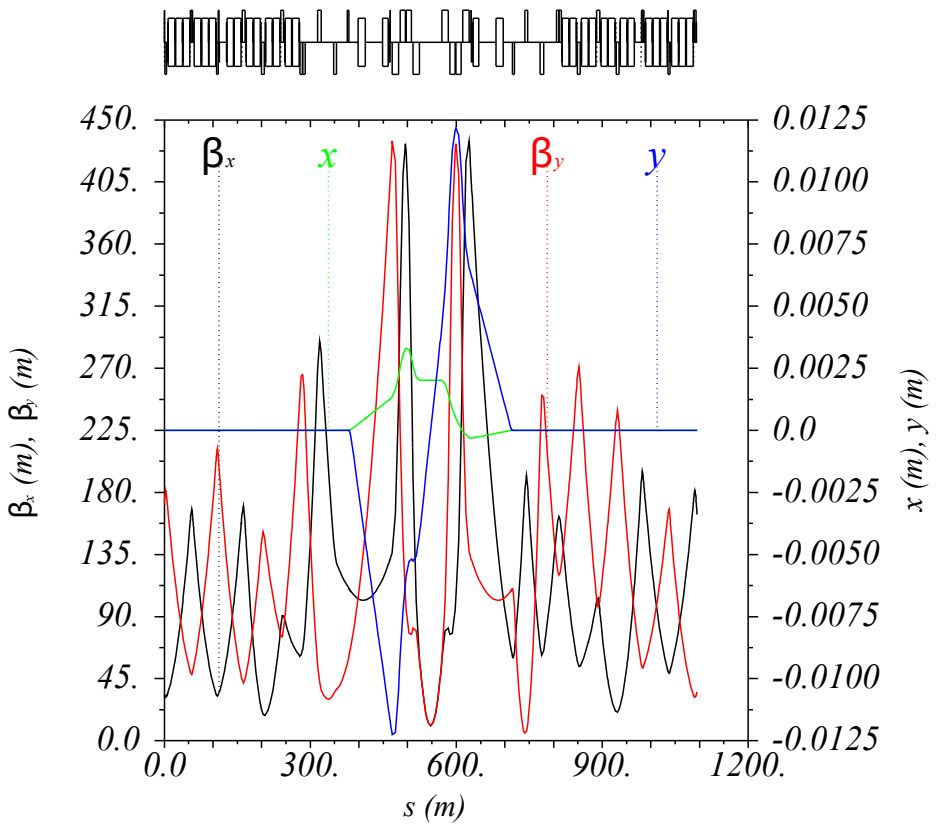

Figure 5.12: Injection optics for the HE-LHC for 23 arc cell optics.

Figure 5.12 also shows the beam orbit for a 16.785 σ crossing angle in the vertical plane and a 16.785 σ separation in the IP. This separation and crossing is needed to avoid beam-beam interactions that can have an impact on the tune and DA.

The BSC in the triplet for this optics at 450 GeV is shown in Figure 5.13, from the plot one can see that the BSC is larger than 17 σ meaning there is sufficient margin should the crossing and separation need to be increased.

5.6 Dynamic Aperture

Apart from being able to create an EIR that achieves the luminosity requirements in the space available whilst still offering enough aperture and protection to the machine components, the impact of the EIR on the rest of the lattice has to be studied. In

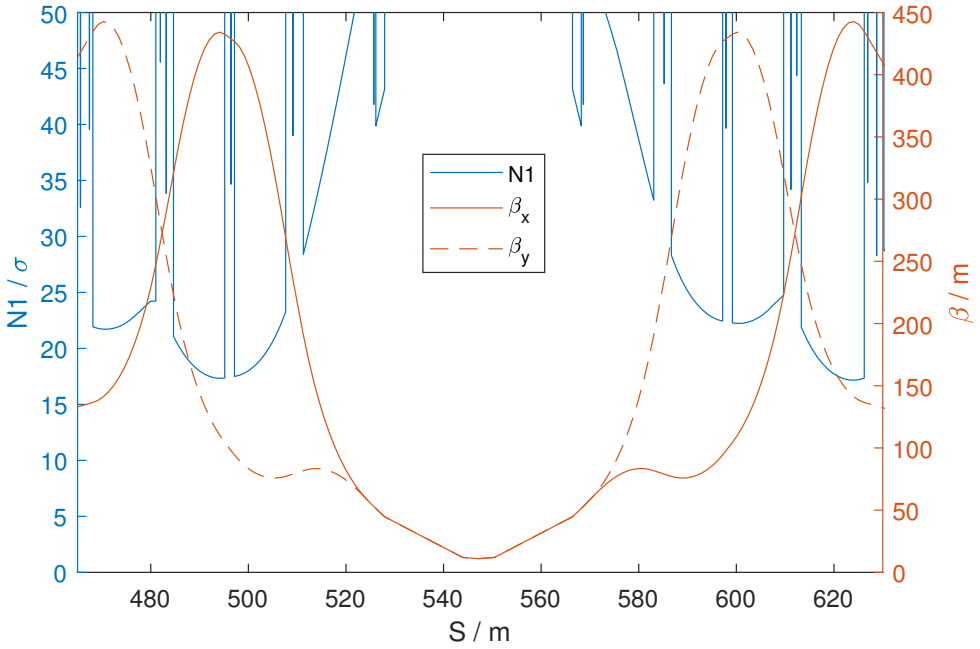

Figure 5.13: BSC and β functions in HE-LHC triplet for 11 m injection optics

particular, the effect the high β functions and non-linear errors in the triplet have on the DA have to be understood and the scope of the methods to counter this effect has to be studied. This is done with a HE-LHC lattice version 0.5 which has the EIR outlined above integrated into the 23 arc cell layout, this arc layout was chosen to be the baseline in the course of the HE-LHC study as the 18 cell layout did not have enough physical aperture in the arcs at injection [111]. Based on the experience with the LHC [48], a minimum DA of 10 σ with all errors and beam-beam effects should be achieved. Based on previous experience for the FCC-hh, the DA decreases by about 5 σ when other errors are added [108], therefore, a DA of about $15 - 20$ σ is required when just applying triplet errors, in order to leave enough margin for when further magnet errors and beam-beam effects are added.

5.6.1 Triplet Errors and Machine Parameters

The tracking for the DA studies are done for 10^6 turns using Sixtrack [20] with a momentum spread of $\Delta p/p = 1.7 \times 10^{-4}$ as predicted by the RF design team [121] and closed-orbit uncertainty of 2 mm. The tracking requires a thin lens Sixtrack lattice file that is generated using MADX, in order to perform the symplectic tracking. The error table used for the triplet quadrupoles is based on the triplet error table of the HL-LHC [31, p. 101] scaled to the aperture radius of the HE-LHC triplet magnets. The errors are applied to the magnets in MADX before the Sixtrack conversion takes place.

Three types of errors are specified in the HL-LHC error table. The first type is the systematic error, b_{nS}, which arises from design limitations in the bulk of the magnet such as the realistic geometry of the coils as well as the fringe field effects at the ends of the magnets. These errors can be predicted and measured and are the same for each magnet. Since the lattice uses thin lenses the average error throughout the magnet has to be applied to the lenses rather than applying the individual bulk and end errors separately. This average is calculated as

$$b_{nS} = \frac{L_{bulk} \times b_{bulk} + L_{ends} \times b_{ends}}{L_{bulk} + L_{ends}}, \tag{5.2}$$

where L and b are the lengths and errors of the bulk and the ends pieces. Hence, the systematic error from the HL-LHC error table has to be recalculated for the length of the HE-LHC triplet quadrupoles.

The two other types of errors are the uncertainty, b_{nU}, and the random error, b_{nR}. For each magnet these three errors are combined to the total error, b_n, as

$$b_n = b_{nS} + \frac{\xi_U}{1.5} b_{nU} + \xi_R b_{nR}, \tag{5.3}$$

where ξ_U and ξ_R are random Gaussian numbers with a standard deviation of unity generated in MADX and truncated at 1.5 and 3, respectively. ξ_U is the same for all magnets of a family and this term represents the uncertainty in the design of the magnets whilst ξ_R is different for each magnet and the term encapsulates random imperfections in each magnets. The estimates for both b_{nU} and b_{nR} can be adapted from the HL-LHC table but the HL-LHC's reference radius at which these harmonics are measured has to be scaled to adjust for the different coil aperture in the HE-LHC triplet magnets.

In order to have an accurate idea of the DA the tracking is performed 60 times, with 60 different seeds for the random variables ξ_U and ξ_R. This is done by using the SixDesk Run Environment [23] and the most pessimistic value from all the seeds is taken as the minimum DA. The DA is determined using the post processing function of the SixDesk software [23] determined at seven angles.

5.6.2 Dynamic Aperture Results

In order to establish a baseline and to check the thin lattice, an initial simulation without any errors can be performed. After loading the thin lattice the tune and chromaticity are matched using the arc quadrupoles and sextupoles respectively. Next, the 16.785 σ crossing angle is matched and activated and the spurious dispersion correction outlined above is implemented. The lattice is then converted for tracking, the results for all seven angles are shown in black in Figure 5.14 with a minimum of

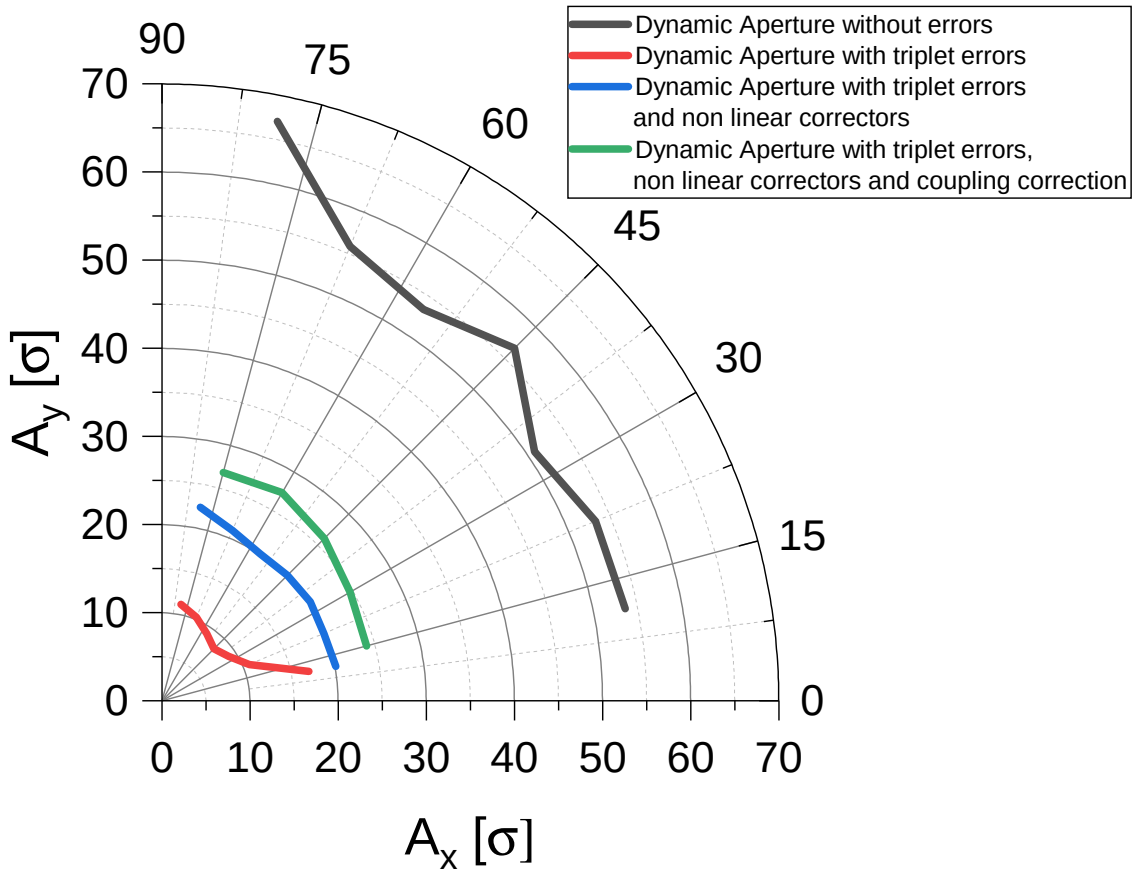

Figure 5.14: HE-LHC DA computed using 10^6 turns without errors and using 60 error seeds and various correction schemes.

DA of 50.8 σ.

The next simulation applies the errors as discussed in Section 5.5.4 but does not apply any corrections. The minimum DA computed using all 60 error seeds at each angle is plotted in red in Figure 5.14. This leads to the minimum DA dropping to 8.1 σ, which is not sufficient for operation when additional effects such as beam-beam are included.

In order to improve this, the non-linear corrector package at the end of the triplet can be used to cancel several resonance driving terms, as described in Equation 1.37. This is implemented by MADX calling a python script that reads out the errors and β functions throughout the triplet and computes which multipole strengths are required to cancel out a set of resonance driving terms. The strengths are then read in by the MADX file again. Based on LHC experience [13] the resonance terms chosen for correction are the $c(a_3; 0, 3)$ and $c(a_3; 3, 0)$ as well as the $c(b_3; 1, 2)$ and $c(b_3; 2, 1)$ terms. The resulting minimum DA using this correction is plotted in blue in Figure 5.14 with a minimum of 21.4 σ, which is safely above the minimum required DA.

The DA can be further increased by reducing the linear coupling caused by the errors. This is done by matching the skew quadrupole next to the triplet in MADX so that the coupling matrix reduces to zero. On top of this the double tuning method used in the FCC-hh [108] was applied to find an optimum working point by adjusting the phase advance between the EIR by varying the strength of the arc quadrupoles. These two methods increase the minimum DA to 24.0 σ and is show in green in Figure 5.14.

5.6.3 Double Tuning

The positive impact double tuning can have on the DA of future hadron colliders is apparent from Figure 5.14 and from work on the FCC-hh [108]. The simplest way to change the tune between the EIRs is to slightly change the phase advance in each arc cell. The downside to this is that it can increase the β functions in the arcs and

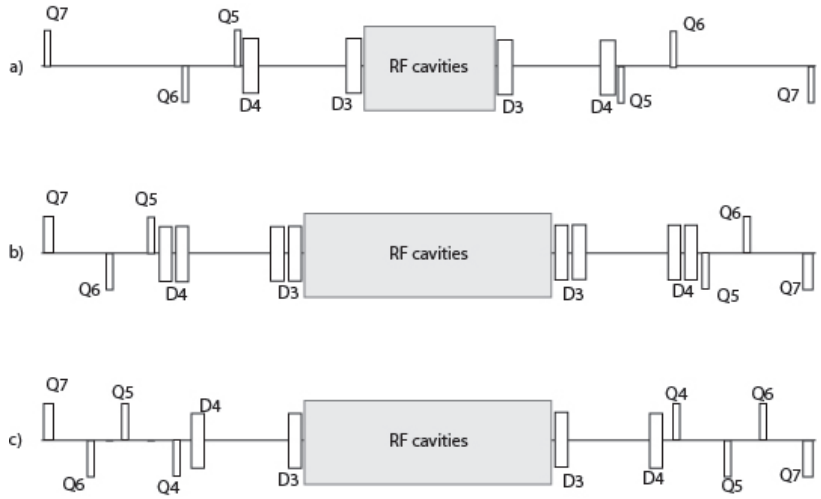

Figure 5.15: Conceptual layout for IR4 for a) LHC b) optimised HE-LHC c) HE-LHC with added tuning quadrupole.

have an impact on the efficiency of correction schemes. An alternative way to achieve the tuning is to change the phase in the IRs between the two EIRs. To illustrate this concept, the HE-LHC's IR4, which contains the RF cavities and instrumentation, was redesigned to be able to achieve a large range of phase advances.

Since the HE-LHC aims to rapidly ramp to higher energies it will need more RF cavities than the LHC and since the beam separation and rigidity is larger than that of the LHC, the layout of this IR was already being modified for the HE-LHC [122]. The layout for the design optimised for this purpose is shown in b) of Figure 5.15, which also shows the layout of the LHC's IR4 in a) for comparison. In order to achieve the required flexibility in phase advance, a fourth quadrupole, Q4, was added to the design, this is shown in c) of Figure 5.15.

The optics of IR4 in the LHC are shown in Figure 5.16a, which can be compared to the optics in the HE-LHC with the extra quadrupole in Figure 5.16b. From the two plots in Figure 5.16, one can see that the maximum β functions in the IR are

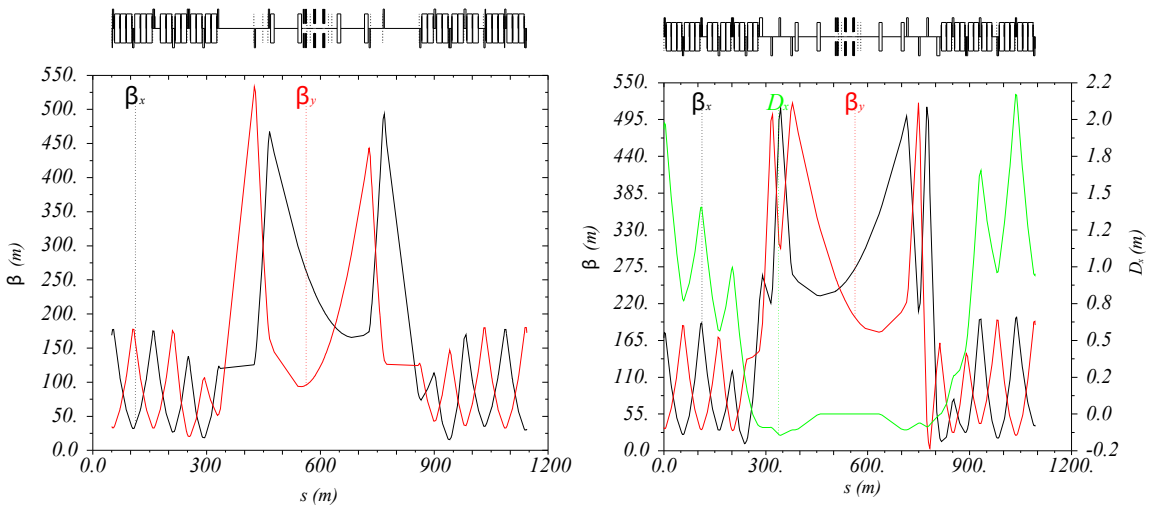

(a) LHC (b) HE-LHC

Figure 5.16: Optics for IR4 in LHC and HE-LHC with added tuning quadrupole.

unchanged even though the length of the drift reserved for the cavities has increased. This is achieved by making the quadrupoles slightly longer so that they can achieve a larger integrated field. Another point to note is that in the LHC the β functions in each plane have one peak either side of the centre of the IR, whilst in the HE-LHC there is an additional β peak on each side. This is due to the fact that there is an extra degree of freedom for the matching from the additional quadrupole.

This extra freedom can be used to manipulate the β functions in the IR without changing the β functions at the arcs and in the cavities. The β functions can be matched in such a way to give the desired phase advance in both planes over the IR. Some examples of optics where the phase advance has been changed is shown in Figure 5.17, in which one can see how the matching changes the positions of the peaks but keeps the optics and dispersion in the region of the cavities constant.

The phase advance range of the IR can be explored by increasing or decreasing the phase advance in either one or both planes as much as possible whilst keeping

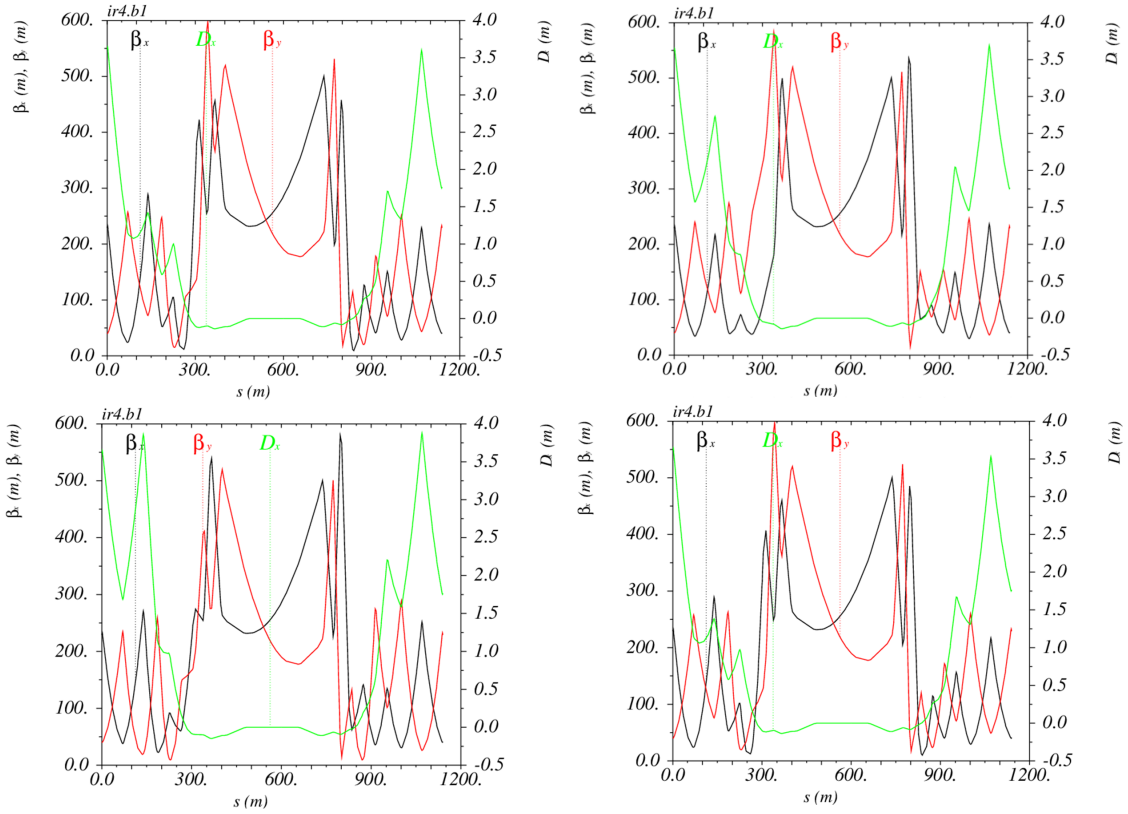

Figure 5.17: Examples of HE-LHC IR4 optics changed in order to achieve various phase advances.

the optics in the arc and cavity areas constant and not allowing any β functions to increase by more than 10 %. When increasing or decreasing the phase advances in both planes simultaneously, the magnitude of these changes were set to be the same in the two planes. The phase advances achieved using this matching are plotted in Figure 5.18. The points are connected using the smooth line feature in Microsoft Excel to give an idea of the overall range available.

As seen in Figure 5.18, IR4 has a phase advance range of more than π in each plane. If another IR, for example IR6, containing the beam dump, was to be optimised the entire machine could be tuned over the full 2 π range just using the IRs. This could be useful for maintaining the machine tune during β squeezing in the EIR without

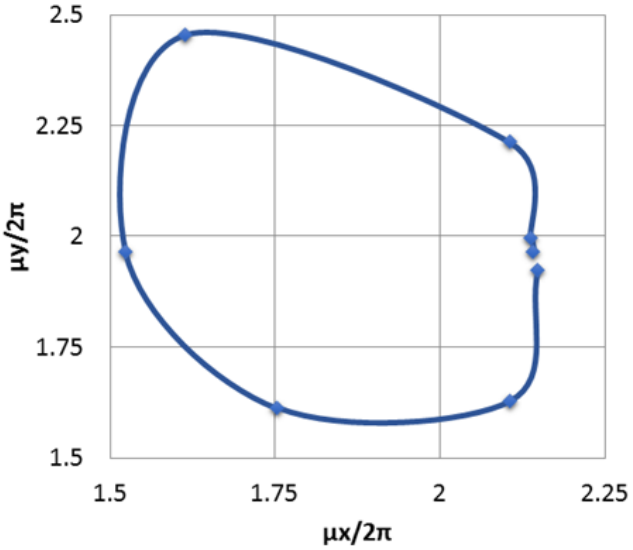

Figure 5.18: Phase advance range of HE-LHC IR4.

changing the arc optics. More importantly, since IR4 and IR6 are on opposite sides of IR5, the two IRs could be used for the double tuning process without affecting the arcs. The LHC IR6 was designed to have a large range of phase advances [45], therefore this IR would be a good choice for this optimisation. However, implementing this would require a first optics design from the beam dump team.

5.7 Conclusion and Outlook

The HE-LHC EIR presented in this chapter largely meets the requirements set at the beginning of the design process. The triplet optimisation tool and the experience from the FCC-hh design have helped create a triplet that is significantly shorter than expected. This leaves sufficient room for the separation and matching sections that have been adjusted for the HE-LHC beam. The layout of the DS might require further optimisation to help adjust the HE-LHC's layout. Another interesting addition might be the matching of ATS optics that can be used to squeeze the β^* as the beam

emittance burns off in order to keep a constant luminosity.

The phase advance to the arc sextupoles could not be matched perfectly, however, spurious dispersion correction is still possible as shown above. Whilst future design iterations should aim to improve this phase advance, this should have a relatively low priority as the DA is already large. The inclusion of beam-beam effects and other magnet errors for the DA studies would make the simulations more realistic and help identify potential issues. This could also include further iterations on the double tuning, which ideally could be done with the IR4 presented in this chapter and an updated IR6.

Chapter 6

Optics for Experimental Applications and Analysis Methods

6.1 Motivation

The impact errors in the triplet can have on the DA has been illustrated in the previous chapters. On top of magnet errors, errors in magnet and beam alignment and in the Twiss functions can decrease the DA and BSC. These factors are included in the DA and BSC studies in the previous chapters as tolerances that are used to anticipate the worst possible case. Therefore, on top of modifying optics designs to increase the DA, decreasing and understanding these tolerances can increase the stability and acceptance of the beam. Being able to precisely measure the beam and machine optics is also important for controlling the luminosity of the machine since changes in the β^* and orbit can decrease the luminosity considerably.

These factors motivate the work presented in this chapter, where optics and experimental methods that can be used to improve the knowledge about the alignment and Twiss function in the EIR are presented. These methods are applied to LHC data as it is the largest hadron collider and the most similar machine to the ones

explored in the previous chapters.

First, this chapter will present the design procedure and outline possible challengers of an optics that switches off the triplet and Q4 magnets to create a field free region for BPM alignment. Next, it will look at the k-modulation method for β^* measurements and its limitations in general and for van der Meer optics in particular. Finally, it will outline a method that uses singular value decomposition (SVD) and k-modulation data to compute the alignment errors in the triplet and discuss how this could also be used to improve the β^* and crossing angle measurement.

6.2 Ballistic Alignment Optics

Ballistic optics are configurations in which a series of quadrupoles are switched off so that the beam can travel in a straight line through a field free region. The readings from the BPMs whilst these optics are used allow one to find the centres of the BPMs and identify the ideal path of the beam. A ballistic optics with the triplet quadrupoles turned off is especially important since the quadrupole fields are high in this region and a precise measurement of the orbit can improve the luminosity, BSC and DA. For this reason, a ballistic optics with the triplet turned off for the LHC was already considered and matched during the LHC's design phase [123]. Moreover, triplet free optics have been designed, tested and used for measurements in the LHC [124]. The ballistic optics in IR5 used during the 2016 LHC run are shown in Figure 6.1 [125].

Next to the triplet, the field in Q4 also has a big impact on the trajectory of the beam, therefore, a ballistic optics with Q4 turned off was also matched for the LHC, and this optics is shown in Figure 6.2. The biggest drawback of this optics is that

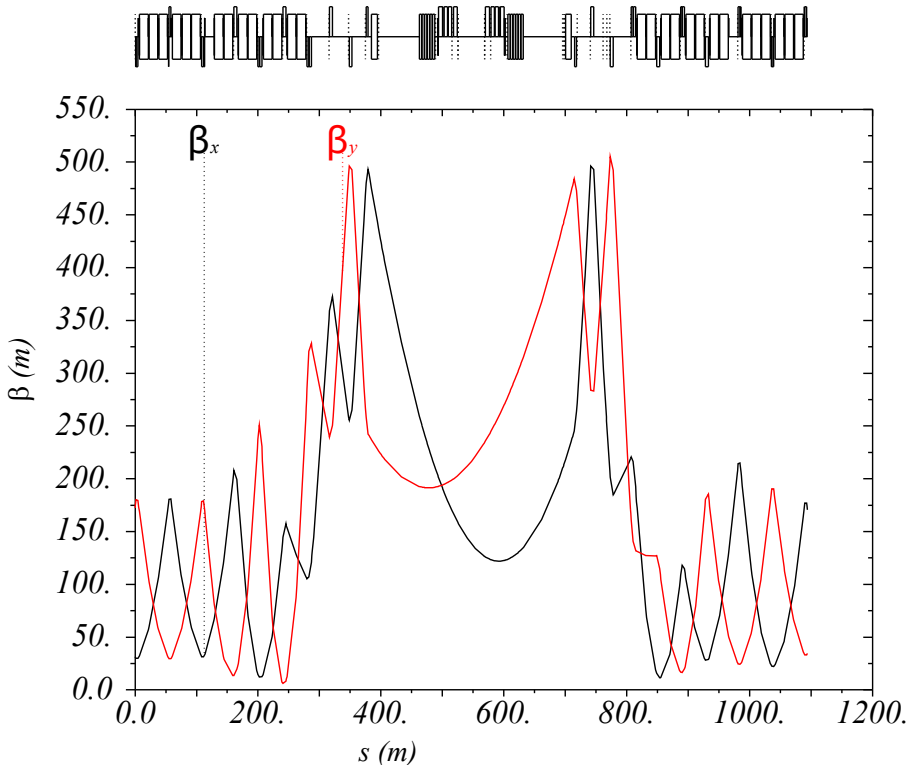

Figure 6.1: 2016 LHC ballistic optics with triplet turned off.

it is only designed to work at injection energies. Therefore, the aim for the optics presented in this thesis is to have the triplet and Q4 turned off whilst keeping the normalised magnet strengths low enough to be compatible with collision energies.

6.2.1 Matching and Hardware Limitations

The ballistic optics must have the Twiss and dispersion functions matched to centimetre level in order to be compatible with the machine and the fractional tunes of 0.28 and 0.31 in the horizontal and vertical planes, respectively, are conserved. Moreover, the β functions have to be low enough to ensure that the BSC is above 6 σ for a test beam with 1 µm normalised emittance. It is also desirable to have an optics that, unlike the previously designed optics, is symmetric around the IP to provide the

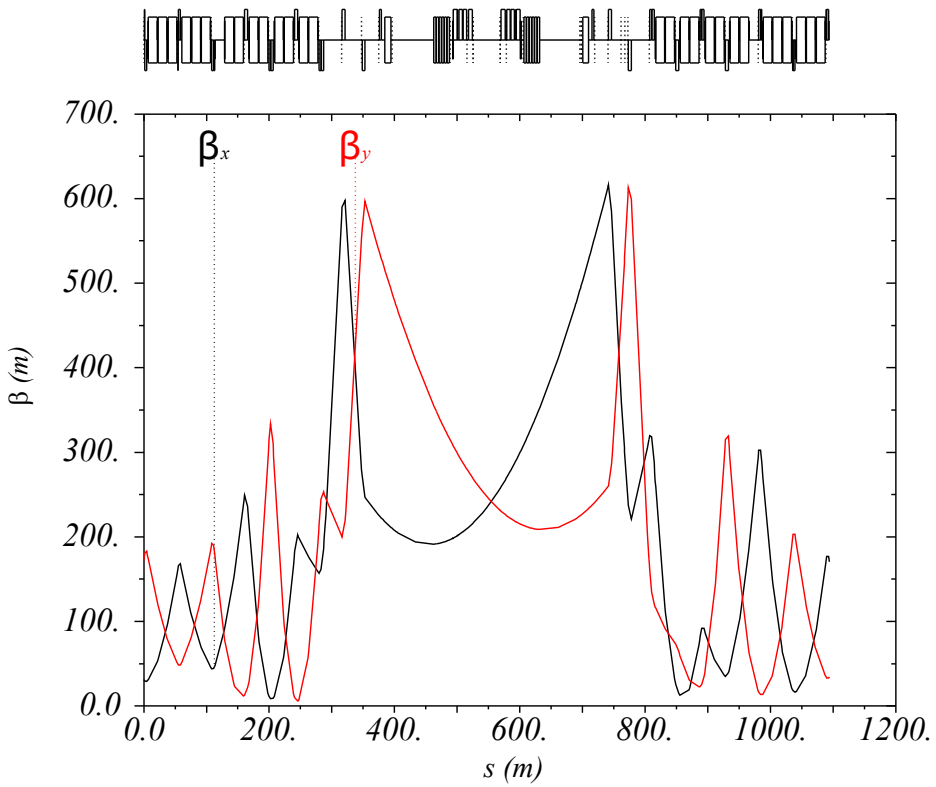

Figure 6.2: Original LHC ballistic optics with triplet and Q4 turned off.

same BPM resolution in both planes. The dispersion does not have to be matched to be zero at the IP since there are no collisions. In fact, some dispersion could even be useful for calibration purposes, on the other hand however, too much dispersion might have an impact on the BSC.

On top of the optics constraints, there are several hardware constraints in the LHC limiting the choice of magnet strengths. These constraints include that on the one hand the magnet strengths cannot exceed the maximum values at collision energy. On the other hand, very low strengths at injection are very sensitive to current fluctuations so that no magnet strength should be lower than 3 % of the nominal value. In addition, it is important that the strength imbalances between the two apertures does not exceed a factor two.

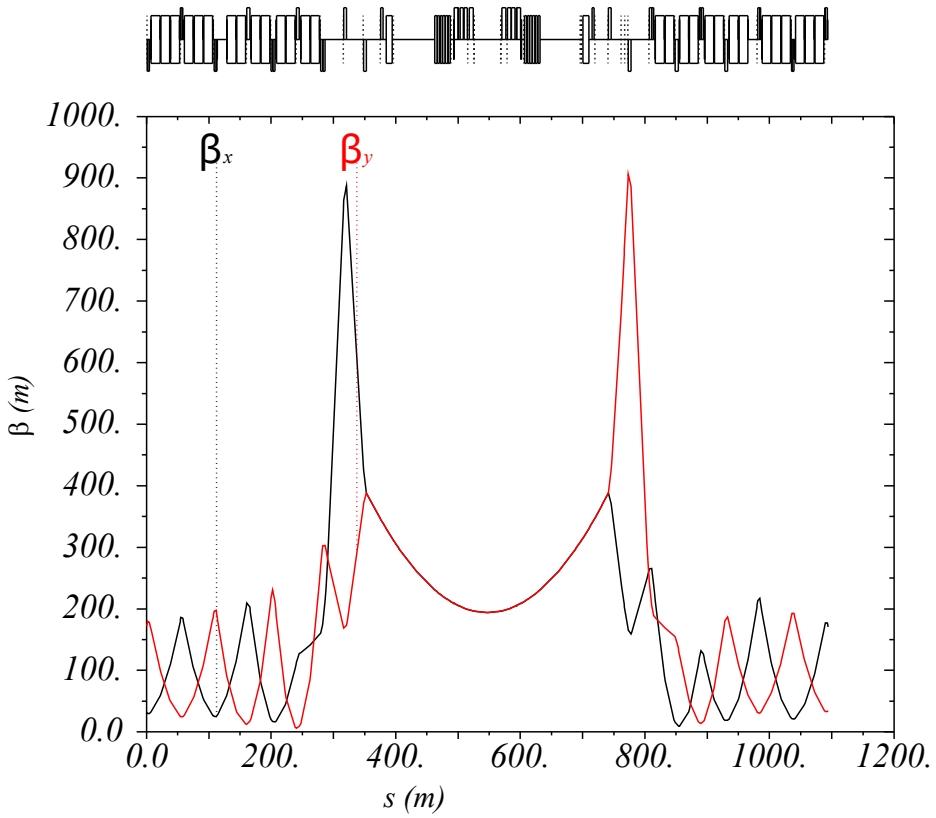

Figure 6.3: 2017 LHC ballistic optics with triplet and Q4 turned off.

6.2.2 Results

The ballistic optics designed to meet the constraints outlined in Section 6.2.1 and matched using MADX is shown in Figure 6.3. The symmetry is achieved by enforcing the condition that $\alpha = 0$ in both planes. A similar optics is designed for beam 2. The strengths of the individual quadrupoles for both beams in this optics are shown in Table 6.1, which also shows the imbalance in the strengths between the two apertures. In all cases the imbalance is between 0.5 and 2 as required.

Due to the symmetry condition and the extra switched off quadrupole, the maximum β functions for this optics are around 900 m, which is considerably larger than for the 2016 ballistic optics, where the maximum β functions were below 500 m. One

Magnet	k_{left} [10^{-3} m^{-2}]		Imbalance	k_{right} [10^{-3} m^{-2}]		Imbalance
	Beam 1	Beam 2		Beam 1	Beam 2	
Q5	**2.97**	**3.80**	0.83	**3.08**	**3.55**	0.87
Q6	5.83	5.63	1.04	5.75	5.88	0.98
Q7	**4.83**	**3.77**	1.28	**4.47**	**4.54**	0.98
Q8	**3.93**	**4.88**	0.81	**4.22**	**4.90**	0.86
Q9	8.43	7.30	1.15	8.40	7.73	1.09
Q10	7.50	8.38	0.89	7.52	7.91	0.95
QT11	5.62	3.62	1.55	3.19	4.06	0.79
QT12	3.19	4.16	0.77	1.08	1.46	0.74
QT13	5.37	4.93	1.09	5.67	7.82	0.73

Table 6.1: 2017 LHC ballistic optics with triplet and Q4 turned off.

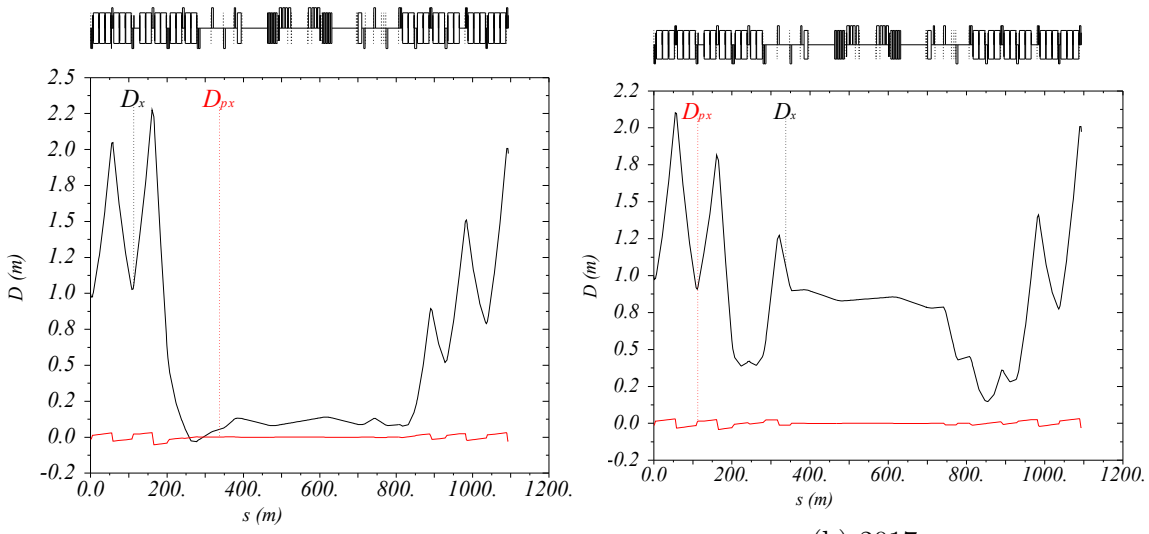

(a) 2016

(b) 2017

Figure 6.4: Dispersion of 2016 and 2017 ballistic optics.

consequence of these large β functions is that the dispersion at the IP is not fully suppressed by the DS and still has a value of almost 1 m, which is larger than in 2016, as shown in Figure 6.4. Whilst this was not one of the design goals, it can be benefitial as it can help calibrating the beam position monitors.

The effect the large dispersion has on the BSC can again be tested using the MADX aperture module on the matched optics and the physical apertures of the LHC stored in the lattice version 6.503. The aperture module is executed with a

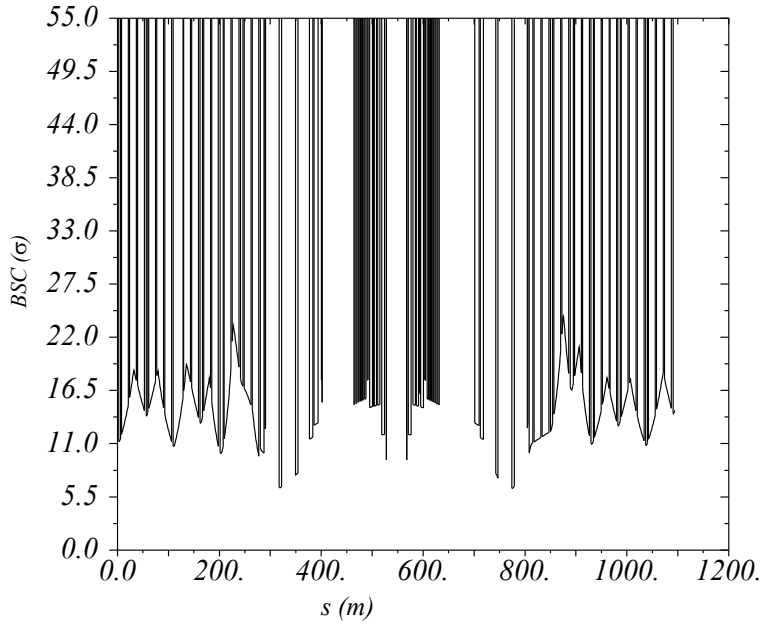

Figure 6.5: BSC for 2017 ballistic optics with triplet and Q4 switched off.

1 µm normalised emittance, an injection energy of 450 GeV and the normal LHC parameters, which are the default parameters in the aperture module [8, p. 156–158]. These default parameters include a momentum spread, $\Delta p/p$, of 0.0015 and a β beating of 20 %. The calculated BSC is shown in Figure 6.5, which illustrates that the minimum BSC is above the required 6 σ and the bottleneck is in the separation dipoles, as one would expect since the β functions are largest in this area.

6.2.3 Dry Run Testing

Whilst, all strengths are below the maximum allowed strength and above 3 % of the nominal value, the strengths of Q5, Q7 and Q8, highlighted in Table 6.1, were flagged up as they result in currents below 200 A. This might cause stability issues since the power converters are designed to have a current range of 200 A to 20 kA [126], however, in practice currents as low as 100 A have been used. The left Q5 magnet has the lowest strength in this optics with a k-value of 2.97 in the beam 1 aperture,

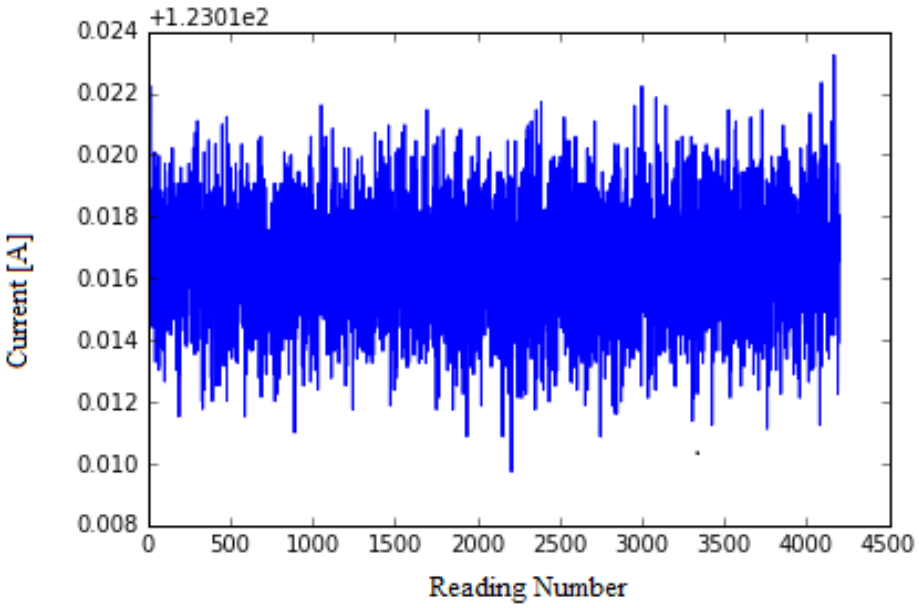

Figure 6.6: Example of current read out during dry run.

corresponding to 120 A.

In order to test the stability of these low currents, a dry run of the optics without beam was performed. This dry run was done at 3 a.m. on the 26.04.2017. During this run four converters were not set properly so they were redone later that day. The data from the current converters can be read out using the PyTimber library [127] in a python script, an example current read out for the right Q5 magnet is shown in Figure 6.6. As one can see from Figure 6.6, the current fluctuated by about 0.005 A.

In order to quantify the fluctuations the python script can work out the mean current and then work out the root mean square (RMS) deviation of the current during the dry run. This is done for the currents of all the power converters powering quadrupoles Q5, Q6, Q7 and Q8 either side of the IP. In order to get a comparison and check if these deviations are acceptable the same is done with a reference low magnet current data set obtained from the 2016 ballistic optics run, measured on the

28.03.2016.

The resulting values in each magnet are shown in Tables 6.2 and 6.3, from which it can be seen that the RMS deviation of the current deviations are of the same magnitude for both readings. The deviations are highest for some of the Q6 power supplies, however, this quadrupole was not flagged up and has a larger current than the other quadrupoles which would lead to larger deviations. After the positive outcome of the testing, the optics were used for 2017 LHC commissioning and further analysis [125].

Quadrupole	Side	Beam	RMS Error / mA	
			Ballistic	Reference
4	Left	1	2.27	5.00
		2	2.33	2.93
	Right	1	3.33	4.93
		2	3.27	2.07
5	Left	1	2.27	4.80
		2	2.4	4.50
	Right	1	2.53	3.33
		2	9.73	3.35
6	Left	1	2.73	4.65
		2	2.81	2.38
	Right	1	2.78	3.08
		2	3.85	4.46
7	Left	1	2.72	4.47
		2	2.77	2.14
	Right	1	3.50	3.82
		2	3.99	3.18

Table 6.2: RMS current deviation in IR1 magnets for 2017 ballistic optics dry run compared to 2016 ballistic optics readings as reference.

Quadrupole	Side	Beam	RMS Error / mA	
			Ballistic	Reference
4	Left	1	2.13	4.00
		2	2.20	1.73
	Right	1	1.86	4.53
		2	1.93	4.98
5	Left	1	2.25	0.14
		2	2.24	1.62
	Right	1	1.87	4.53
		2	1.73	4.83
6	Left	1	2.84	2.64
		2	2.69	3.18
	Right	1	2.31	3.19
		2	2.25	4.96
7	Left	1	2.75	3.51
		2	2.95	3.53
	Right	1	2.18	4.96
		2	2.23	4.94

Table 6.3: RMS current deviation in IR5 magnets for 2017 ballistic optics dry run compared to 2016 ballistic optics readings as reference.

6.3 k-Modulation

6.3.1 Applications and Limitations

In Section 1.2.4 it was outlined how the modulation of the k value of a quadrupole by Δk leads to a measurable tune change ΔQ_z from which the β_z in this quadrupole can be worked out as

$$\beta_z = \pm\frac{2}{\Delta k l}(\cot(2\pi Q_z)[1-\cos(2\pi\Delta Q_z)] + \sin(2\pi\Delta Q_z)) \approx \pm 4\pi\frac{\Delta Q_z}{\Delta k l}. \tag{6.1}$$

In the LHC, k-modulation has proven itself a robust and reliable method to accurately measure the β in the inner triplet and hence work out β^* and distance of the β-waist from the IP, w, and is one of several tools used to ensure a precise optics control [128]. In this process the currents in the innermost quadrupoles around

the IP are modulated and the resulting Δk is computed using the magnet models. The tune change is then measured in order to reconstruct the β functions in the two quadrupoles. These estimates can then be used to obtain a β^* and w measurement [129].

Simulations have shown that for nominal LHC collision optics this method is very accurate as it has a 0.4 % uncertainty in the absence of a waist and increases to 3.5 % for a 20 % waist (w/β^*) [129]. During the k modulation measurement of a special van der Meer (vdM) optics the measured β^* deviated from the model by 8 % on average in IP1 and IP8 with very large error bars whilst it was not able to measure a physical β^* in IP5 [130].

A major question arising from this is whether this is due to the method in general or if the vdM is a special case. vdM optics are anti-symmetric optics with the largest possible β^* achievable with $\alpha^* = 0$, that can be used for luminosity scans and calibrating the beam profile monitors [131]. Given that for $\alpha^* = 0$, the β function at the entrance of the first quadrupole is given by Equation 1.45 as

$$\beta = \beta^* + \frac{L^{*2}}{\beta^*},$$

one can find the roots of this equation to get an expression for β^* to be

$$\beta^* = \frac{\beta \pm \sqrt{\beta^2 - 4L^{*2}}}{2}, \tag{6.2}$$

for which only the solution with the negative sign is physical. From this, one can see that the largest β^* is obtained for $\beta = 2L^*$, which corresponds to $\beta^* = L^*$. Therefore,

the vdM optics are designed to have a β^* very close to L^*.

6.3.2 Mathematical Properties of Reconstruction

In order to understand the limitations of the β^* reconstruction for vdM optics it is useful to take a closer look at the mathematical properties of the simplified Equation 1.45, which assumes the waist to be at the IP. For this simplified case, the relationship between the error of the β function measured in the quadrupole and the reconstructed β^* can be approximated to first order as

$$\sigma_\beta = \left|\frac{\partial\beta}{\partial\beta^*}\right|\sigma_{\beta^*} = \left|1 - \frac{L^{*2}}{\beta^{*2}}\right|\sigma_{\beta^*}. \tag{6.3}$$

From this, the fractional error σ_β/β is

$$\frac{\sigma_\beta}{\beta} = \frac{\left|1 - \frac{L^{*2}}{\beta^{*2}}\right|}{\beta^* + \frac{L^{*2}}{\beta^*}}\sigma_{\beta^*} = \frac{\left|1 - \frac{L^{*2}}{\beta^{*2}}\right|}{1 + \frac{L^{*2}}{\beta^{*2}}}\frac{\sigma_{\beta^*}}{\beta^*}. \tag{6.4}$$

In most cases $\beta^* \ll L^*$ so that $\frac{L^{*2}}{\beta^{*2}} \gg 1$ and $\frac{\sigma_\beta}{\beta} \approx \frac{\sigma_{\beta^*}}{\beta^*}$. However, in the special case where β^* approaches L^*, $\frac{L^{*2}}{\beta^{*2}}$ approaches 1 so that $\frac{\sigma_\beta}{\beta} \ll \frac{\sigma_{\beta^*}}{\beta^*}$ meaning that a small relative error in β measured in the quadrupoles leads to a much larger error in the reconstructed β^*. To quantify this effect one can look at the LHC's vdM optics in IR8 where $L^* = 26.15$ m and $\beta^* = 24.11$ m, whereby Equation 6.4 approximates $\frac{\sigma_{\beta^*}}{\beta^*} \approx 25\frac{\sigma_\beta}{\beta}$.

Another limitation can be understood when looking at the solutions to the quadratic equation given in Equation 6.2. As β approaches $2L^*$, as is the case for the vdM optics, the discriminant $\sqrt{\beta^2 - 4L^{*2}}$ approaches zero meaning that the two solutions of the quadratic equation lie very close together. Whilst only the solution subtract-

ing the discriminant is the physical solution, a numerical solver might converge to the wrong solution in this regime. In the nominal case these solutions lie far apart and prior knowledge about the model β^* can ensure that the right solution is found, however, this does not hold for the case of the vdM optics.

A final problem that can be seen from the quadratic solution is that if there is an error in the measured β in the quadrupoles making it smaller than $2L^*$, the discriminant becomes negative resulting in a complex solution. This could prevent a numerical solver from finding a solution or result in finding solutions that do not make any physical sense.

6.3.3 Testing of the Code

The explanations given in the previous section are for a very simplified case, however, they do provide an insight in the physical properties of the reconstruction. To test how valid these approximations and insights are, the accuracy of the k-modulation β^* reconstruction code used in [129] can be applied to simulated data and artificial errors.

The code reads in Δk for the left and right innermost quadrupoles and the corresponding ΔQ in both planes. It then outputs the measured β^* and waist. In a first step a MADX model of the LHC is used with the vdM optics configuration and the nominal tune is saved. The strength of the Q1 quadrupoles in IR8 are then changed manually in the MADX script and the new tune is read out in order to determine the change in tune, ΔQ.

In order to simulate errors, the change in tune in the horizontal plane for both

the left and the right quadrupole is varied in increments of 0.1 % to be 5 % higher and 5 % lower than the actual tune change. The k-modulation reconstruction is then performed on all combinations of possible tunes and the calculated β^* values are plotted, this is shown in Figure 6.7a. The plot also contains a red circle highlighting the location the correct value. Figure 6.7b shows the same data but from a different angle and with the errors normalised to the absolute correct value.

The results shown in Figure 6.7 indicate that all of the predictions made using the simplified case described in Section 6.3.2 can be seen in the real example. The k-modulation code yields the correct result for the modelled data without errors, showing that the underlying theory of the code is still valid. However, the error in calculated β^* can be off by 10 % for tune change errors smaller than 1 %. For 5 % tune change errors the measured β function can even be off by almost 50 %.

As one would expect from the quadratic evolution of β functions in drifts and from the simplified Equation 1.45, the plotted data resembles a paraboloid, with the designed optics lying close to the point of inflection. This causes the gradient of measured β^* to be very high in tune space in this region. A nominal β^* below 1 m would be in a much flatter region and much less vulnerable to errors.

Only the lower half of the paraboloid corresponds to physical solutions, however, the code converged to unphysical solutions for a large amount of cases and can jump between the physical and unphysical results between adjacent points in tune space with only 0.1 % error between them. This issue could potentially be fixed relatively easily by constraining the solver to β^* values that are below L^*. Again, in a nominal case this would not be a problem since the physical and unphysical solutions are much

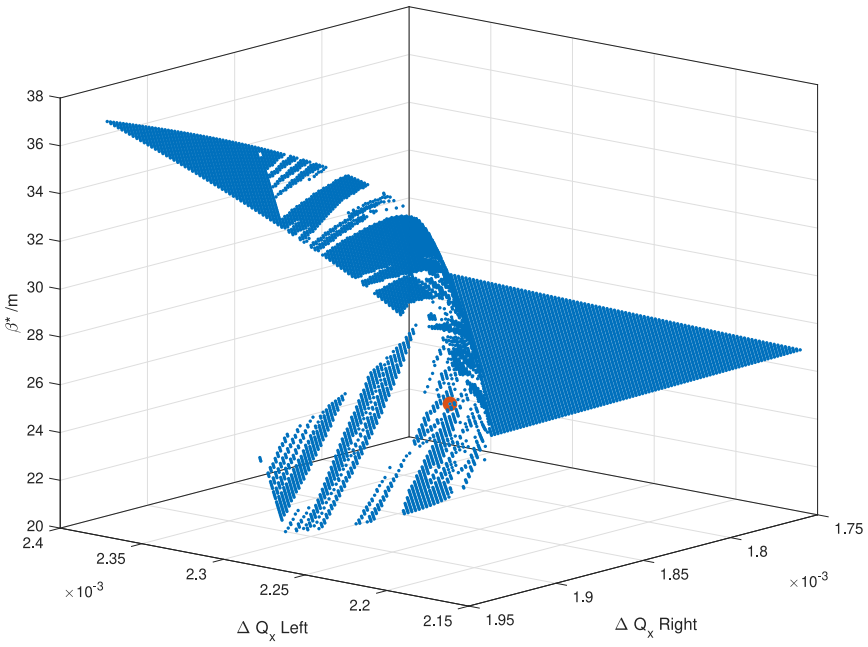

(a) Absolute value

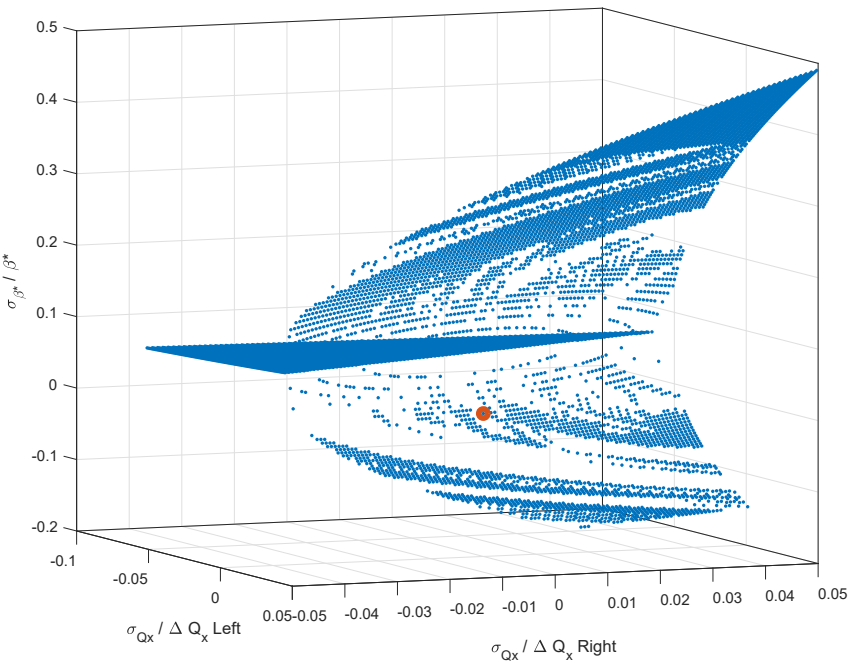

(b) Relative error

Figure 6.7: β^* computed using k-modulation code on simulated data with tune errors applied.

further apart and the solver has prior knowledge of the approximate location of the solution.

Especially in Figure 6.7a, one can see that there is a large flat region beyond the inflection point of the paraboloid for low tune changes. This corresponds to regions where the solutions to the quadratic equations would be complex. To fully understand what the found β^* values mean one would have to take a closer look at the code and the libraries used, however, it is likely that the code just returns the real component of the solution, which would be $\beta^* = L^*$ according to Equation 6.2. This region is normally sufficiently far away from the actual solution, however in the case of the vdM optics it would be helpful to modify the code to return an error message when the solution is complex to make it easier to spot errors in the measured tune.

Overall this analysis has given a valuable insight in the limitations of measuring vdM optics in general since other methods can often measure β functions around the IP accurately but the β^* reconstruction is prone to give large errors in this regime. This provides strong motivation to improve measurement techniques but also to re-think the type of optics used for calibration measurements. Moreover, the analysis has provided a better understanding of the underlying concepts of k-modulation for β^* measurements.

6.4 Beam Based Alignment

Apart from changing the tune of the machine, modulating the strength of a quadrupole can also change the closed orbit of the beam if the quadrupole or beam are misaligned. The change in orbit then alters the position of the beam as it passes through the sex-

tupoles which results in the beam experiencing a quadrupole like field inducing a parasitic tune change. This parasitic tune change can have an impact on the measured β functions and the resulting β^* measurement. It is therefore helpful to be able to predict this parasitic tune change to increase the accuracy of the measurements.

Measuring the orbit throughout the machine can allow one to reconstruct the initial offset causing this effect. This section will outline a method that exploits the orthonormality of the singular-vectors produced using SVD to compute this offset and remove noise. Such a method can help align the quadrupoles and measure the crossing angles in the LHC and future machines and hence reduce errors and luminosity loss. The method can also be used to help reconstruct the orbit in the sextupoles and estimate the parasitic tune change in order to improve k-modulation β measurements.

6.4.1 Data Set

A good data set on which this method can be tested is fill 5380, taken on 07.10.2016. During this fill both the β^* in IP1 and IP8 were measured twice using k-modulation. The benefit of this fill is that the first k-modulation measurement in IR8 was done with a crossing angle of 230 µrad switched on in the horizontal plane and the crossing angle was switched off for the second measurement. The measurement with crossing angle should give a clear signal that can be compared against the measurement with the crossing angle turned off. For both measurements a separation bump in the vertical plane was turned on so there should also be a signal in the vertical plane that remains unchanged.

Figure 6.8 shows an example of some data taken during the k-modulation process.

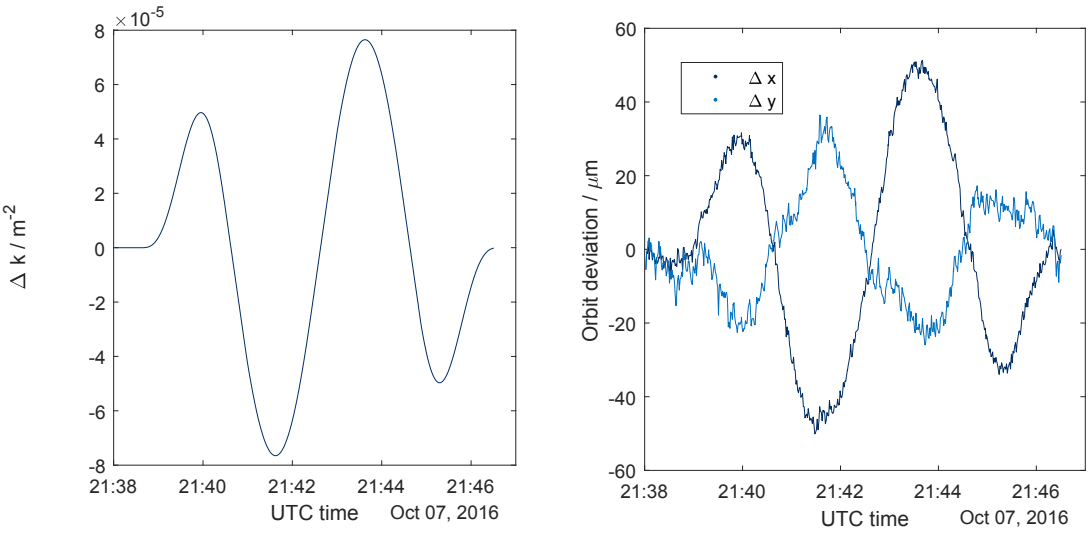

(a) Change in k-value

(b) Change in Orbit

Figure 6.8: Example of measured k-value and corresponding orbit change during k-modulation.

Figure 6.8a shows the change in k value in the left Q1 magnet during modulation without a crossing angle whilst Figure 6.8b shows the resulting change in orbit in beam 1 measured in BPM.31L1.B1, which is located in the arc between IP8 and IP1. As expected, there is a clear orbit response in both planes.

On top of the data from the measurement, it is useful to apply the method on model data so that the results can be compared and the method can be validated. The model data used is generated using a MADX script that loads the optics used during the measurement and turns on the 230 µrad crossing angle as required. It then varies the k-value of the inner quadrupoles and writes the resulting orbit in the BPMs in an output file. The script outputs the k-value and orbit data in the same format as the real data with artificial time stamps so that it can be read in the same algorithm.

6.4.2 Straightforward Method

The closed orbit response, Δz_{co}, to a change in k is given by Equation 1.32 in Section 1.2.4 as

$$\Delta z_{co} = \mp z_q \frac{\beta_z \cot(\pi Q_z) \Delta kl}{2 + \beta_z \cot(\pi Q_z) \Delta kl},$$
$$\Delta z'_{co} = \mp z_q \frac{\left[1 - \alpha_z \cot(\pi Q_z)\right] \Delta kl}{2 + \beta_z \cot(\pi Q_z) \Delta kl},$$

which is directly proportional to the offset between the beam and the centre of the modulated quadrupole, z_q. The resulting change in closed orbit in downstream BPMs can be determined using the transfer matrix between the modulated quadrupole and the BPM, $\mathbf{M}_{Q \to BPM}$ so that

$$\Delta z_{BPM} = M_{Q \to BPM,11} \Delta z_{co} + M_{Q \to BPM,12} \Delta z'_{co}, \tag{6.5}$$

which also varies linearly with z_q. The Twiss parameters in the quadrupole, tune and the transfer matrix can be determined from the MADX model and the Δkl value is given by the measurement. This implies that the orbit change in the BPM can be rewritten as

$$\Delta z_{BPM}(t, s) = f(\Delta k(t), BPM(s)) z_q, \tag{6.6}$$

where $f(\Delta k(t), BPM(s))$ is a function of the machine properties of the longitudinal position of the BPM, s, and the value of Δk at the time of the measurement, t. The offset of the modulated quadrupole can then be estimated from the measured orbit in a BPM as

$$z_q = \Delta z_{BPM}(t, s)/f(\Delta k(t), BPM(s)). \tag{6.7}$$

The most straight forward way of exploiting this could be done by computing this offset from every BPM at every time step during the modulation and calculating the average.

Before calculating this, it is helpful to get a qualitative understanding of the data. This can be done by averaging the measured z_q from each BPM over the entire time and plotting a histogram showing the results. Figure 6.9 shows four histograms with the measured z_q from beam 1 for the first quadrupole left of IP8 in the horizontal and vertical planes with and without activating the crossing angle.

The first observation that can be made is that, as expected, most BPMs measure a large offset of several millimetres in the horizontal plane when the crossing angle is on. Once the crossing angle is turned off, most BPMs measure a small offset below one millimetre but the results are less coherent. In the vertical plane, the histograms indicate an offset of about a millimetre for both measurements. The location of the peak is consistent between the two measurement which is expected since the vertical separation remained turned on.

Another observation seen in Figure 6.9 is the fact that there is a large spread in estimated offset and a large number of outliers. This makes it hard to justify the results since a single outlier can greatly skew the results and the standard deviation is of the same order of magnitude as the measurement. This means the method has to be optimised to reduce this error, either by applying statistical methods to filter

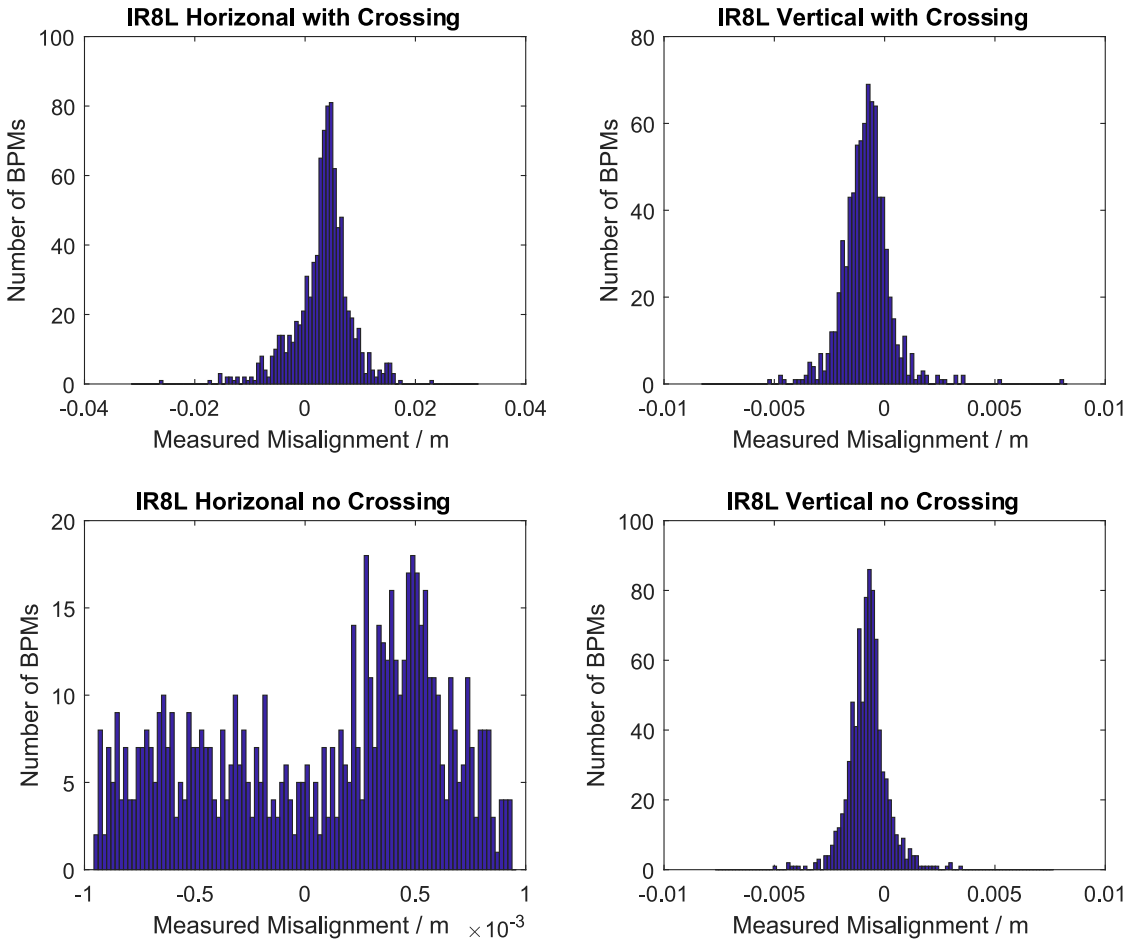

Figure 6.9: Histograms showing offset measurements calculated using different BPMs whilst modulating the first quadrupole left of IP8.

the data or by improving the analysis method.

6.4.3 Ratio Method

One source for errors and outliers in the measured offset could be inaccuracies in the optics model used and effects not taken into account when deriving Equation 6.5. A simple way of checking this conjecture is by comparing the actual maximum amplitude of oscillations measured by the BPMs against the amplitude predicted using the optics model and Equation 6.5. This is done in the horizontal plane with data obtained

whilst modulating the left quadrupole in IR8 whilst the crossing angle is on and is shown in Figure 6.10a.

Figure 6.10 also provides a zoomed in sample of the plot in Figure 6.10b, from which one can see that whilst there is a good agreement overall, there are some severe disagreements, for example in BPM number 719. One solution might be to identify BPMs that have a large disagreement and excluding their results in the measurement. However, one would have to be careful not to lose information when selecting these BPMs.

Another approach, could exploit the fact that there are measurements with and without crossing angle orbit bumps turned on. For the case with the crossing angle turned on, the offset can be expressed as the sum of the offset due to the misalignment, $z_{q,mis}$, and the offset due to the crossing angle, $z_{q,cross}$ so that the orbit change in the BPM when the crossing angle is turned on is

$$\Delta z_{BPM,on}(t,s) = f(\Delta k(t), BPM(s))(z_{q,mis} + z_{q,cross}). \tag{6.8}$$

Similarly, when the crossing angle is turned off the change in orbit will be

$$\Delta z_{BPM,off}(t,s) = f(\Delta k(t), BPM(s))(z_{q,mis}). \tag{6.9}$$

Dividing the orbit changes for measurements with equal Δk with and without crossing angles therefore yields

$$\frac{\Delta z_{BPM,on}}{\Delta z_{BPM,off}} = \frac{z_{q,mis} + z_{q,cross}}{z_{q,mis}} = 1 + \frac{z_{q,cross}}{z_{q,mis}}. \tag{6.10}$$

This can be used to work out the ratio between the misalignment and the controlled orbit bump and is independent of the model. This method was applied to

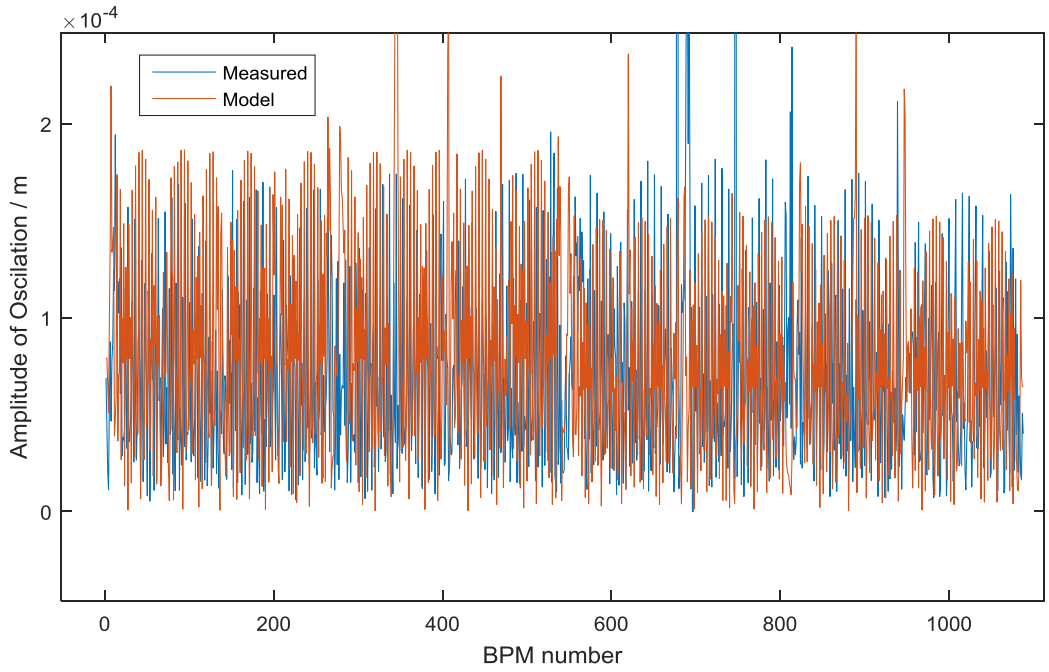

(a) Overview

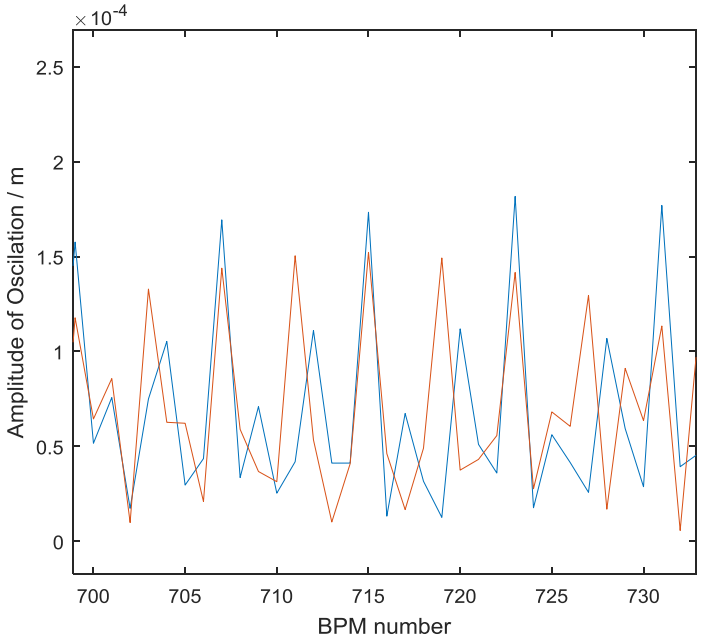

(b) Zoomed in Sample

Figure 6.10: Measured and predicted amplitudes of oscillations in BPMs due to k-modulation.

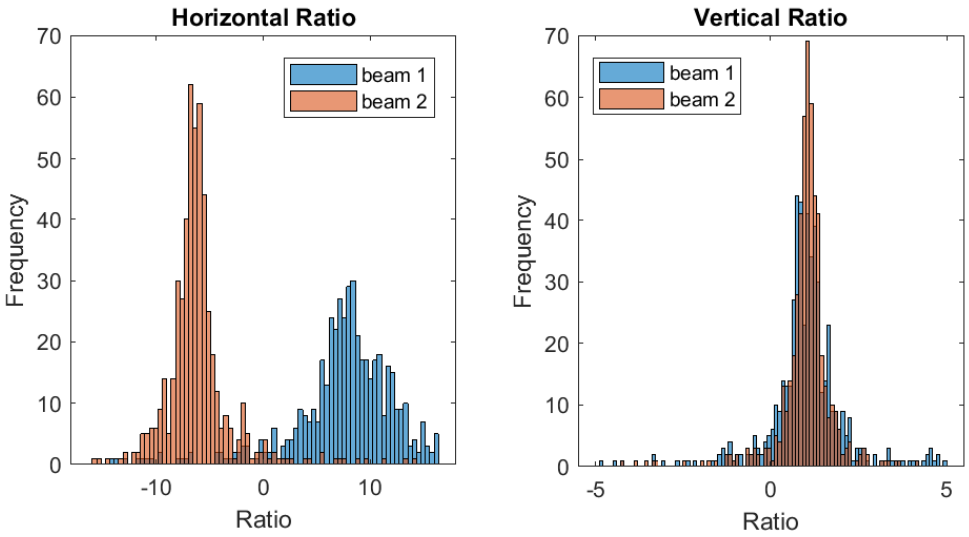

Figure 6.11: Ratio of orbit deviation with and without crossing angle during k-modulation of the left quadrupole around IP8.

the data from modulating the left quadrupole in IR8 and the results obtained using different BPMs for both beam 1 and beam 2 are shown in Figure 6.11.

The results for beam 1 and beam 2 in the horizontal plane agree with each other since the ratios observed by the BPMs are almost opposite and equal. This is because whilst $z_{q,cross}$ is in opposite directions for the two beams, $z_{q,mis}$ is the same for both beams. However, again there is still a lot of noise and outliers making it hard to justify the results. Similarly, in the vertical plane both beams produce seem to produce a ratio of around one, which is what one would predict given that the vertical separation bump stayed unchanged. The level of noise and outliers is also very high in the vertical plane, making it hard to justify the results.

The accuracy of the measurements does not seem to have increased significantly by using this model independent approach. Moreover, in order to measure the actual misalignment, one needs to precisely know or measure the offset due to the crossing,

which is complicated in the first place. Finally, two sets of measurements are not always available and it would take at least twice as long to record the data needed. These reasons suggest that the model independent ratio approach does not provide a satisfactory solution and it would be preferable to use statistical methods to systematically reduce the noise in the measurements.

6.4.4 Singular Value Decomposition Method

Singular value decomposition (SVD) is a method widely used in accelerator physics to identify and eliminate noise in a large data set [132]. SVD factorises a matrix $\mathbf{M}$ so that

$$\mathbf{M} = \mathbf{U}\mathbf{\Sigma}\mathbf{V}^T, \tag{6.11}$$

where $\mathbf{U}$ and $\mathbf{V}$ are unitary matrices and $\mathbf{\Sigma}$ has diagonal entries known as singular values, σ_i. Because $\mathbf{U}$ and $\mathbf{V}$ are unitary, their columns form a set of orthonormal vectors known as the left- and right-singular vectors, $\mathbf{u_i}$ and $\mathbf{v_i}$ respectively.

For accelerators, it is common to store the orbit data from all BPMs during a measurement in a matrix $\mathbf{B}$ such that $B_{ij} = x_j(t_i)$. It can then be decomposed, leading to left-singular vectors containing spatial information and the right-singular vectors representing temporal information. Large singular values indicate that the corresponding mode is due to a signal, whilst small singular values are attributed to noise. Data is often cleaned by deleting σ_i smaller than a certain threshold from $\mathbf{\Sigma}$ and then multiplying out the matrices to recover a cleaned $\mathbf{B}$.

The method developed in the scope of this thesis does not clean the data directly but rather exploits the orthonormality of the singular vectors and the properties of

Equation 6.6. Equation 6.6 can be used to compute the orbit response measured in the BPMs during k-modulation for a situation where $z_q = 1$ m and store this model data in a matrix $\mathbf{B_m}$. The decomposition of this matrix only yields one non-zero singular value, σ_m, so that

$$\mathbf{B}_m = \mathbf{u}_m \sigma_m \mathbf{v}_m^T, \tag{6.12}$$

where $\mathbf{u}_m$ and $\mathbf{v}_m$ are unit vectors representing the machine properties and the temporal change in k.

Since the orbit response varies linearly with z_q, the matrix containing the measured orbits, $\mathbf{B}_{data}$, should have a signal proportional to $\mathbf{B}_m$ by a factor z_q as well as some noise $\mathbf{N}$ so that

$$\mathbf{B}_{data} = \mathbf{B}_m z_q + \mathbf{N} = \mathbf{u}_m \sigma_m \mathbf{v}_m^T z_q + \mathbf{N}. \tag{6.13}$$

Therefore the offset can be measured from the data as

$$z_{meas} = \frac{\mathbf{u}_m^T \mathbf{B}_{data} \mathbf{v}_m}{\sigma_m} = \frac{\mathbf{u}_m^T \mathbf{u}_m \sigma_m \mathbf{v}_m^T z_q \mathbf{v}_m}{\sigma_m} + \frac{\mathbf{u}_m^T \mathbf{N} \mathbf{v}_m}{\sigma_m} = z_q + \frac{\mathbf{u}_m^T \mathbf{N} \mathbf{v}_m}{\sigma_m} = z_q + \epsilon, \tag{6.14}$$

where $\epsilon \equiv \frac{\mathbf{u}_m^T \mathbf{N} \mathbf{v}_m}{\sigma_m}$ is the error in the measurement and should decrease as the size of the data set increases. Once z_{meas} has been found, the error can be estimated as

$$\epsilon = \frac{\mathbf{u}_m^T (\mathbf{B}_{data} - \mathbf{B}_m z_{meas}) \mathbf{v}_m}{\sigma_m}. \tag{6.15}$$

The SVD code can be applied to the IP8 measurements with and without crossing angles as well as the simulated data with the crossing angle. The results for the left and right quadrupole k-modulation are shown in Tables 6.4 and 6.5 respectively.

From Tables 6.4 and 6.5 one can see that there is a good agreement in the measured offset in the vertical plane for both measurements, this shows that the method gives

consistent results when the conditions are unchanged. In the horizontal plane there is a clear change in the measured offset when the crossing angle is turned on. The offset due to the crossing angle is consistent between the two beams and similar in the left and right quadrupoles. Moreover, the measured offsets in both planes are in excellent agreement with the results from the model and the actual results are within the error margins for all measurements. This is an indication that the error margins are perhaps too pessimistic.

The error margin for the crossing angle offset measurements is about 20 %, making it comparable to similar methods [133]. The misalignment of the quadrupoles can be estimated from the measurement in the horizontal plane with the crossing angle turned off. Here the errors are of the same order of magnitude as the measurements, however, the results from beams 1 and beam 2 are consistent in both the right and left quadrupoles which makes sense since they travel through the same aperture. The error in misalignment can potentially be reduced by combining the information of both beams. For both the crossing angle and misalignment measurements the errors might reduce in the future once good agreement between different measurements and model can be replicated.

Plane	**Beam**	$\mathbf{z_{meas}}$ **/ mm**		
		No Crossing	Crossing	Model
Horizontal	1	0.5 ± 0.3	4.6 ± 0.6	4.3
	2	0.8 ± 0.4	-5.2 ± 1.1	-4.6
Vertical	1	-0.7 ± 0.4	-0.7 ± 0.4	-1.0
	2	1.2 ± 0.6	1.3 ± 0.7	1.0

Table 6.4: Results from SVD k-modulation code on measurements in left IR8 quadrupole with and without crossing angles turned on and for simulated data.

Plane	Beam	$\mathbf{z_{meas}}$ / mm		
		No Crossing	Crossing	Model
Horizontal	1	-0.2 ± 0.1	-4.6 ± 0.6	-4.6
	2	-0.07 ± 0.07	4.4 ± 1.1	4.3
Vertical	1	-1.4 ± 0.4	-1.4 ± 0.5	-1.0
	2	0.9 ± 0.5	0.9 ± 0.4	1.0

Table 6.5: Results from SVD k-modulation code on measurements in right IR8 quadrupole with and without crossing angles turned on and for simulated data.

Another way the method can be verified is by comparing the results to those obtained using similar methods. The crossing angle measurement described in [133] is chosen for this. This is done for LHC fill 5422 where the half crossing angle was set to 140 µrad in IP1 and IP5. The crossing angle can be obtained by measuring the separation of the beams in the quadrupoles using the results from the modulation and dividing this by the distance to the IP. The difference in the measured crossing angle obtained from doing this using the left and right quadrupoles can be used as an estimate of the error.

The offsets measured using the method described in [133] yield a half crossing angle of 155 ± 10 µrad in IP1 and 153 ± 12 µrad in IP5. Whilst the results using the SVD method give a half crossing angle of 149 ± 18 µrad in IP1 and 141 ± 18 µrad in IP5. The results of both methods are in good agreement with each other and the model value. The crossing angle computed using the SVD method results in a slightly larger error, however, the estimates in crossing angle are closer to the model value than the results obtained using the other method.

6.4.5 Parasitic Tune Change

Apart from measuring the misalignment of the quadrupole and the magnitude of the crossing angle, the offset measurement can also be used to predict the new closed orbit through the sextupoles caused by the modulation and hence estimate the parasitic tune change. This could greatly improve the accuracy of the β measurements and the subsequent β^* reconstruction.

Once the offset is measured, the new closed orbit in the quadrupole can be calculated for every Δk using Equation 1.32. The orbit in the sextupoles can then be calculated using the transfer matrix between the quadrupole and the sextupoles. In a given sextupole, a horizontal offset, x_s, results in a quadrupole like field of magnitude $k_{2,S}x_S$. The tune change due to this sextupole is therefore equal to [134]

$$\Delta Q_z = \pm\frac{\beta_{Sz}k_2L_Sx_S}{4\pi}, \tag{6.16}$$

where β_S is the average β function in the sextupole and L_S is the length of the sextupole. The tune change has a plus sign in the horizontal and a minus sign in the vertical plane. The contributions from all sextupoles can be summed up to work out the overall parasitic tune change.

The best way of testing this method is with k-modulation data from simulations as the tune change can be recorded under identical conditions with and without offsets. The actual parasitic tune change can be calculated as the difference in tune change for both simulations and can be compared to the parasitic tune change estimate worked out using the method above.

The simulated data used is the same as the data described in Section 6.4.1 with

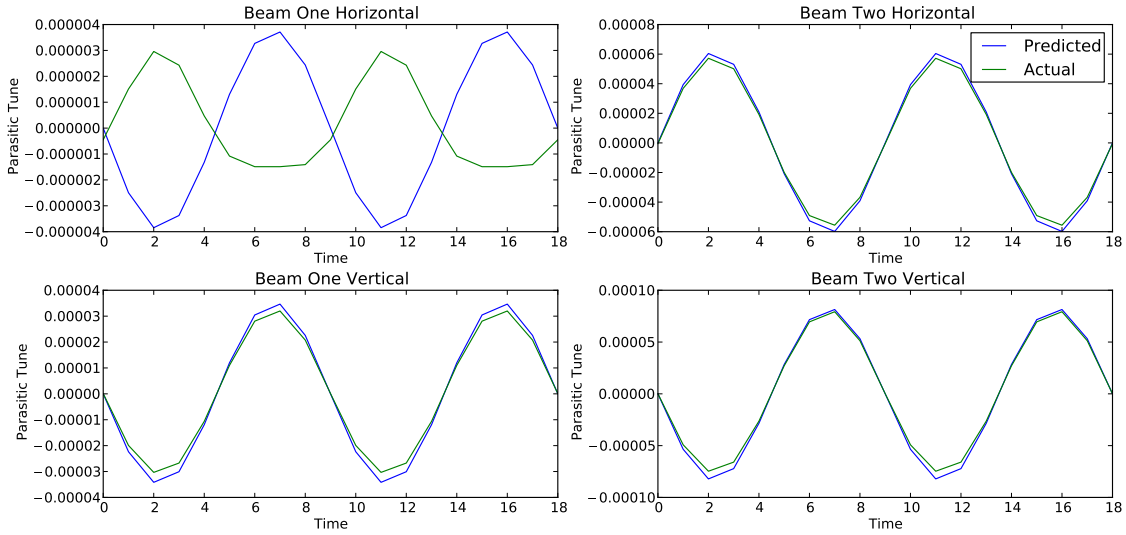

Figure 6.12: Parasitic tune change predicted using offset measurement compared to actual value obtained from simulations.

an additional simulation with no crossing angle. The results of predicted tune change compared to the actual tune change obtained when modulating the quadrupole left of IP8 is shown in Figure 6.12.

The prediction is in good agreement to the actual parasitic tune change for the vertical tune of beam 1 and both tunes of beam 2. However, it seems that it is out of phase for the horizontal tune of beam 1. A big difference between the horizontal tune of beam 1 and the other tunes is that the parasitic tune change in this situation is an order of magnitude smaller than the other parasitic tune changes. When plotting the error in the predicted tune change instead of the actual parasitic tune change, as done in Figure 6.13, it can be seen that the error in the prediction is very similar for all situations. It can also be seen from Figure 6.13 that this is also the case for data obtained when modulating the quadrupole to the right of IP8.

Since the simulations are done for optics with an equal β^* in both planes, the

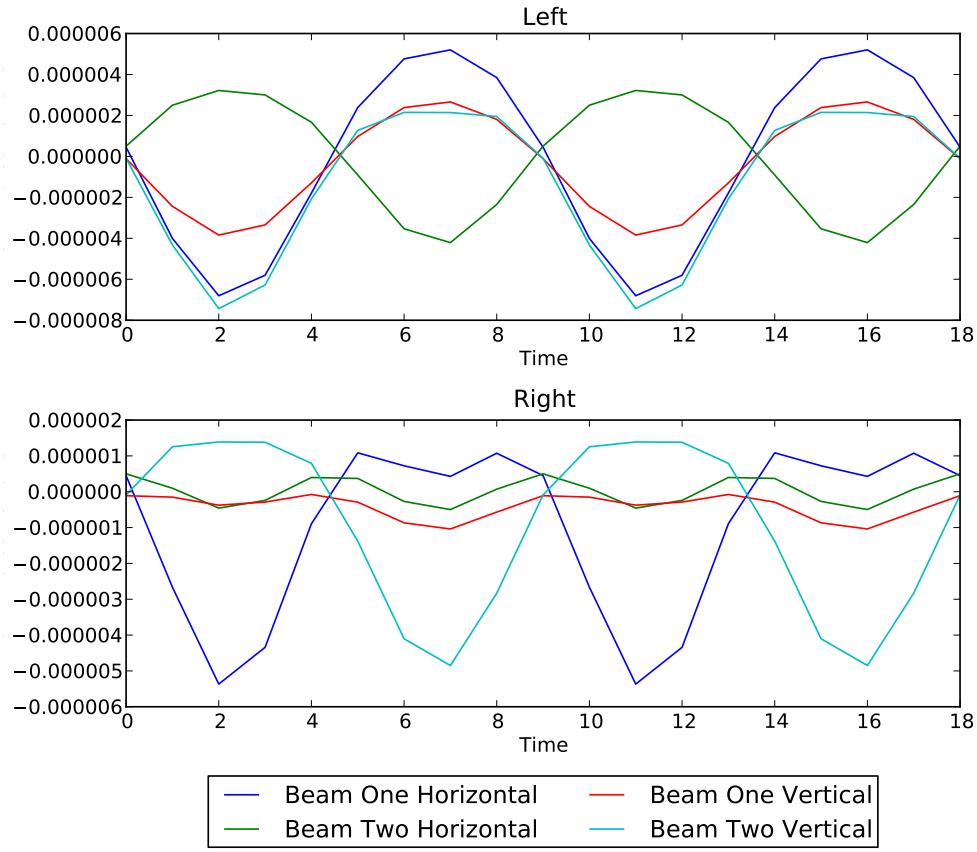

Figure 6.13: Error in parasitic tune change predicted using offset measurement obtained from simulations.

β functions in both planes and beams should be roughly equal in the quadrupoles. Hence, the nominal tune change due to the k-modulation should be similar in all situations meaning that the error in the prediction affects all planes and beams equally. The fact that the error is large compared to the actual parasitic change in the horizontal plane of beam 1 is therefore not a significant problem since the parasitic tune change is very small in the first place. Therefore, this method can be used to improve the β measurements by correcting the measured tune change using the prediction.

For completeness it should also be stated that several attempts were made to further decrease this error in parasitic tune change. The first correction is to include

the contributions due to skew quadrupole fields that arise from vertical offsets in the sextupoles. This correction assumes the initial machine coupling is zero when computing the contribution to the vertical and horizontal tunes. The second improvement explored is to add a β beating induced by the modulation of the quadrupole when working out the change in tune using Equation 6.16. Both these methods increased the errors in the predicted parasitic tune changes when applied individually and together and were dropped as they only made the prediction more complicated and dependant on the model.

6.5 Conclusions and Outlook

The design and elaborate testing of the ballistic optics has provided a means to measure the ideal path and calibrate the BPMs. When put in context with the EIR designs presented in Chapter 4 and Chapter 5, it shows the importance of having an EIR that is flexible enough to achieve special optics when needed whilst not violating any hardware constraints. One unforeseen advantage of this optics is the large horizontal dispersion that can be used for calibrating the BPMs. An interesting extension to this study might be to devise a method that can induce vertical dispersion in the machine to further improve the calibration. Another extension could be to design alignment optics for the proposed EIR of the HE-LHC and FCC-hh colliders. If these optics cannot be achieved this might have an impact on the alignment tolerances and BSC and DA studies would have to be repeated.

The insights into the limitations of β^* measurements from k-modulation have resulted in a better understanding of the process and possible improvements. This

could have an impact on the accuracy of β^* measurements in the LHC and future machines and provide a means to improve the luminosity of colliders. The same is true for the beam based alignment using SVD analysis. This novel method provides measurements that are in agreement with models and allows one to compute the offsets of quadrupoles during k-modulation without requiring further measurements. This can save time during optics commissioning and reduce the idle time of accelerators. Moreover, it may also provide a means to improve the β^* measurements by correcting for the parasitic tune shifts, which was also demonstrated in this chapter.

Chapter 7

Summary and Outlook

This thesis presents various optics solutions designed to overcome a spectrum of challenges, with the main focus lying on collision optics. In the case of the FCC-hh, the triplet was optimised in order to be able to deal with the unprecedented high energies. A flat optics solution is matched to demonstrate a mitigation strategy in case crab cavities are not feasible. The high energies are also a driving factor in the HE-LHC triplet design, however, the overall EIR layout presented in this thesis also takes into account the strict spatial constraints that a novel collider in the LHC tunnel would face. As well as the classical matching of finite elements using MADX, an exact solution found using the thin lens approximation is used to come up with these triplets.

The thin lens formalism also helped to gain insights into the nature of fringe field effects in the EIR of the NICA collider and come up with an alternative design to improve the DA. Unlike the HE-LHC and FCC-hh the NICA collider is already under construction, leaving less opportunity to change other sections of the machine. The restrictions for the LHC alignment optics are even more stringent as the hardware is already in place — the optics are designed and matched using finite element matching

and symmetry considerations and the feasibility of the optics was also checked during a dry run.

In the scope of the HE-LHC design, optics solutions for two sections outside of the EIR are presented. Firstly, a spurious dispersion correction scheme in the arcs is demonstrated, which is based on the HL-LHC scheme with a small modification due to the non-ideal phase advances to the arc sextupoles. The second optics presented is for IR4, it increases the space available for RF-cavities and is adapted to the HE-LHC beam but also demonstrates how the IR can be used for the double tuning scheme which has helped increase the DA of the HE-LHC and FCC-hh. Both these optics are directly linked to issues arising from the EIR.

Throughout this thesis two of the main motivations are fulfilling physical and dynamic aperture requirements. For the HE-LHC and FCC-hh the aperture bottleneck was primarily in the triplet and separation dipoles as the large beam sizes and shielding thicknesses require big coil radii for the triplet magnets. At the same time the small β^* values demand very strong focusing from the triplet. Balancing this in a cost and space efficient way has led to an optimised FCC-hh triplet produced using a dedicated optimisation code. This triplet is comparable to the baseline option but was designed without prior information and can be constructed of identical sub-magnets. The same method applied to the HE-LHC results in a triplet that is almost 30 % shorter than one would expect from simple scaling.

For the injection optics of these future machines and for the alignment optics of the LHC, the aperture bottleneck shifts back to the matching section. This is especially problematic in the case of the LHC alignment optics due to the large field free region

and the symmetry causing high β functions in the matching section. Nevertheless, this thesis presents the first matched LHC optics with Q4 switched off that is both stable at injection and can also operate at top energy. The symmetry of the optics also provides a novel aspect compared to previous versions, including the fact that the large dispersion that arises from this optics is helpful for the calibration of the BPMs.

Using various optimisation methods, the DA of the HE-LHC with the EIR presented in this thesis and triplet errors is demonstrated to be 24.0 σ, which is above the minimum requirement of about 12 σ. By systematically exploring the nature of fringe fields and replacing the triplet installed in the NICA lattice with a doublet of the same length, the DA was increased by 22 % in the horizontal and over 50 % in the vertical plane.

The insights gained from these optimisations can help increase the stability and acceptance of other future accelerators. These features can also be improved with better measurement methods, which are also provided in this thesis. The alignment of the triplet quadrupoles and the crossing angle can be precisely measured using orbit data from k-modulation and the SVD method. This can also be used to improve the tune change measurement used for β^* reconstruction, the importance of this, especially for vdM optics, is also shown. The findings on the limitations of k-modulation in the special case of the vdM optics is especially important as it can drive the design of future high β^* optics in the LHC after its second long shut down.

Overall this thesis provides a range of tools that can be used for various aspects of EIR design and implementations. Several of these methods have been demonstrated

to be versatile and adaptable for a broad range of problems and machines. Therefore, on top of just benefiting the collaborations included in this thesis, these methods can potentially be used for many other accelerator applications.

Bibliography

[1] J. Jackson. *Classical Electrodynamics*. Wiley, New York, USA, 1999.

[2] J.L.R. Hayden. The dielectric strength of the vacuum: Electrostatic ionization gradient of metal electrodes. *Journal of the American Institute of Electrical Engineers*, 41(11):852–853, Nov 1922.

[3] K. Wille. *The Physics of Particle Accelerators : an Introduction*. Oxford University Press, Oxford, UK, 2000.

[4] E. Wilson. *An Introduction to Particle Accelerators*. Oxford University Press, Oxford, UK, 2001.

[5] E.D. Courant and H.S. Snyder. Theory of the Alternating-Gradient Synchrotron. *Annals of Physics*, 281(1):360 – 408, 2000.

[6] A. Seryi. *Unifying Physics of Accelerators, Lasers and Plasma*. CRC Press, Taylor & Francis Group, Boca Raton, USA, 2016.

[7] A. Langner and R. Tomás. Optics Measurement Algorithms and Error Analysis for the Proton Energy Frontier. *Phys. Rev. ST Accel. Beams*, 18:031002, Mar 2015.

[8] L. Deniau, H. Grote, G. Roy, and F. Schmidt. *The MAD-X Program (Methodical Accelerator Design) User's Reference Manual*. CERN, Geneva, Switzerland, Oct 2018.

[9] F. Zimmermann. Measurement and Correction of Accelerator Optics. Technical Report SLAC-PUB-7844, Stanford Linear Accelerator Center, Stanford, USA, Jun 1998.

[10] R.J. Steinhagen. Tune and Chromaticity Diagnostics. In *CAS - CERN Accelerator School: Course on Beam Diagnostics*, CERN Accelerator School, pages 317–361, Geneva, Switzerland, Jun 2009. CERN.

[11] A. Wolski and F. Zimmermann. Closed Orbit Response to Quadrupole Strength Variation. Technical Report LBNL Report-54360, ATF-03-08, Ernest Orlando Lawrence Berkley National Laboratory, Berkley, USA, Jan 2004.

[12] B.W. Montague. Chromatic Effects and Their First-Order Correction. Technical Report CERN-1987-003-V-1, Geneva, Switzerland, Sep 1985.

[13] O.S. Brüning, S.D. Fartoukh, M. Giovannozzi, and T. Risselada. Dynamic Aperture Studies for the LHC Separation Dipoles. Technical Report LHC-Project-Note-349. CERN-LHC-Project-Note-349, CERN, Geneva, Switzerland, Jun 2004.

[14] E. Keil. Lattices for Collider Storage Rings. In A. W. Chao and M. Tigner, editors, *Handbook of Accelerator Physics and Engineering*, chapter 2.2.3, pages 76–78. World Scientific, Singapore, 1999.

[15] D.A. Edwards and Sypher M. Linear Betatron Motion. In A. W. Chao and M. Tigner, editors, *Handbook of Accelerator Physics and Engineering*, chapter 2.1.1, pages 65–66. World Scientific, Singapore, 1999.

[16] K.T. McDonald and D.P. Russell. Methods of Emittance Measurement. In M. Month and S. Turner, editors, *Frontiers of Particle Beams; Observation, Diagnosis and Correction*, Berlin, Germany, 1989. Springer Berlin Heidelberg.

[17] J.B. Jeanneret and T. Risselada. Geometrical Aperture in LHC at Injection. Technical Report LHC-Project-Note-66, CERN, Geneva, Switzerland, Sep 1996.

[18] J. Irwin and Y.T. Yan. Dynamic Aperture. In A. W. Chao and M. Tigner, editors, *Handbook of Accelerator Physics and Engineering*, chapter 2.3.9, pages 104–107. World Scientific, Singapore, 1999.

[19] R. de Maria, M. Fitterer, M. Fjellstrom, and A. Patapenka. *Sixtrack Physics Manual (Draft)*. CERN, Geneva, Switzerland, Aug 2018. `http://sixtrack.web.cern.ch/`.

[20] F. Schmidt. *Sixtrack User's Reference Manual*. CERN, Geneva, Switzerland, Mar 2018. `http://sixtrack.web.cern.ch/`.

[21] F. Schmidt. *Untersuchungen zur dynamischen Akzeptanz von Protonenbeschleunigern und ihre Begrenzung durch chaotische Bewegung*. PhD thesis, Institut für Experimentalphysik Universität Hamburg, Hamburg, Germany, 1987.

[22] M. Böge and F. Schmidt. Estimates for Long-term stability for the LHC. Technical Report CERN-LHC-Project-Report-114, Geneva, Switzerland, May 1997.

[23] E. McIntosh and R. De Maria. The SixDesk Run Environment for SixTrack. Technical Report CERN-ATS-Note-2012-089, Geneva, Switzerland, Nov 2012.

[24] B.R. Martin. *Nuclear and Particle Physics*. John Wiley & Sons, Chichester, UK, 2006.

[25] M.A. Furman and M.S. Zisman. Luminosity. In A. W. Chao and M. Tigner, editors, *Handbook of Accelerator Physics and Engineering*, chapter 4.1, pages 277–281. World Scientific, Singapore, 1999.

[26] R. Calaga. Crab Cavities for the LHC Upgrade. In *Proceedings - Chamonix 2012 Workshop on LHC Performance*, Chamonix Workshop on LHC Performance, pages 363–372, Geneva, Switzerland, Jan 2012. CERN.

[27] R. de Maria. General method for final focus system design for circular colliders. *Phys. Rev. ST Accel. Beams*, 11:031001, Mar 2008.

[28] M. Bassetti and P. A. Biscari. Lattices for Collider Storage Rings. In A. W. Chao and M. Tigner, editors, *Handbook of Accelerator Physics and Engineering*, chapter 2.2.3, pages 62–64. World Scientific, Singapore, 1999.

[29] B.J. Holzer. Beam Optics and Lattice Design for Particle Accelerators. CERN Accelerator School, Barcelona, Spain, 2011. arXiv:1303.6514.

[30] O.S. Brüning et al. *LHC Design Report*. CERN Yellow Reports: Monographs. CERN, Geneva, Switzerland, 2004.

[31] G. Apollinari and others. *High-Luminosity Large Hadron Collider (HL-LHC): Technical Design Report V. 0.1*. CERN Yellow Reports: Monographs. CERN, Geneva, Switzerland, 2017.

[32] M. Benedikt and F. Zimmermann. FCC: Colliders at the Energy Frontier. In *Proc. 9th International Particle Accelerator Conference (IPAC'18), Vancouver, BC, Canada, April 29-May 4, 2018*, pages 2908–2913, Geneva, Switzerland, Jun 2018. JACoW Publishing.

[33] G.V. Trubnikov et al. The NICA Project at JINR. In *Proc. of International Particle Accelerator Conference (IPAC'16), Busan, Korea, May 8-13, 2016*, pages 2061–2065, Geneva, Switzerland, Jun 2016. JACoW.

[34] E. Keil. The CERN Large Hadron Collider LHC. Technical Report CERN-LHC-Project-Report-83, CERN, Geneva, Switzerland, Dec 1996.

[35] A. de Roeck, J.R. Ellis, and F. Gianotti. Physics Motivations for Future CERN Accelerators. Technical Report CERN-TH-2001-023, Geneva, Switzerland, 2001.

[36] G. Aad et al. Observation of a new particle in the search for the Standard Model Higgs boson with the ATLAS detector at the LHC. *Physics Letters B*, 716(1):1 – 29, 2012.

[37] S. Chatrchyan et al. Observation of a new boson at a mass of 125 gev with the cms experiment at the lhc. *Physics Letters B*, 716(1):30 – 61, 2012.

[38] T. Carli. ATLAS + ALICE highlights. Seoul, Korea, 2018. ICHEP 2018.

[39] R. Aaij et al. LHCb Detector Performance. *Int. J. Mod. Phys.*, A30(07):1530022, 2015.

[40] B.B. Abelev et al. Performance of the ALICE Experiment at the CERN LHC. *Int. J. Mod. Phys.*, A29:1430044, 2014.

[41] C. Wyss. LHC Arc Dipole Status Report. Technical Report CERN-LHC-Project-Report-288, CERN, Geneva, Switzerland, 1999.

[42] S. Fartoukh. Achromatic Telescopic Squeezing Scheme and Application to the LHC and its Luminosity Upgrade. *Phys. Rev. ST Accel. Beams*, 16:111002, Nov 2013.

[43] K. Schindl. The Injector Chain for the LHC; rev. version. Technical Report CERN-PS-99-018-DI, CERN, Geneva, Switzerland, Mar 1999.

[44] A. Verdier. IR4 Tuning for LHC V6.5. Technical Report CERN-LHC-Project-Note-366, CERN, Geneva, Switzerland, Apr 2005.

[45] A. Verdier. The LHC IR6 optics. Technical Report LHC-Project-Note-146, CERN, Geneva, Switzerland, Jun 1998.

[46] N. Aquilina et al. Tune variations in the Large Hadron Collider. *Nuclear Instruments and Methods in Physics Research Section A: Accelerators, Spectrometers, Detectors and Associated Equipment*, 778:6 – 13, 2015.

[47] R. Bruce et al. Reaching record-low β^* at the CERN Large Hadron Collider using a novel scheme of collimator settings and optics. *Nuclear Instruments and Methods in Physics Research Section A: Accelerators, Spectrometers, Detectors and Associated Equipment*, 848:19 – 30, 2017.

[48] J.-P. Koutchouk. The LHC Dynamic Aperture. In *Proceedings of the 1999 Particle Accelerator Conference (Cat. No.99CH36366)*, volume 1, pages 372–376 vol.1, March 1999.

[49] S. Fartoukh et al. The Achromatic Telescopic Squeezing Scheme: Basic Principles and First Demonstration at the LHC. *Conf. Proc.*, C1205201(CERN-ATS-2012-080):TUPPR068. 3 p, May 2012.

[50] R. Ostojic and T.M. Taylor. Proposal for an Improved Optical and Systems Design of the LHC low-β Triplets. Technical Report CERN-LHC-Note-293, CERN, Geneva, Switzerland, Nov 1994.

[51] T.E. D'Amico and G. Guignard. Analysis of Generic Insertions Made of two Symmetric Triplets. Technical Report CERN-SL-98-014-AP, CERN, Geneva, Switzerland, Apr 1998.

[52] N. Siegel. Overview of the LHC Magnets other than the Main Dipoles. In *Particle accelerator. Proceedings, 7th European Conference, EPAC 2000, Vol. 1-3*, pages 23–27, Vienna, Austria, 2000.

[53] F. Bordry and H. Thiesen. LHC Inner Triplet Powering Strategy. In *Particle accelerator. Proceedings, Conference, PAC 2001*, volume C0106181, pages 633–635, Chicago, USA, Jun 2001.

[54] Q. Wu. Crab Cavities: Past, Present, and Future of a Challenging Device. In *Proc. 6th International Particle Accelerator Conference (IPAC'15), Richmond, VA, USA, May 3-8, 2015*, pages 3643–3648, Geneva, Switzerland, Jun 2015. JACoW.

[55] A.A. Garren, X. Luo, F. Méot, and W. Scandale. The LHC Lattice, Version 4. Technical Report CERN-SL-95-06. CERN-LHC-Note-314. CERN-SL-95-06-AP. LHC-NOTE-314, CERN, Geneva, Switzerland, Mar 1995.

[56] H. Damerau et al. LHC Injectors Upgrade, Technical Design Report, Vol. I: Protons. Technical Report CERN-ACC-2014-0337, CERN, Geneva, Switzerland, Dec 2014.

[57] E. Shaposhnikova et al. LHC Injectors Upgrade (LIU) Project at CERN. In *Proc. of International Particle Accelerator Conference (IPAC'16), Busan, Korea, May 8-13, 2016*, pages 992–995, Geneva, Switzerland, Jun 2016. JACoW.

[58] E. Todesco et al. Progress on HL-LHC Nb_3Sn magnets. *IEEE Transactions on Applied Superconductivity*, 28(4):1–9, Jun 2018.

[59] J.L. Abelleira et al. High-Energy LHC design. *Journal of Physics: Conference Series*, 1067(2):022009, 2018.

[60] M. Benedikt, B. Goddard, D. Schulte, F. Zimmermann, and M.J. Syphers. FCC-hh Hadron Collider - Parameter Scenarios and Staging Options. In *Proc. 6th International Particle Accelerator Conference (IPAC'15), Richmond, VA, USA, May 3-8, 2015*, pages 2173–2176, Geneva, Switzerland, Jun 2015. JACoW.

[61] M. Benedikt and F. Zimmermann. Towards future circular colliders. *Journal of the Korean Physical Society*, 69(6):893–902, Sep 2016.

[62] M. Aicheler et al. A Multi-TeV Linear Collider Based on CLIC Technology. Technical report, CERN, Geneva, Switzerland, 2012.

[63] T. Behnke et al. The International Linear Collider Technical Design Report - Volume 1: Executive Summary, 2013. ILC-REPORT-2013-040.

[64] V. Kekelidze et al. Status of the NICA project at JINR. *Nuclear and Particle Physics Proceedings*, 273-275:170 – 174, 2016.

[65] H.H. Gutbrod et al. Fair baseline technical report. Technical report, Gesellschaft fuer Schwerionenforschung mbH, Darmstadt, Germany, 2006.

[66] Y. Zhang, Y.S. Derbenev, F. Lin, V.S. Morozov, and G.H. Wei. JLEIC Ultimate Luminosity With Strong Electron Cooling. presented at IPAC2017 in Copenhagen, Denmark, unpublished, May 2017.

[67] E. C. Aschenauer et al. eRHIC Design Study: An Electron-Ion Collider at BNL. Technical Report arXiv:1409.1633, Brookhaven National Laboratory, Upton, United States, 2014.

[68] J. L. Abelleira Fernandez et al. A Large Hadron Electron Collider at CERN: Report on the Physics and Design Concepts for Machine and Detector. *J. Phys.*, G39:075001, 2012.

[69] E. Adli et al. Acceleration of Electrons in the Plasma Wakefield of a Proton Bunch. *Nature*, 561:363–367, 2018.

[70] M. Hofer et al. Integrated Full HE-LHC Optics and Its Performance. In *Proc. 9th International Particle Accelerator Conference (IPAC'18), Vancouver, BC, Canada, April 29-May 4, 2018*, pages 348–351, Geneva, Switzerland, Jun 2018. JACoW Publishing.

[71] J. Keintzel. Optics Design and Performance Aspects of the HE-LHC. Master's thesis, Technische Universität Wien, Vienna, Austria, 2018.

[72] F. Burkart et al. Conceptual Design Considerations for a 1.3 TeV Superconducting SPS (scSPS). In *Proc. of International Particle Accelerator Conference (IPAC'17), Copenhagen, Denmark, 1419 May, 2017*, pages 3323–3326, Geneva, Switzerland, May 2017. JACoW.

[73] Y.M. Nosochkov et al. Optimized Arc Optics for the HE-LHC. In *Proc. 9th International Particle Accelerator Conference (IPAC'18), Vancouver, BC, Canada, April 29-May 4, 2018*, pages 277–280, Geneva, Switzerland, Jun 2018. JACoW Publishing.

[74] M. Crouch. Collimation. Amsterdam, Netherlands, Apr 2018. FCC Week 2018.

[75] S. Fartoukh. Achromatic Telescopic Squeezing Scheme and Application to the LHC and its Luminosity Upgrade. *Phys. Rev. ST Accel. Beams*, 16:111002, Nov 2013.

[76] A. Chancé et al. Updates on the Optics of the Future Hadron-Hadron Collider FCC-hh. In *Proc. of International Particle Accelerator Conference (IPAC'17), Copenhagen, Denmark, 1419 May, 2017*, pages 2023–2026, Geneva, Switzerland, May 2017. JACoW.

[77] D. Schulte. Parameters and layout. Amsterdam, Netherlands, Apr 2018. FCC Week 2018.

[78] E. Renner et al. Design and Evaluation of FCC-hh Injection Protection Schemes. In *Proc. 9th International Particle Accelerator Conference (IPAC'18), Vancouver, BC, Canada, April 29-May 4, 2018*, pages 854–857, Geneva, Switzerland, Jun 2018. JACoW Publishing.

[79] A. Chancé, D. Boutin, B. Dalena, B.J. Holzer, and D. Schulte. Overview of Arc Optics of FCC-hh. In *Proc. 9th International Particle Accelerator Conference (IPAC'18), Vancouver, BC, Canada, April 29-May 4, 2018*, pages 141–144, Geneva, Switzerland, Jun 2018. JACoW Publishing.

[80] M. Fiascaris, R. Bruce, D. Mirarchi, and S. Redaelli. First Design of a Proton Collimation System for 50 TeV FCC-hh. In *Proc. of International Particle Accelerator Conference (IPAC'16), Busan, Korea, May 8-13, 2016*, pages 2423–2426, Geneva, Switzerland, Jun 2016. JACoW.

[81] M. Mentink et al. Evolution of the Conceptual FCC-hh Baseline Detector Magnet Design. *IEEE Transactions on Applied Superconductivity*, 28(2):1–10, Mar 2018.

[82] R. Martin et al. Interaction Region Design Driven by Energy Deposition. *Phys. Rev. Accel. Beams*, 20:081005, Aug 2017.

[83] M.I. Besana et al. Energy Deposition in the Betatron Collimation Insertion of the 100 TeV Future Circular Collider. In *Proc. of International Particle Accelerator Conference (IPAC'17), Copenhagen, Denmark, 1419 May, 2017*, pages 68–71, Geneva, Switzerland, May 2017. JACoW.

[84] A.V. Butenko et al. Commissioning of the New Heavy Ion Linac at the NICA Project. In *Proc. of International Particle Accelerator Conference (IPAC'17), Copenhagen, Denmark, 1419 May, 2017*, pages 2362–2365, Geneva, Switzerland, May 2017. JACoW.

[85] M.M. Shandov et al. First Serial Magnetic Measurements of the NICA Collider Twin-Aperture Dipoles. In *Proc. 9th International Particle Accelerator Conference (IPAC'18), Vancouver, BC, Canada, April 29-May 4, 2018*, pages 3645–3648, Geneva, Switzerland, Jun 2018. JACoW Publishing.

[86] V.D. Kekelidze. NICA Project at JINR: Status and Prospects. *Journal of Instrumentation*, 12(06):C06012, 2017.

[87] R. Baartman. Intrinsic Third Order Aberrations in Electrostatic and Magnetic Quadrupoles. arXiv:1508.00058, 2015.

[88] O. Napoly, T.M. Taylor, and B.W. Zotter. A final focus design for the cern linear collider clic. In *Proc. 14th International Conference on High-Energy Accelerators*, pages 137–142, August 1989.

[89] Y.-C. Chao and J. Irwin. Solution of a three thin lens system with arbitrary transfer properties. *Submitted to: Part. Accel.*, 1992.

[90] V. Balandin and S. Orlov. Explicit thin-lens solution for an arbitrary four by four uncoupled beam transfer matrix. *Phys. Rev. ST Accel. Beams*, 15:074001, Jul 2012.

[91] Wolfram Research, Inc. Mathematica, Version 11.3. Champaign, USA, 2018.

[92] G. Rossum. Python reference manual. Technical report, CWI (Centre for Mathematics and Computer Science), Amsterdam, Netherlands, 1995.

[93] L. Nevay et al. *pymadx Documentation*. Royal Holloway, University of London, Egham, UK, 2018.

[94] F. Schmidt, E. Forest, and E. McIntosh. Introduction to the Polymorphic Tracking Code: Fibre Bundles, Polymorphic Taylor Types and "Exact tracking". Technical Report CERN-SL-2002-044-AP, CERN, Geneva, Switzerland, Jul 2002.

[95] O.S. Kozlov et al. NICA Collider Lattice Optimization. In *Proc. of Russian Particle Accelerator Conference (RuPAC'16), St. Petersburg, Russia, November 21-25, 2016*, pages 166–168, Geneva, Switzerland, Feb. 2017. JACoW.

[96] M. Patecki and R. Tomás. Effects of quadrupole fringe fields in final focus systems for linear colliders. *Phys. Rev. ST Accel. Beams*, 17:101002, Oct 2014.

[97] A. Ferrari, P.R. Sala, , A. Fasso, and J. Ranft. FLUKA: A multi-particle transport code. Technical Report SLAC-R-773, Stanford Linear Accelerator Center (SLAC), Stanford, USA, Dec 2005.

[98] D. Schoerling. personal communication, 2016.

[99] R. Martin, B. Dalena, and R. Tomás. Interaction Region for a 100 TeV Proton-Proton Collider. In *Proc. 6th International Particle Accelerator Conference (IPAC'15), Richmond, VA, USA, May 3-8, 2015*, pages 1996–1999, Geneva, Switzerland, Jun 2015. JACoW.

[100] J.L. Abelleira, M.I. Besana, E. Cruz Alaniz, A. Seryi, and L. van Riesen-Haupt. FCC-hh Final-Focus for Flat-Beams: Parameters and Energy Deposition Studies. In *Proc. of International Particle Accelerator Conference (IPAC'17), Copenhagen, Denmark, 1419 May, 2017*, pages 2139–2142, Geneva, Switzerland, May 2017. JACoW.

[101] J.L. Abelleira, E. Cruz Alaniz, A. Seryi, and L. van Riesen-Haupt. Energy Deposition Studies and Luminosity Evolution for the Alternative FCC-hh Triplet. In *Proc. 9th International Particle Accelerator Conference (IPAC'18), Vancouver, BC, Canada, April 29-May 4, 2018*, pages 352–355, Geneva, Switzerland, Jun 2018. JACoW Publishing.

[102] S. Roesler, R. Engel, and J. Ranft. The Monte Carlo event generator DPMJET-III. In *Advanced Monte Carlo for radiation physics, particle transport simulation and applications. Proceedings, Conference*, pages 1033–1038, Lisbon, Portugal, Oct 2000.

[103] A. Zaborowska. Fcc-hh and he-lhc experiments detectors overview. Amsterdam, Netherlands, Apr 2018. FCC Week 2018.

[104] R. Calaga. Overview of CC for the HL-LHC project. Geneva, Switzerland, 2017. International review of the Crab Cavity Performance for HiLumi.

[105] T. Pieloni et al. Beam-Beam Effects. Amsterdam, Netherlands, Apr 2018. FCC Week 2018.

[106] R. Martin et al. Experimental Insertions. Amsterdam, Netherlands, Apr 2018. FCC Week 2018.

[107] A. Infantino et al. Energy Deposition from Collision Debris in FCC-hh EIR. Karlsruhe, Germany, Oct 2018. 4th EuroCirCol Meeting.

[108] E. Cruz Alaniz et al. Methods to Increase the Dynamic Aperture of the FCC-hh Lattice. In *Proc. 9th International Particle Accelerator Conference (IPAC'18), Vancouver, BC, Canada, April 29-May 4, 2018*, pages 3593–3596, Geneva, Switzerland, Jun 2018. JACoW Publishing.

[109] E. Cruz-Alaniz. Dynamic Aperture Studies for FCC-hh at Collision. Karlsruhe, Germany, Oct 2018. 4th EuroCirCol Meeting.

[110] R. De Maria, S.D. Fartoukh, and M. Fitterer. HLLHCV1.1 Optics Version for the HL-LHC Upgrade. In *Proc. 6th International Particle Accelerator Conference (IPAC'15), Richmond, VA, USA, May 3-8, 2015*, pages 2090–2093, Geneva, Switzerland, Jun 2015. JACoW.

[111] M. Benedikt et al. Future Circular Collider, Conceptual Design Report, Volume 4: High Energy LHC. Technical Report CERN-ACC-2018-0059, CERN, Geneva, Switzerland, 2019.

[112] L. van Riesen-Haupt and J. Abelleira. HE-LHC Triplet Optimisation. Berlin, Germany, May 2017. FCC Week 2017.

[113] J.L. Abelleira, E. Cruz Alaniz, A. Seryi, and L. van Riesen-Haupt. HE-LHC Final Focus: Flat Beam Parameters and Energy Deposition Studies. In *Proc. 9th International Particle Accelerator Conference (IPAC'18), Vancouver, BC, Canada, April 29-May 4, 2018*, pages 356–359, Geneva, Switzerland, Jun 2018. JACoW Publishing.

[114] T. Pieloni. Beam-beam effects. Amsterdam, Netherlands, Apr 2018. FCC Week 2018.

[115] E.Y. Wildner, J. Beauquis, G. Grubello, M. La China, and W. Scandale. HE-LHC Final Focus: Flat Beam Parameters and Energy Deposition Studies. In *Proc. 9th Eurpean Particle Accelerator Conference (EPAC 2004)*, pages 1648–1650, Geneva, Switzerland, Jun 2004. JACoW Publishing.

[116] T. Nakamoto et al. Model Magnet Development of D1 Beam Separation Dipole for the HL-LHC Upgrade. *IEEE Transactions on Applied Superconductivity*, 25(3), Jun 2015.

[117] S. Farinon, P. Fabbricatore, S. Curreli, and E. Todesco. The design of superconducting separation dipoles d2 for the high luminosity upgrade of lhc. *IEEE Transactions on Applied Superconductivity*, 26(4):1–4, Jun 2016.

[118] J. Abelleira. HE-LHC IR Energy Deposition Simulations. Karlsruhe, Germany, Oct 2018. 4th EuroCirCol Meeting.

[119] L.H.A. Leunissen. Influence of vertical dispersion and crossing angle on the performance of the LHC. Technical Report CERN-LHC-Project-Report-298, CERN, Geneva, Switzerland, Apr 1999.

[120] R. Kersevan. New beamscreen design proposal. Geneva, Switzerland, Mar 2018. FCC General Design Meeting — New Beam Screen.

[121] E. Shaposhnikova. HE-LHC: Longitudinal beam parameters. Geneva, Switzerland, Jul 2018. HE-LHC General Design Meeting.

[122] L. van Riesen-Haupt et al. Optics for RF Acceleration Section for the High Energy Large Hadron Collider. In *Proc. 9th International Particle Accelerator Conference (IPAC'18), Vancouver, BC, Canada, April 29-May 4, 2018*, pages 345–347, Geneva, Switzerland, Jun 2018. JACoW Publishing.

[123] A. Verdier. Alignment optics for LHC. Technical Report CERN-LHC-PROJECT-NOTE-325, CERN, Geneva, Switzerland, Jul 2003.

[124] A. Garcia-Tabares Valdivieso et al. MD Test of a Ballistic Optics. Technical Report CERN-ACC-NOTE-2016-0008, CERN, Geneva, Switzerland, Jan 2016.

[125] R. Tomás et al. Ballistic optics. LMC meeting, Geneva, Switzerland, May 2017.

[126] H.E. Jorgensen, F. Bordry, A. Dupaquier, and G. Fernqvist. High Current, Low Voltage Power Converter [20KA,6V] LHC Converter Prototype. Technical Report CERN-LHC-Project-Report-198, CERN, Geneva, Switzerland, Jul 1998.

[127] R. De Maria, T. Levens, C. Hernalsteens, and Bet M. *PyTimber*. CERN, Geneva, Switzerland, 2018.

[128] T. Persson et al. LHC Optics Commissioning: A Journey Towards 1% Optics Control. *Phys. Rev. Accel. Beams*, 20:061002, Jun 2017.

[129] F. Carlier and R. Tomás. Accuracy and feasibility of the β^* measurement for LHC and High Luminosity LHC using k modulation. *Phys. Rev. Accel. Beams*, 20:011005, Jan 2017.

[130] A. Garcia-Tabares Valdivieso. Optics measurements. Cross-calibration of LHC profile monitors, Geneva, Switzerland, Jan 2017.

[131] R. Alemany-Fernndez et al. Cross-Calibration of the LHC Transverse Beam-Profile Monitors. In *Proc. of International Particle Accelerator Conference (IPAC'17), Copenhagen, Denmark, 1419 May, 2017*, pages 437–440, Geneva, Switzerland, May 2017. JACoW.

[132] R. M. Bodenstein. *A Procedure for Beamline Characterization and Tuning in Open-Ended Beamlines.* PhD thesis, University of Virginia, Charlottesville, USA, 2012.

[133] M. Hostettler et al. Impact of the Crossing Angle on Luminosity Asymmetries at the LHC in 2016 Proton Physics Operation. In *Proc. of International Particle Accelerator Conference (IPAC'17), Copenhagen, Denmark, 1419 May, 2017*, pages 2035–2038, Geneva, Switzerland, May 2017. JACoW.

[134] M. Borland, E. A. Crosbie, and N. S. Sereno. Measurement of Sextupole Orbit Offsets in the APS Storage Ring. In *Proceedings of the 1999 Particle Accelerator Conference*, volume 3, pages 1587–1589, New York, USA, Mar 1999.